

Time-resolved crystallography on the structural dynamics of cryptochromes and photolyases

A dissertation submitted

in fulfillment of the requirements for the degree of

DOCTOR IN NATURAL SCIENCES

(Dr. rer. nat.)

Presented at the

Department of Chemistry

Philipps University Marburg

By

Wang Po Hsun

Kaohsiung, Taiwan

Marburg/Lahn 2023

Accepted as a dissertation by the chemistry department of the Philipps
University of Marburg (university reference number XXXX) on

First reviewer: Prof. Dr. Lars-Oliver Essen (Department of Chemistry, Marburg)

Second reviewer: Prof. Dr. Manuel Maestre-Reyna (Department of Chemistry, Taiwan)

Date of defense: _____

Erklärung

Ich erkläre, dass eine Promotion noch an keiner anderen Hochschule als der Philipps-Universität Marburg, Fachbereich Chemie, versucht wurde.

Hiermit versichere ich, dass ich die vorliegende Dissertation

Time-resolved crystallography on the structural dynamics of cryptochromes and photolyases

selbstständig, ohne unerlaubte Hilfe Dritter angefertigt und andere als die in der Dissertation angegebenen Hilfsmittel nicht benutzt habe. Alle Stellen, die wörtlich oder sinngemäß aus veröffentlichten oder unveröffentlichten Schriften entnommen sind, habe ich als solche kenntlich gemacht. Dritte waren an der inhaltlich-materiellen Erstellung der Dissertation nicht beteiligt; insbesondere habe ich hierfür nicht die Hilfe eines Promotionsberaters in Anspruch genommen. Kein Teil dieser Arbeit ist in einem anderen Promotions- oder Habilitationsverfahren verwendet worden. Mit dem Einsatz von Software zur Erkennung von Plagiaten bin ich einverstanden.

Ort/Datum

Unterschrift (Vor- und Nachname)

“You can overcome anything,
if and only if you love something enough”

— Lionel Messi

List of publications

1. Manuel Maestre-Reyna*, **Po-Hsun Wang**, Eriko Nango, Yuhei Hosokawa, Martin Saft, Antonia Furrer, Cheng-Han Yang, Eka Putra Gusti Ngurah Putu, Wen-Jin Wu1, Hans-Joachim Emmerich, Sophie Franz-Badur, Sylvain Engilberge, Nicolas Caramello, Maximilian Wranik, Hannah Louise Glover, Tobias Weinert, Hsiang-Yi Wu, Cheng-Chung Lee, Wei-Cheng Huang, Kai-Fa Huang, Yao-Kai Chang, Jiahn-Haur Liao, Jui-Hung Weng, Wael Gad, Chiung-Wen Chang, Allan H. Pang, Dardan Gashi, Emma Beale, Dmitry Ozerov, Karol Nass, Gregor Knopp, Philip J. M. Johnson, Claudio Cirelli, Chris Milne, Camila Bacellar, Michihiro Sugahara, Shigeki Owada, Yasumasa Joti, Ayumi Yamashita, Rie Tanaka, Tomoyuki Tanaka, Fangjia Luo, Kensuke Tono, Pavel Müller, Filip Bezold, Valerie Fuchs, Petra Gnau, Stephan Kiontke, Lukas Korf, Viktoria Reithofer, Christian Joshua Rosner, Laura Werel, Roberta Spadaccini, Antoine Royant, Junpei Yamamoto, So Iwata, Joerg Standfuss, Yoshitaka Bessho*, Lars-Oliver Essen*, Ming-Daw Tsai*. Watching the entire DNA repair process by a photolyase at atomic resolution in real time. (Science, 2023, under revision).
2. Maestre-Reyna, M.; Yang, C.-H.; Nango, E.; Huang, W.-C.; Ngurah Putu, E. P. G.; Wu, W.-J.; **Wang, P.-H.**; Franz-Badur, S.; Saft, M.; Emmerich, H.-J.; Wu, H.-Y.; Lee, C.-C.; Huang, K.-F.; Chang, Y.-K.; Liao, J.-H.; Weng, J.-H.; Gad, W.; Chang, C.-W.; Pang, A. H.; Sugahara, M.; Owada, S.; Hosokawa, Y.; Joti, Y.; Yamashita, A.; Tanaka, R.; Tanaka, T.; Luo, F.; Tono, K.; Hsu, K.-C.; Kiontke, S.; Schapiro, I.; Spadaccini, R.; Royant, A.; Yamamoto, J.; Iwata, S.; Essen, L.-O.; Bessho, Y.; Tsai, M.-D., Serial crystallography captures dynamic control of sequential electron and proton transfer events in a flavoenzyme. *Nature Chemistry* 2022, 14 (6), 677-685.
3. Maestre-Reyna, M.; Huang, W. C.; Wu, W. J.; Singh, P. K.; Hartmann, R.; **Wang, P. H.**; Lee, C. C.; Hikima, T.; Yamamoto, M.; Bessho, Y.; Drescher, K.; Tsai, M. D.; Wang, A. H., *Vibrio cholerae* biofilm scaffolding protein RbmA shows an intrinsic, phosphate-dependent autoproteolysis activity. *IUBMB life* 2021, 73 (2), 418-431.
4. **Wang, P.-H.**; Lee, C.-E.; Lin, Y.-S.; Lee, M.-H.; Chen, P.-Y.; Chang, H.-C.; Chang, I.-F., The Glutamate Receptor-Like Protein GLR3.7 Interacts With 14-3-3 ω and Participates in Salt Stress Response in *Arabidopsis thaliana*. *Frontiers in Plant Science* 2019, 10.
5. Huang, S. J.; Chang, C. L.; **Wang, P. H.**; Tsai, M. C.; Hsu, P. H.; Chang, I. F., A type III ACC synthase, ACS7, is involved in root gravitropism in *Arabidopsis thaliana*. *Journal of experimental botany* 2013, 64 (14), 4343-60.

CV – Scientific career

03/2020-04/2023 PhD thesis in the research group of Professor Dr. Lars-Oliver Essen, Department of Chemistry, Philipps-University Marburg
PhD project: Time-resolved crystallography on the structural dynamics of cryptochromes and photolyases
Major: Biochemistry

06/2016-12/2022 Research assistant in the research group of Assistant Prof. Dr. Manuel Maestre-Reyna and Prof. Dr. Ming-Daw Tsai, Institute of Biochemistry, Academia Sinica, Taiwan
Major: Biochemistry/Structure biology

Master studies

09/2011-12/2013 Institute of Plant Biology, National Taiwan University
Thesis: Functional study of phosphorylation-dependent interaction between 14-3-3 and glutamate receptor-like gene 3.7 in *Arabidopsis thaliana*
Supervisor: Prof. Dr. Ing-Feng Chang, Ph.D
Major: Plant biology

Bachelor studies

09/2007-06/2011 Department of Nutrition, Chung Shan Medical University
Thesis: Antioxidant analysis of common fruits and vegetables powders
Supervisors: Prof. Dr. Chin-Kun Wang, Ph.D
Major: Nutrition

Table of Contents

| | |
|--|----|
| List of publication | |
| CV-scientific career | |
| Zusammenfassung | 1 |
| Summary | 3 |
| 1. Introduction | 5 |
| 1.1 The cryptochrome/photolyase family (CPF)..... | 5 |
| 1.2 Structures of cryptochromes and photolyases..... | 7 |
| 1.3 Photoactivation of cryptochromes and photolyases.....- | 9 |
| 1.4 Isoalloxazine geometry of FAD..... | 11 |
| 1.5 Mechanism of DNA repair..... | 12 |
| 1.5.1 Mechanism of CPD repair..... | 13 |
| 1.5.2 Mechanism of (6-4)PP repair..... | 15 |
| 1.6 Time resolved crystallography by using X-ray free electron laser..... | 16 |
| 2. Objective of the thesis | 18 |
| 3. Material and Method | 19 |
| 3.1 Clone and site-directed mutagenesis..... | 19 |
| 3.2 Transformation..... | 19 |
| 3.3 Protein expression and purification..... | 19 |
| 3.4 <i>CraCRY</i> and its mutants protein crystallization..... | 20 |
| 3.5 6-4 DNA synthesis and hybridization..... | 20 |
| 3.6 <i>CraCRY</i> -DNA co-crystallization..... | 21 |
| 3.7 Steady-state UV/Vis spectroscopy and photoreduction assay..... | 21 |
| 3.8 Degassing and obtaining fully reduce state of <i>CraCRY</i> crystals under anaerobic conditions..... | 21 |
| 3.9 <i>CraCRY</i> crystals filtration and crashing..... | 22 |
| 3.10 <i>CraCRY</i> crystals embedding and injector building..... | 22 |
| 3.11 Data acquisition and on-site data processing at SACLA..... | 23 |
| 3.12 Off-site data processing and data extrapolation..... | 24 |
| 3.13 Structural refinement..... | 25 |
| 3.14 Generating difference density maps..... | 25 |
| 3.15 Data processing for KAMO..... | 26 |
| 3.16 Unit cell analysis for <i>CraCRY</i> mutants..... | 26 |
| 3.17 Time resolved in crystallo optical spectroscopy (TR- <i>icOS</i>)..... | 26 |
| 3.18 Cryo-trapping setup..... | 27 |
| 4. Results and discussion | 28 |
| 4.1 <i>CraCRY</i> signal transduction via time-resolved structural analysis..... | 28 |
| 4.1.1 Photoreduction overview in <i>CraCRY</i> | 28 |

| | |
|---|------------|
| 4.1.2 Structure changes between <i>CraCRY</i> 's dark-adapted, signaling and catalytic states..... | 29 |
| 4.1.3 Overall features of the C _{ox} to C _{signal} transition..... | 32 |
| 4.1.4 Changes in the isoalloxazine geometry..... | 35 |
| 4.1.5 Extrapolation and occupancies of time-solved datasets..... | 35 |
| 4.1.6 Observation of early events (10 to 100 ns)..... | 36 |
| 4.1.7 Observation of intermediate and late events (100 ns to 233 ms)..... | 37 |
| 4.1.8 E384 involves in proton transfer chain..... | 41 |
| 4.1.9 Time resolved in crystallo optical spectroscopy in <i>CraCRY</i> crystals..... | 42 |
| 4.1.10 Unit cell classification of the relevant actors..... | 43 |
| 4.1.11 <i>CraCRY</i> mutational analysis of the relevant actors in α 22 unraveling..... | 47 |
| 4.1.12 Conclusion and outlook..... | 49 |
| 4.2 Observing DNA post-repair dynamics in <i>CraCRY</i> -(6-4)PP complex..... | 51 |
| 4.2.1 Overview of (6-4)PP repair in <i>CraCRY</i> | 51 |
| 4.2.2 Structure solution of (6-4)PP repaired models..... | 52 |
| 4.2.3 Overall structural changes after (6-4)PP DNA repair..... | 54 |
| 4.2.4 Active site structural changes after (6-4)PP DNA repair..... | 56 |
| 4.2.5 Detailed structural changes of the BIR releasing..... | 58 |
| 4.2.6 Conclusion and outlook..... | 60 |
| 4.3. Protonation study on mutant <i>Methanosarcina mazei</i> class II DNA photolyase.... | 60 |
| 4.3.1 E407L preparation, crystallization and data acquisition..... | 61 |
| 4.3.2 <i>Mm</i> CPDII E407L mimics <i>CraCRY</i> behavior (transition from FAD _{ox} to FADH [*]) | 63 |
| 4.3.3 Possible mechanism of proton donation from solvent..... | 64 |
| 5. Perspectives..... | 65 |
| 6. References..... | 66 |
| 7. Appendix..... | 79 |
| 8. Acknowledgements..... | 101 |

Zusammenfassung

Photolyasen und Cryptochrome bilden eine Superfamilie (PCSf) von lichtgesteuerten Proteinen, die in allen Bereichen des Lebens vorkommen. Photolyasen reparieren UV-induzierte DNA-Läsionen, nämlich entweder Cyclobutan-Pyrimidin-Dimere (CPD) oder Pyrimidin-(6-4)-Pyrimidon-Photoprodukte, (6-4)PP. Die Cryptochrome haben größtenteils ihre DNA-Reparaturfunktionalität verloren und fungieren als Signalproteine, die verschiedene biologische Reaktionen auf Lichteinfall koppeln. Photolyasen und Cryptochrome haben enge evolutionäre Beziehungen und teilen beide eine gemeinsame Topologie, einschließlich der gleichen photoaktiven Regionen (FAD, Antennen-Cofaktoren). Während der Photoaktivierung kann FAD ein oder zwei Elektronen einfangen und in vier möglichen Redoxzuständen existieren: oxidiert (FADox), anionisches Semichinon-FAD-Radikal ($\text{FAD}^{\bullet-}$), radikalisch halbreduziert (Semichinon, FADH^{\bullet}) und vollständig reduziert (Hydrochinon, FADH^-). Blaulichtabsorption führt zum ersten Elektronentransfer zum inaktiven FADox Chromophor, was zur kurzlebigen $\text{FAD}^{\bullet-}$ Spezies führt, ein Zwischenprodukt zum langlebigen protonierten FADH^{\bullet} Zustand ist. Ein zweiter Elektronentransfer bildet den vollständig photoaktivierten Zustand, FADH^- , aus, der die DNA-Reparatur von CPD oder (6-4)PP Schäden katalysiert, indem ein Elektron vom angeregten $\text{FADH}^{\bullet-}$ auf die DNA-Läsion injiziert wird.

Die vorliegende Studie konzentriert sich auf die strukturellen Veränderungen mittels zeitaufgelöster serieller Femtosekunden-Röntgenkristallographie (TR-SFX), um zu beschreiben, wie Cryptochrome den Signalübertragungsmechanismus im tierähnlichen Cryptochrom aus der Grünalge *Chlamydomonas reinhardtii* (*CraCRY*) durchführen. *CraCRY* ist nicht nur ein Cryptochrom, sondern hat auch eine (6-4)-Photolyase-Funktion, d.h. ist zur Reparatur von (6-4)PP-Schäden. In *CraCRY* fungieren während des ersten lichtgesteuerten Zyklus drei Tryptophanreste und ein Tyrosin (Y373) als Elektronentransferkette, wobei Y373 das Elektron an das FAD abgibt, um das kurzlebige Radikalpaar (RP) $\text{FAD}^{\bullet-}/\text{Y373}^{\bullet+}$ zu erzeugen, das sich zum langlebigen $\text{FADH}^{\bullet}/\text{Y373}^{\bullet}$ RP durch Protonierung stabilisiert. Das Tyrosyl-Radikal löst eine Strukturänderung in der Region zwischen der Schleife, die den Tyrosyl-Radikal trägt, und der C-terminalen $\alpha 22$ -Helix aus, was zur anschließenden Entfaltung des C-Terminus führt. Während der Photoreduktion von *CraCRY* wurden 19 Schnappschussstrukturen durch TR-SFX erhalten, die zeigten, dass die Signaltransduktion in drei verschiedene Phasen vom ns- bis ms-Bereich erfolgte: (1) Stabilisierung des $\text{FAD}^{\bullet-}$ und $\text{Tyr}^{\bullet+}$ -Biradikals (ns), (2) Stabilisierung von $\text{FAD}^{\bullet-}$ über Protonentransfer (μs zu ms) und (3) C-terminale Entfaltung (ms zu s). Diese Ergebnisse zeigten erstmals einen detaillierten molekularen Mechanismus für die Cryptochrom-Photoaktivierung. Für die (6-4)PP-Reparatur gelang es, den Prozess via in-crystallo

Cryo-Trapping von Post-Illuminations-Zwischenprodukten vorläufig zu charakterisieren. Wir waren in der Lage, drei Stadien der komplexen Dissoziation mit atomarer Auflösung zu bestimmen: (1) Basenrelaxation innerhalb des aktiven Zentrums, (2) Basenrückkehr in Richtung der ungepaarten DNA-*bubble* und (3) DNA-Freisetzung aus dem aktiven Zentrum der (6-4)-Photolyase. Zur weiteren Untersuchung der Photoreduktion wurden Mutanten jedes relevanten Akteurs im Signalzustand sowohl spektroskopisch als auch kristallographisch charakterisiert. Diese Mutationen beeinflussten die Ausbildung des Signalzustands, wodurch die Rolle einzelner Aminosäuren während des *CraCRY*-Photozyklus charakterisiert wurde. Gegenwärtig ist der Reparaturmechanismus für die Reparatur von (6-4)PP DNA-Läsionen noch unklar. Zukünftige TR-SFX-Experimente werden in der Lage sein den gesamten Reparaturmechanismus für die (6-4)PP-Reparatur zeigen.

Summary

Photolyases and cryptochromes form a superfamily (PCSf) of light-directed proteins found in all areas of life. Photolyases repair UV-induced DNA lesions, namely either cyclobutane-pyrimidine dimers (CPD) or pyrimidine-(6-4)-pyrimidone photoproducts, (6-4)PP. The cryptochromes have mostly lost DNA repair functionality and act as signaling proteins coupling various biological responses to light input. Photolyases and cryptochromes have close evolutionary relationships sharing both a common topology, including the same photoactive regions (FAD, antenna cofactors). During photoactivation, FAD can capture one or two electrons and exist in four possible redox states: oxidized (FAD_{ox}), anionic semiquinone FAD radical ($\text{FAD}^{\bullet-}$), radical semi-reduced (semiquinone, FADH^{\bullet}) and fully reduced (hydroquinone, FADH^-). When blue light absorption drives first electron transfer to the inactive FAD_{ox} , resulting in a short-lived $\text{FAD}^{\bullet-}$ which is intermediate of long-lived protonated FADH^{\bullet} . Furthermore, the second electron transfer leads to the fully photoactivated state, FADH^- , which catalyze DNA repair of CPD or (6-4)PP by injecting an electron from excited FADH^{-*} onto the DNA lesion. This study focuses on the structural changes via time-resolved serial femtosecond X-ray crystallography (TR-SFX) to describe how cryptochromes perform signal transduction mechanism in animal-like cryptochrome from the green algae *Chlamydomonas reinhardtii* (*CraCRY*). However, *CraCRY* is not only a cryptochrome, but also has (6-4) photolyase function, meaning (6-4)PP repair. In *CraCRY*, during first light-driven cycle, three tryptophans and one tyrosine (Y373) act as an electron transfer chain, with Y373 donating the electron to the FAD to produce short-lived radical pair (RP) $\text{FAD}^{\bullet-}/\text{Y373}^{\bullet+}$, which evolves to the long-lived $\text{FADH}^{\bullet}/\text{Y373}^{\bullet}$ RP. The tyrosyl radical is triggering a structural change in the region between the loop carrying the tyrosyl radical and the C-terminal $\alpha 22$ -helix, and c-terminal unfolding afterwards. In the photoreduction of *CraCRY*, 19 snapshot structures were obtained, which showed that signal transduction occurred in three different phases in ns to ms: (1) stabilization of $\text{FAD}^{\bullet-}$ and $\text{Tyr}^{\bullet+}$ radicals (ns), (2) stabilization of $\text{FAD}^{\bullet-}$ via proton transfer (μs to ms), and (3) c-terminal unfolding (ms to s). These results demonstrated a detailed molecular mechanism for cryptochrome photoactivation. For (6-4)PP repair, we succeeded to preliminarily characterize via *in crystallo* cryo-trapping of post-illumination intermediates, immediately followed by data collection. We were able to determine three stages of complex dissociation at atomic resolution: (1) base relaxation within the active site, (2) base return towards the unpaired bubble and (3) DNA release from the (6-4)-photolyase active site. For further investigation of photoreduction, mutants of each relevant actor in the signaling state were characterized both spectroscopically and crystallographically. These mutations influenced the formation of the signaling state characterizing the role of individual amino-acids during the

CraCRY photocycle. For repairing DNA lesion, (6-4)PP repair mechanism is still not clear. Future TR-SFX experiments will show the whole repair mechanism for (6-4)PP repair.

1. Introduction

1.1 The cryptochrome/photolyase family (CPF)

Light is a very important environmental factor that controls many cellular responses in organisms. To use light energy, organisms rely on special photoactive enzymes called photoreceptors such as rhodopsin, melanopsin, phytochromes, phototropins and cryptochromes to absorb light at different spectral wavelengths and regulate cellular processes¹⁻³. The cryptochrome/photolyase family members can be categorized into two main groups based on their biological functions. In cryptochrome (CRY), the first CRY was identified as a blue light photoreceptor in *Arabidopsis thaliana*. The characterization of *Hy4* gene in *A. thaliana* mutant was indicated that *Hy4* encodes CRY and responsible for inhibition of hypocotyl elongation under blue light illumination⁴. Afterwards, many studies of CRYs were discovered in other plant species and involved in plant growth and development⁵⁻⁶. In addition, CRYs have been reported to be photoreceptors for the circadian clock in fruit fly (*Drosophila melanogaster*) and through conformational change by light exposure to start a signaling pathway leading the resetting of the molecular clock⁷⁻⁸. However, the biological function in photolyase (PHR) is mainly to absorb blue light energy to repair UV-induced DNA lesions. The DNA lesions have two major types: cyclobutane pyrimidine dimers (CPDs) and pyrimidine–pyrimidone (6–4) photoproducts ((6-4)PP)⁹⁻¹⁰ (Figure 1).

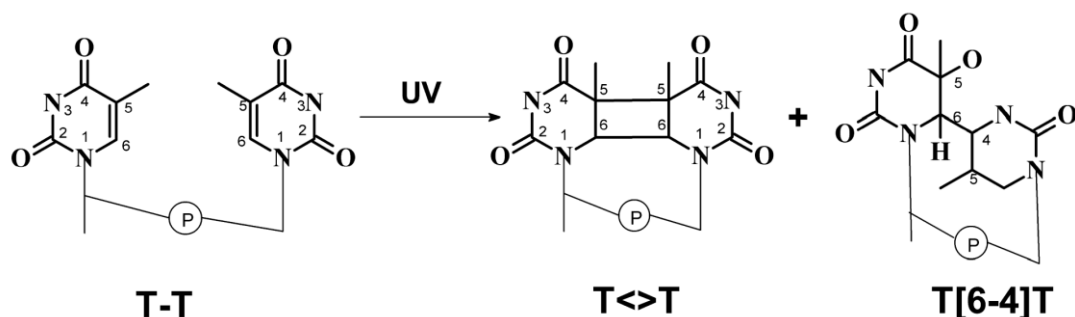


Figure 1. The common UV-induced DNA lesions. Adapted from Ref. (10). Two major types of compounds resulting from DNA damage are formed: pyrimidine cyclobutane dimers (CPDs) and pyrimidine-pyrimidone (6-4) photoproducts. CPD lesion is the product of a [2+2] cyclo-addition, whereas (6-4)PP is formed by an oxetane intermediate¹¹.

As CPF is widely and diverse protein family, different ancestors and species of cryptochrome and photolyase are classified into many subgroups. Recently, a phylogenetic tree of over 200 total sequences was analyzed by MEGA7 program¹² (Figure 2), and the total sequence data were included with previous studies from GenBank (NCBI) and the groups not analyzed in previous studies¹³⁻¹⁴. Phylogenetic analysis separated the sequences into 10 subgroups: Class I, Class II and Class III CPD PHRs; (6-4) PHRs; ssDNA PHRs (previously called CRY-DASH); plant CRYs; Type-1, Type-2 and Type-4 CRYs; and sponge CRYs (representing animal CRYs)¹². The Class I PHR were found mostly in unicellular organisms (e.g. *E-coli*) and Class II PHR were found in both unicellular and multicellular organisms (e.g. *Drosophila*). Class III PHR only found in some eubacteria¹⁵. Interestingly, the single stranded DNA photolyase (ss PHR), previously misclassified as CRY-DASH (Cryptochrome-Drosophila, Arabidopsis, Synechocystis, Human), is renamed by Ozturk¹² to Class 0 PHRs because they are CPD PHRs but repair damage only on single-stranded DNA¹⁶. Currently, CRYs are classified as plant CRY and animal CRYs (Type 1, Type 2, and Type 4). Plant CRYs are phylogenetically more similar to CPD PHR as well as (6-4)PHR are very similar to animal CRYs¹⁷. The difference of Type 1 and Type 2 CRYs are their biological functions. Type-1 CRYs acts as a photoreceptor for resetting of the circadian clock¹⁸ and Type-2 CRYs are involved in the core clock¹². In addition, function of plant CRYs are inhibition of stem elongation, stimulation of leaf expansion, and control of photoperiodic flowering¹². In plants, the model organism is *Arabidopsis*. *Arabidopsis* CRY1 and CRY2 play a essential role in the reset of the core circadian clock^{4, 19}. Moreover, by light exposure in *AtCRY2*, *AtCRY2* is degraded by the proteasome system and has no autokinase activity²⁰. In contrast, *AtCRY1* is not degraded following light exposure and has autokinase activity that is unaffected by blue light⁴. Another group of CRYs, I-CRY (Type-0 CRY), which function as light-sensing role in the primordial eyes of opsin-less sponge larvae to assist settlement¹³. I-CRYs allows light signals into glass fiber network in the siliceous skeleton of sponges²¹⁻²² and proposed that photon signals are converted into radicals²³.

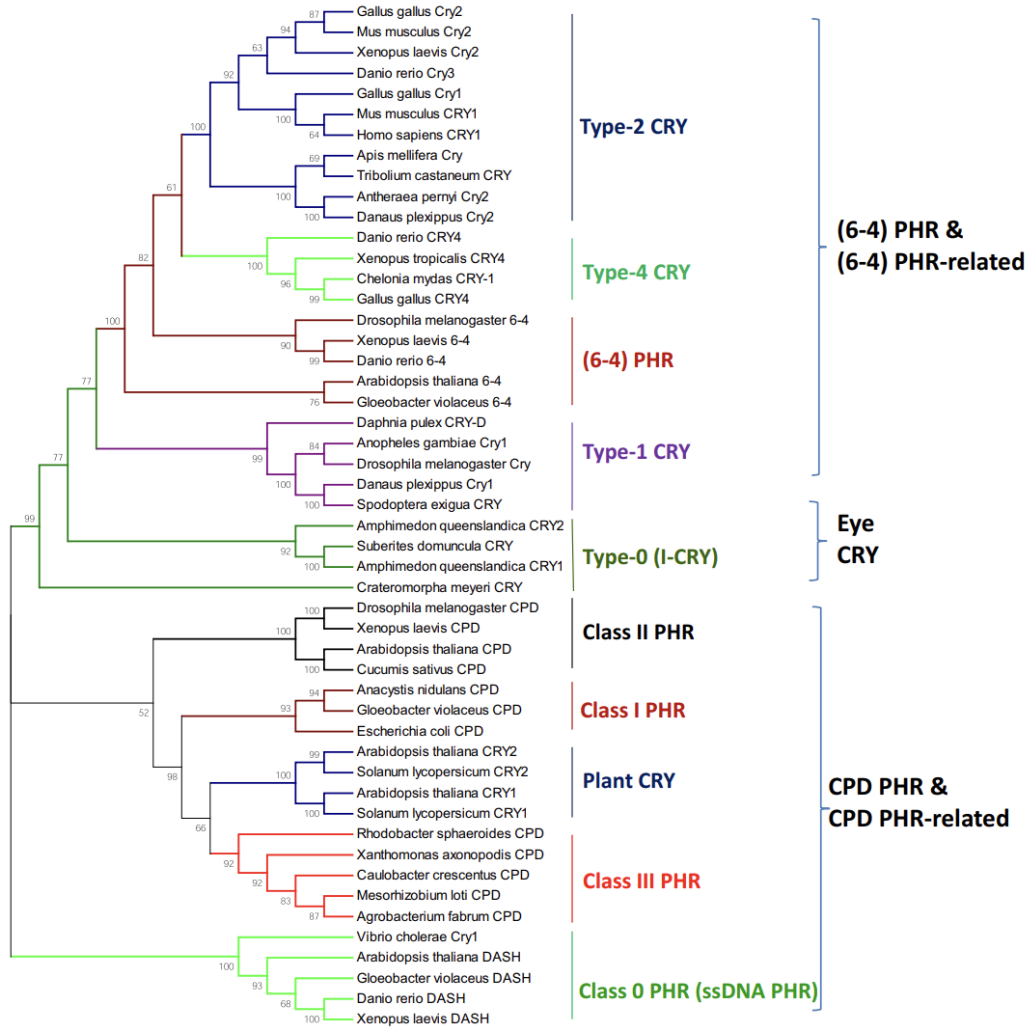


Figure 2. Phylogenetic classification of CPF from Ozturk¹². Adapted from Ref. (12). The total PHR and CRY sequences were aligned by using ClustalW and for further analysis. The evolutionary history was concluded by using the maximum likelihood method and based on the model of Le and Gascuel²⁴. Ten major subgroups were identified and classified to 3 major groups, including a novel group of CRYs (Type-0 CRYs or I-CRYs) from sponges.

1.2 Structures of cryptochromes and photolyases

The Protein Data Bank (PDB) is a database for the three-dimensional structural data of large biological molecules. Nowadays, several crystal structures of photolyase and cryptochrome proteins are available. The first CPD photolyase crystal structures were obtained from *Escherichia coli* in 1995²⁵ and *Anacystis nidulans* in 1997²⁶ which lack of the respective DNA substrates. Comparison of crystal structures of CPF, they have shown very similar structural features. The N-terminal consists of an α/β domain, which is a typical dinucleotide-binding domain, and often binds an auxiliary chromophore as light-harvesting antenna. The C-terminal (α -helical) domain is composed only by several α -helices and harbors the main chromophore, flavin-adenine-dinucleotide (FAD) cofactor, that is essential for light-dependent catalysis (Figure 3A). In *E. coli* CPD

photolyase, not only 5,10-methenyl-tetrahydrofolate (MTHF) is observed in the cleft between the two domains but also it has reported that the main chromophore, FAD, is held in a U-shaped conformation by interaction with 14 conserved amino acid residues¹⁷.

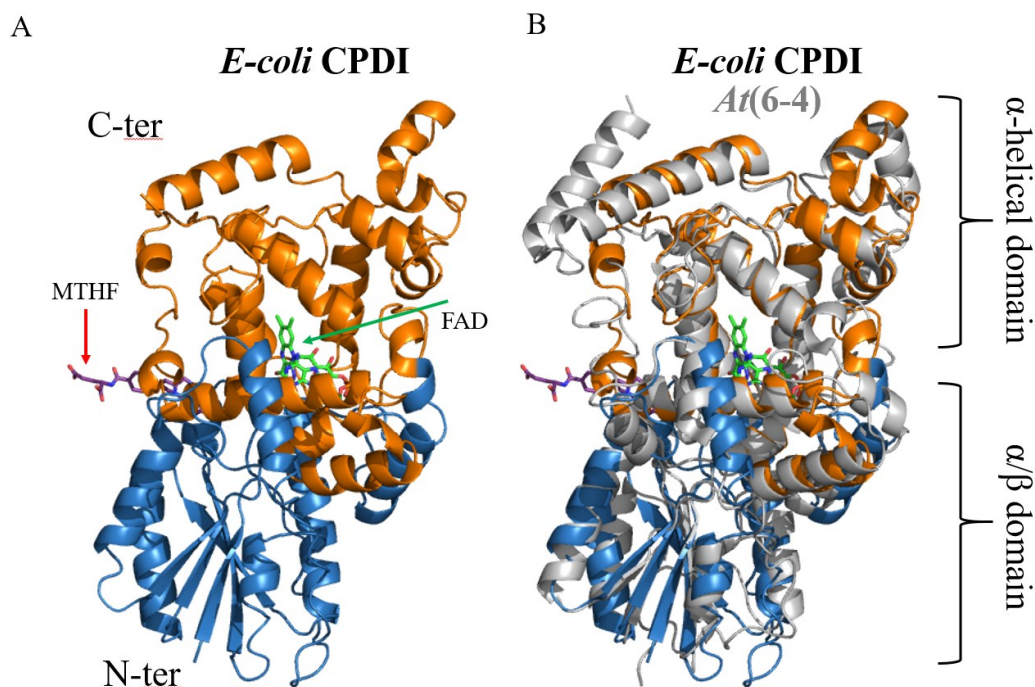


Figure 3. 3D structure of cryptochrome/photolyase family. (A) *E. coli* CPD class I photolyase (1DNP) has shown two antenna chromophores and FAD is bound in a U-shaped conformation. (B) Structural alignment between *Ec*CPDI and *At*(6-4) photolyase (3FY4) shows high structural similarity.

Besides, the second antenna chromophore has reported to function for broadening absorption in the visible spectral region²⁷. So far, several kinds of antenna chromophores have identified (Figure 4A), including 8-hydroxydeazaflavin (8-HDF)²⁸, 5,10-methenyltetrahydrofolate (MTHF)²⁹, flavin mononucleotide (FMN)³⁰ and 6,7-dimethyl-8-ribityllumazine (DLZ)³¹. Interestingly, in *Sulfolobus tokodaii*, a second FAD molecule was also found in the antenna binding pocket³². These cofactors have an absorption in a spectral range between 380 and 420 nm.

Despite the overall structures of photolyases and cryptochromes are similar, the main difference between them is that cryptochromes have an additional C-terminal extension (CTE) region that varies largely in different CRY groups (Figure 4B)^{10, 33}. Previous studies have demonstrated that the C-terminal of *A. thaliana* CRY mediate blue light signals by interaction with COP proteins³⁴⁻³⁵. In addition, the *Drosophila* CRY (*DmCRY*) transmits the blue light signal by interacting with TIM proteins³⁶, and proven that the C-terminus of *DmCRY* is intimately involved in phototransduction. Several studies have shown that *DmCRY* mediates the response to blue light and 19 amino acids

of C-terminal were required for inhibition of the CRY-TIM interaction in the dark³⁷⁻³⁸. However, in *Xenopus laevis* and mammalian CRY1 and CRY2, the CTE is not necessary for circadian clock function, but deletion of the C-terminus causes a different nuclear localization mechanism³⁹⁻⁴⁰. Furthermore, phosphorylation of the CTE regulates mouse CRY1 stability and contributes to the proper circadian period length⁴¹⁻⁴².

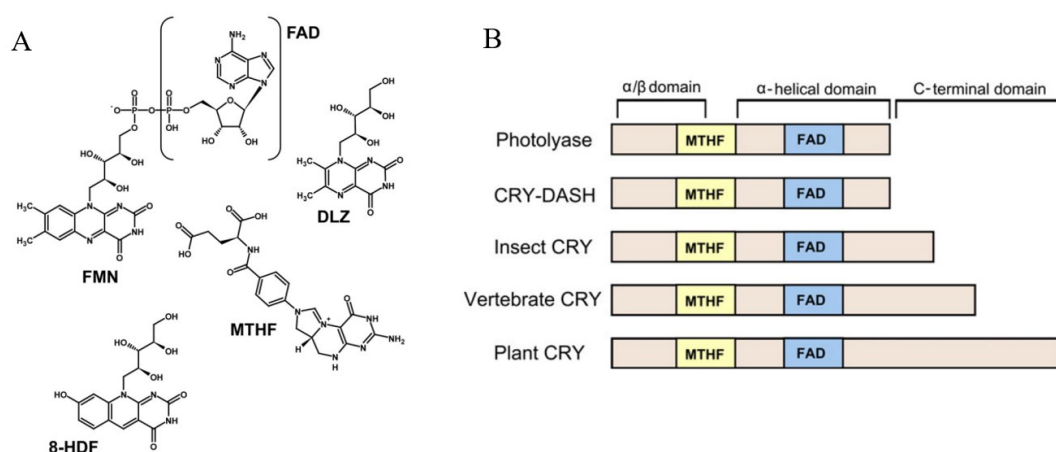


Figure 4. (A) Overview of the different antenna chromophores that have been proved within the photolyases and cryptochromes. (B) Schematic scheme of CPF proteins¹⁰. Adapted from ref. (10). According to different types of CPF member, the total lengths range from 500 to 700 amino acids. In addition, most CRYs have C-terminal extensions from 30 to 300 amino acids. Main antenna chromophores of all CPF members are associated with the FAD cofactor of the α -helical domain.

1.3 Photoactivation of cryptochromes and photolyases

Photoactivation is a reaction common to cryptochromes and photolyases, involving electron transfer (ET) and flavin reduction. In general, flavins usually exist in the oxidized state. The non-covalently bound FAD of flavoproteins may exist in any one of the three states in five different kinds of forms: the fully oxidized FAD_{ox} , the semiquinone state as anionic radical $\text{FAD}^{\bullet-}$ or neutral radical FADH^{\bullet} and the fully reduced hydroquinone state as FADH^- or FADH_2 ⁴³⁻⁴⁴ (Figure 5). FAD reduction is accomplished via two light-driven, subnanosecond, single electron transfer events, which reduce FAD from its oxidized state (FAD_{ox}) to FADH^- . In photolyases, only FADH^- is then capable to catalyze light-induced DNA repair⁴⁵⁻⁴⁸. *Arabidopsis* CRY1 and CRY2 cryptochromes have been the most extensively investigated and the ground state of FAD in *AtCRY1* and *AtCRY2* appears to be the fully oxidized state, FAD_{ox} ⁴⁹⁻⁵². Under anaerobic conditions, the FAD chromophore of *AtCRY1* gets photoreduced to the semiquinone state with blue light and further absorbs green light to become the fully reduced state⁵²⁻⁵⁴. In addition, studies on type1 cryptochrome from insects, including fruit flies (*Drosophila melanogaster*)⁵⁵⁻⁵⁶, migratory birds (*Sylvia borin*)⁵⁷

and mammals⁵⁸, suggested that the resting state of flavin is the oxidized state, except for the monarch butterflies (*D. plexippus*), which adopts the semiquinoid $\text{FAD}^{\bullet-}$ form⁵⁹.

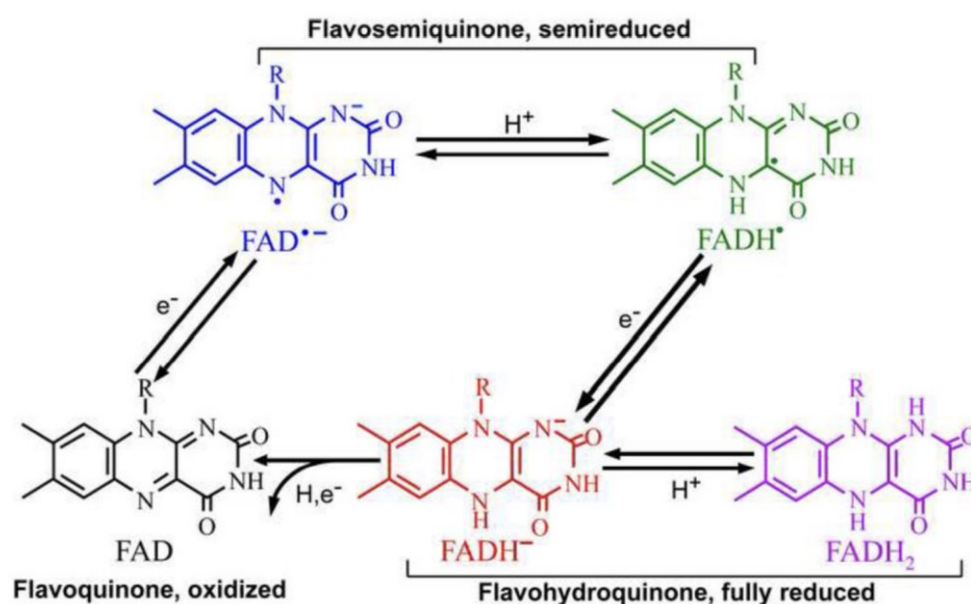


Figure 5. Five possible redox forms of flavins in the photocycle are shown⁴⁴. Adapted from ref. (44). The two different forms of semiquinone radicals: anion radical ($\text{FAD}^{\bullet-}$) and neutral radical (FADH^{\bullet}), and two forms of reduced flavins: protonated hydroquinone (FADH_2) and anionic hydroquinone ($\text{FADH}^{\bullet-}$) are shown. R indicates the ADP-ribityl moiety of FAD. After absorption of light, FAD_{ox} abstracts an electron to form the semiquinone state, first as $\text{FAD}^{\bullet-}$ than as FADH^{\bullet} . By further light-driven electron transfer, the fully reduced state, $\text{FADH}^{\bullet-}$, can be formed.

Upon light excitation, the excited flavin (FAD_{ox}^*) abstracts an electron from a nearby (proximal) tryptophan, which is part of the highly conserved Trp triad (Figure 6A)^{27, 60-62} for allowing further charge separation to form a short-lived pair of the anionic semiquinone radical and the cationic tryptophan radical ($\text{FAD}^{\bullet-}/\text{TrpH}^{\bullet+}$). This electron transfer chain of Trp triad can be found in almost all members of the CPF. In the *Escherichia coli* DNA photolyase, the electron is abstracted from the proximal Trp, W382, to the FAD to form the initial radical pair of $\text{FAD}^{\bullet-}/\text{TrpH}^{\bullet+}$. This tryptophanyl radical is further stabilized by deprotonation and takes an electron from the medial Trp, W359, to form the secondary of radical pair of $\text{FAD}^{\bullet-}/\text{Trp}^{\bullet60, 63}$. It abstracts an electron from the distal Trp, W306, afterwards; the latter Trp^{\bullet} radical is then reduced by an exogenous electron donor (Figure 6B)⁶⁴. All of these electron transfer events happen in the picosecond time scale⁶⁴⁻⁶⁵. Besides, but less frequently, a Trp tetrad has been also found⁶⁶⁻⁶⁷. A fourth tryptophan (or tyrosine) is usually found in animal cryptochrome, animal (6-4) photolyases (Figure 6C) and may be of importance for the magnetoreceptive properties of some of these cryptochromes⁶⁷.

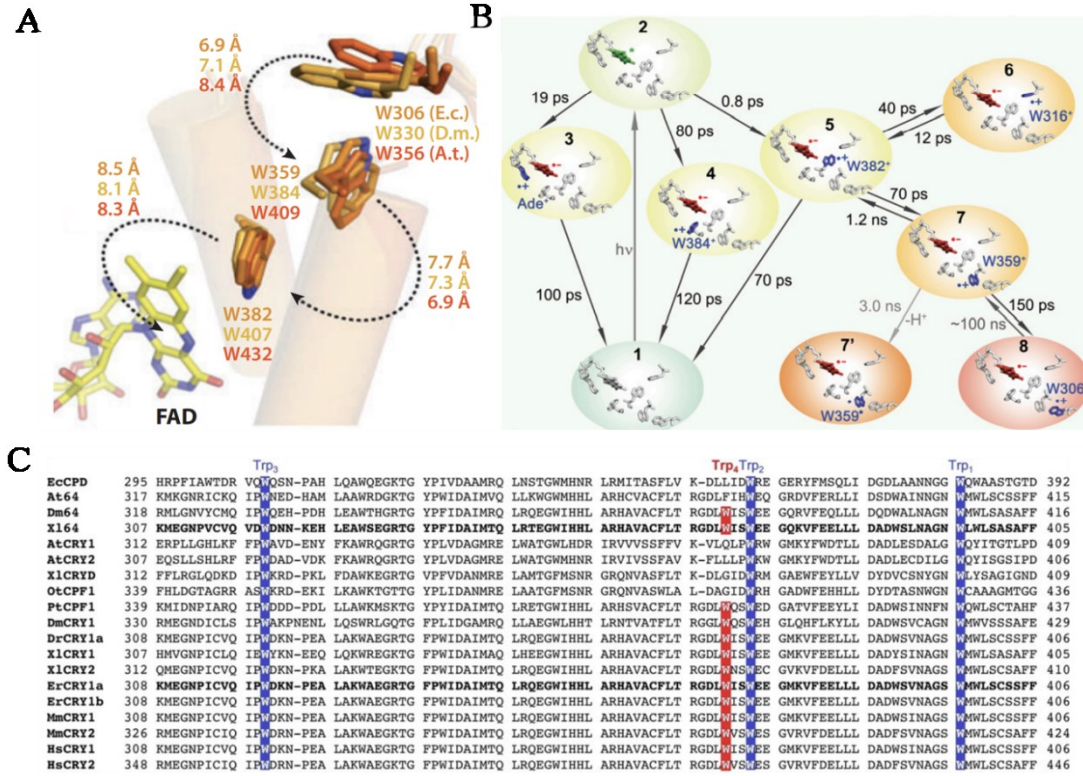


Figure 6. (A) Structural comparison of electron transfer chain in cryptochromes and photolyases²⁷. Adapted from ref. (27). The conserved tryptophan triad of *Escherichia coli* DNA photolyase, *Drosophila melanogaster* (6–4) photolyase, and *Arabidopsis thaliana* cry3 are superimposed. Electron transfer distances are shown by center to center. (B) Timescales of the Trp-triad electron transfer reaction in EcCPD⁶⁴. Adapted from ref. (64). There are 12 electron transfer reactions for each step. 1>2 represents the FAD_{ox} getting photoexcited. 2>3 represents the electron transfer in adenine. 2>5, 5>8 and 7>8 represent the Trp triad flow to the active site. 2>4 means the electron transfer between FAD_{ox}* and W384. 5>6 shows the electron transfer between W316 and W382. 3>1, 4>1, 5>1, 7>5, and 8>7 represent the reorganization of electron transfer. (C) Partial protein sequence alignment of several CPF⁶⁶. Adapted from ref. (66). The conserved Trp triad are high-lighted in blue. The fourth tryptophan is shown in red.

1.4 Isoalloxazine geometry of FAD

In the past 30 years, the flavin redox chemistry of photolyases has been extensively characterized via several spectroscopic and theoretical studies^{27, 65, 68–69}. However, spectroscopic characterization provides very little information on flavin geometry, including electronic transitions of the flavin species and electron transfer chain. On the other hand, flavin radical intermediates are too short-lived for conventional crystallography. In terms of the FAD isoalloxazine geometry, a theoretical study found different isoalloxazine conformational changes, mostly the so-called “butterfly bending”, that is defined by the angle (α) between the normal vectors of the A and C ring planes of isoalloxazine⁷⁰. According to α values, approaching to zero degrees represents an oxidized flavin state and 15–25° a reduced hydroquinoid state in several

flavoproteins⁷¹⁻⁷². Recently, our study used *Methanosarcina mazei* class II DNA photolyase (*MmCPDII*) as flavoenzyme target and was able to track the isoalloxazine moiety changing in real time⁷³. Unlike the α angle, we introduced the dihedral angles ρ_C and ρ_N , which together can discriminate between longitudinal twisting (bending along the long axis crossing the A, B and C rings) and lateral bending (bending along the short N5–N10 axis)(Figure 7A)⁷³. In addition, if $\rho_C \approx \rho_N$, then they correspond to α , suggesting that butterfly bending happens. In contrast, if $\rho_C \neq \rho_N$, a twist is indicated of the isoalloxazine moiety. During FAD_{ox} to $\text{FAD}^{\bullet-}$ transition, ρ_C values change from 10ns, reaching a maximum at 10 μs , meanwhile ρ_N values follow the same pattern but with milder changes, suggesting a twist (Figure 7B)⁷³. After 125 μs , the reoxidation takes over. During FADH^{\bullet} to FADH^- , the ρ_C and ρ_N dihedral angles increase together with time and reach a maximum at 300 ns, indicating butterfly bending, and reoxidation follows afterwards.

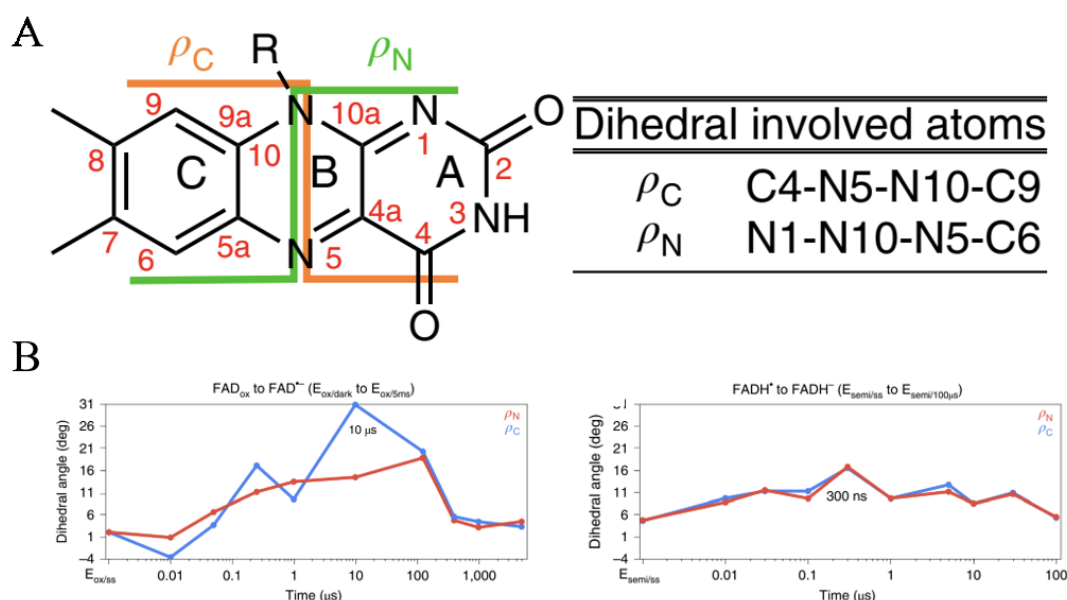


Figure 7. (A) Isoalloxazine ring structure with definition of the pseudo-dihedral angles ρ_C (orange) and ρ_N (green)⁷³. Adapted from ref. (73). ρ_C is composed by C4-N5-N10-C9 and ρ_N is composed by N1-N10-N5-C6. (B) Evolution of ρ_C (blue) and ρ_N (red) dihedral angles over time for each transition step of photoreduction, respectively.

1.5 Mechanism of DNA repair

The ultraviolet component in sunlight can cause damages of DNA by inducing formation of a cyclobutane pyrimidine dimer (CPD) and the less-frequent pyrimidine-pyrimidone (6–4) photoproduct (6–4PP), which are repaired by distinct photolyase families with specific repair mechanisms. To repair the damage of DNA, the fully reduced state FADH^- is required, as it is the only redox state capable of an initial electron transfer to the DNA lesion. These mechanisms will be described in the following.

1.5.1 Mechanism of CPD repair

In the past three decades, DNA repair by photolyases and their mechanism have been investigated extensively^{65, 69, 74-77}. CPD photolyase is the first enzyme system which was mapped out in real time for its entire catalytic dynamics and functional evolution. In *Anacystis nidulans* photolyase⁷⁵, FADH⁻ and the repaired CPD are linked by an electron tunneling pathway during repair (Figure 8A)⁷⁵. Six elementary reactions in the catalytic repair were completely characterized, and the reaction timescales were determined via femtosecond-resolved spectroscopy^{74, 78}. The complete photocycle of CPD repair is depicted in Figure 8B⁷⁵. Upon photoexcitation, the first reaction is the forward electron transfer (FET) from the excited flavin (FADH^{-*}) to the CPD in an average time of 250ps to generate the FADH[•] and T[•] radical pair^{74, 79}. The second reaction is the C5-C5' bond splitting dynamics within a few picoseconds to form FADH[•] and T-T[•]. The next reaction is the C6-C6' bond splitting in ~90 ps to form FADH[•] and T+T[•] or, alternatively, back electron transfer (BET) within 2.4 ns without repair. The latter reaction, the electron return occurs also in 700 ps after dimer repair, leading to the restoration of the second intact base and the catalytically active FADH⁻ (FADH⁻ and T+T). The repaired DNA is released from photolyase in 50 μ s⁸⁰, and the photolyase is ready to bind and repair another CPD DNA lesion. The whole photorepair mechanism of photolyases depends on the energy of a blue light photon to power the cyclic electron transfer between the flavin and the UV-damaged CPD.

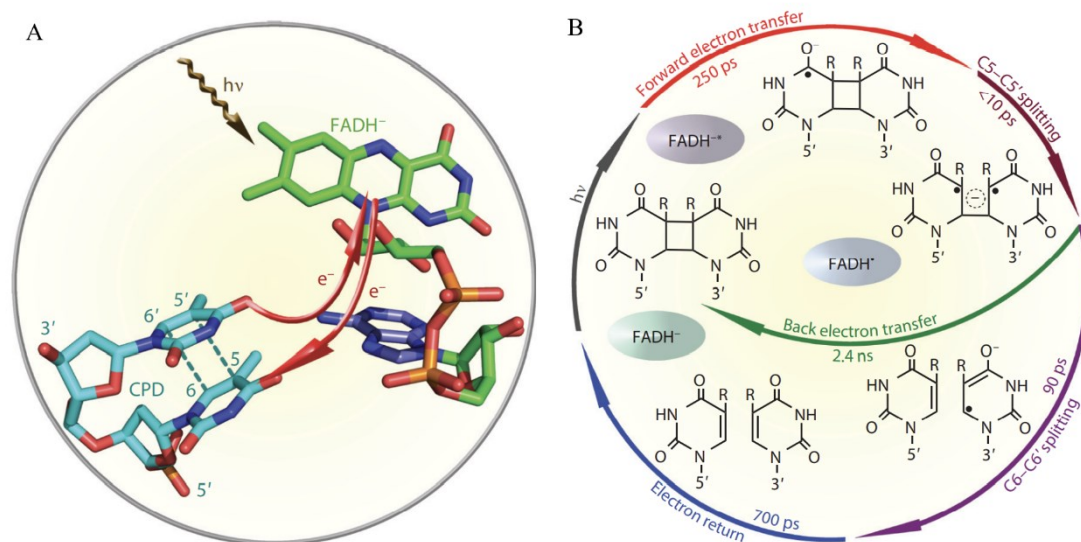


Figure 8. (A) Close view of relative positions in the active site of *Anacystis nidulans* photolyase between CPD and FADH⁻ with the electron tunneling pathways⁷⁵. Adapted from ref. (75). (B) Entire photocycle of CPD repair by photolyase⁷⁵. Adapted from ref. (75). Ultrafast time scales are shown for all elementary steps of the molecular mechanism.

Although the crystal structures of photolyases from different subfamilies show high similarities, several differences in FADH⁻ and DNA recognition, electron transfer

pathway and different reaction rates cause to form different repair quantum yields⁸¹. The repair quantum yields of different photolyases vary from 0.32 to 0.88⁸¹. The class I *Ec*PL (0.82) and *An*PL (0.88) have the highest reported quantum yields, whereas class II, III and ssDNA PLs have considerably lower quantum yields⁸¹.

However, it is still not clear how CPD repair by photolyases is realized in its structural details. Recently, our research consortium has used a structurally well-defined model system from previous studies to serve as base for time-resolved serial femtosecond X-ray crystallography to visualize the full catalytic process in real time and at atomic resolution (Maestre et al., Science under revision). This study used the *Methanosarcina mazei* class II DNA photolyase with dsDNA comprising a single CPD lesion as a target and uncovered ordered breaking of the covalent C-C bonds, opening of the cyclobutane ring, intermediates for enzyme recovering, repaired product release from the active site and pairing with their complementary bases (under revision).

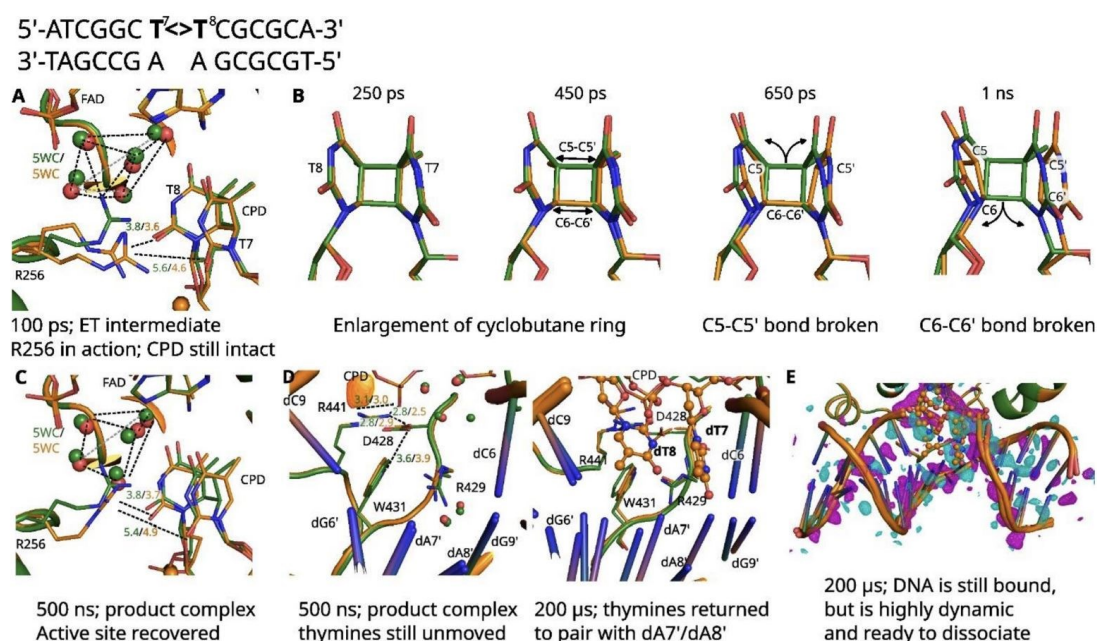


Figure 9. Selective intermediates at different stages of the repair process are shown (under revision). (A) The 100 ps structure where the forward electron transfer from FADH^- to CPD takes place. The active site R256 turned dynamic and moved to stabilize CPD. (B) Four intermediates in the ring opening of CPD, starting with elongation of C5-C5' and C6-C6' bonds (250-450 ps), followed by C5-C5' splitting (650 ps) and then C6-C6' splitting (1 ns). (C) At 500 ns, the R256, five water clusters and FADH^- of active site return to their resting state conformations. (D) The thymine bases are still flipped out at 500 ns, but start to return in the microsecond range and reach and pair with their adenine complementary bases at 200 μs. (E) Partial reannealed dsDNA is still bound to the enzyme but the DNA-protein interface is highly dynamic. Massive difference maps have shown positive maps in cyan and negative maps in magenta color. Each intermediate structure is overlaid with the structure of the dark state (green).

1.5.2 Mechanism of (6-4)PP repair

Like the CPD photolyases, (6-4)-photolyase for repair on the FAD cofactor in its fully reduced state. However, measured quantum yields of photorepair of (6-4)PPs was found to be around 4-100 times lower than CPD repair⁸²⁻⁸³. The (6-4)PP repair mechanism is still under debate⁸⁴⁻⁸⁷. An early (6-4)PP repair mechanism by (6-4)-photolyases that was proposed implies a reaction via formation of an oxetane intermediate in the active site. Catalysis is here driven by two conserved histidine residues⁸⁴, H354 (His₁) and H358 (His₂) in *Xenopus laevis* (6-4) photolyase. Photo-induced electron transfer from flavin to the oxetane moiety occurs like for the CPD photolyases with subsequent cleavage of the intra-dimer bonds and return of the excess electron to the flavin⁸². However, this mechanism was disproven by the co-crystal of *Drosophila melanogaster* 6-4 photolyase with (6-4)PP (3CVU) as there was no oxetane intermediate formed in the dark¹¹. In 2017, one review has summarized three different mechanisms, which are simple OH transfer, proton-transfer-steered OH transfer and a two-photon mechanism (Figure 10)⁸⁸. In simple OH transfer, forward electron transfer from photoexcited FADH^{•*} to (6-4)PP forms the 5' base radical anion (intermediate IIa), and His₁ remains in the neutral protonation state to help the stabilization of O4'H⁸⁹. The O4'H group then moves spontaneously from C5 to C4', followed by spontaneous cleavage of the C6-C4' bond and electron return to FADH^{•*}⁸⁹. In the proton-transfer-steered OH-transfer mechanism, Faraji *et al.* discussed and developed several plausible schemes^{85, 90-91}. Compared to the simple OH transfer mechanism, His₁ was assumed to be protonated. The two different forward electron transfer scenarios were from photoexcited FADH^{•*} either to the 5' base anion radical of the lesion (IIb) or first localized on His₁ (IIb') and then to the lesion⁹². After proton transfer (IIIb), the O4'H group would be transferred from C5 to C4', and followed by cleavage of the C6-C4' bond. Finally, the proton returns to His₁ and the excess electron to FADH[•]. However, in this mechanism, the highest energy barrier of OH transfer is about 20 kcal mol⁻¹. Further theoretical studies on this activation barrier came to values of 16 kcal mol⁻¹ or lower⁹⁰. The third mechanism implies a requirement for two photons, i.e. two cycles of photoexcitation. The first two reaction steps are very similar to the proton-transfer-steered OH transfer. Instead of O4'H group being transferred directly, the O4' atom forms a bond with C4' while keeping its bond with C5. The excess electron is returned and an oxetane intermediate is formed with fully reduced flavin FADH⁻ and the protonated His₁. Upon the second photon excitation, an oxetane radical anion (Ox^{•*}) is formed, that spontaneously splits its C5-O4' bond and finally undergoes the breakage of the lesion. The highest barrier in the second photoreaction would be about 9 kcal mol⁻¹.

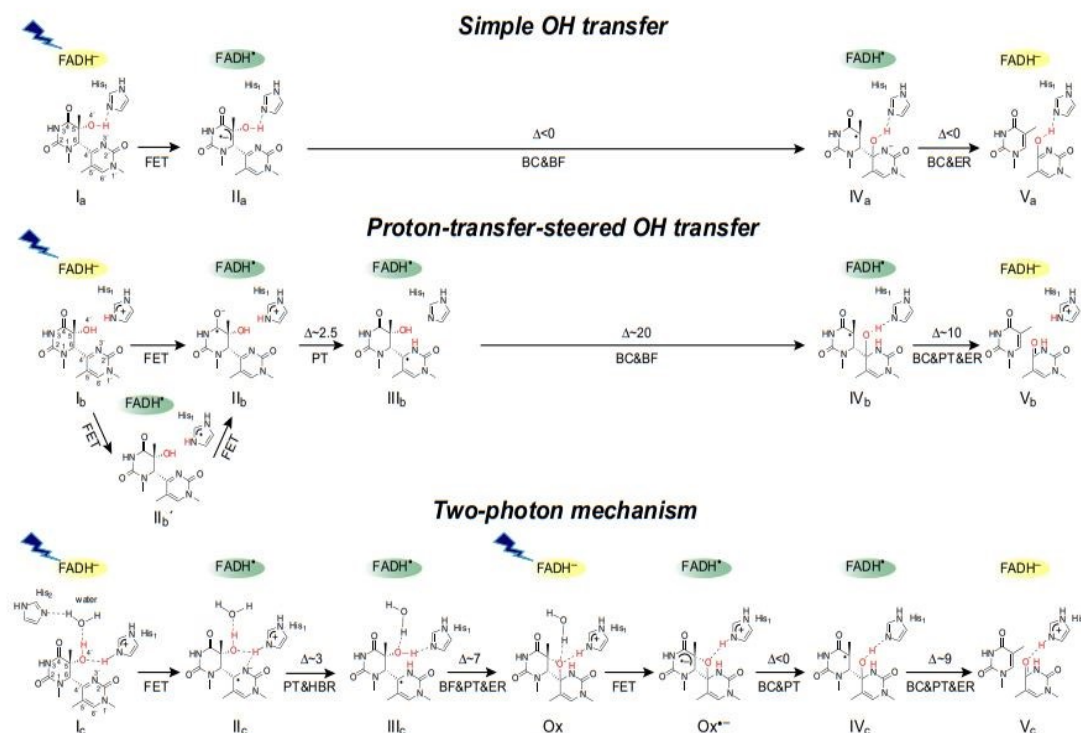


Figure 10. Three theoretical mechanisms for (6-4)PP repair by (6-4) photolyase⁸⁸. Adapted from ref. (88). The reaction of upper row (simple OH-transfer) is proposed by Domratcheva et al.^{89, 93}. The OH group transfer directly and supported by non-protonated His₁. The middle row (proton-transfer-steered OH transfer) is proposed by Faraji et al.^{85, 90-91}. His₁ is protonated and forward electron transfer either from the excited flavin to the lesion or through His₁. The anionic radical is formed at 5' base, following protonation of N3'. After the OH group transfer, the proton returns back to His₁ and electron return are occurred. The lower row (two photon mechanism) was proposed by Sadeghian et al.⁸⁷. In the beginning steps, after forward electron transfer of first photoexcitation, His₁, His₂ and a water molecular support to stabilize the anionic radical formation, and His₁ protonated. After proton transfer and electron return, the ground state of oxetane intermediate (Ox) forming. By the second photoexcitation, the oxetane radical anion is formed and abstracts a proton from His₁. The repaired has completed afterwards. FET = forward electron transfer; ER = electron return; PT = proton transfer; BC = bond cleavage; BF = bond formation; HBR = hydrogen bond reorganization; Δ = barrier in kcal mol⁻¹.

1.6 Time resolved crystallography by using X-ray free electron laser

The X-ray free-electron laser (XFEL) has been developed for high resolution structure analysis using X-ray pulses with a large number of photons of ultrashort duration⁹⁴⁻⁹⁵. The SPring-8 Angstrom Compact free-electron LAser (SACLA) is an XFEL located in Harima, Japan. In March 2012, SACLA started user operations at the first compact XFEL facility. The XFEL of SACLA is a combination of a linear accelerator, a long undulator line and optical lasers to generate electromagnetic radiation with very high intensity and brightness⁹⁶. The electrons are produced by an electron source, followed by a linear electron accelerator to amplify the energy of electron beam before it gets

injected into the undulator. The undulator is composed by many dipole magnets, which can make the “SASE” (self-amplified spontaneous emission) process occurring⁹⁷. The SASE process causes the intensity of the radiation to grow exponentially to the point of saturation. Because of the periodic magnetic field, the electron beam can be converted into an X-ray pulse with an ultrashort wavelength. SACLA has been providing user support with stable XFEL including around 10^{12} photons per pulse and an ultrashort duration below 10 femtoseconds^{96, 98}. Surprisingly, with ultrashort pulse duration and very high energies, diffraction patterns can be collectable by taking “snapshots” in a random orientation from microcrystals before the crystals are destroyed. Computer simulations by Neutze *et al.* proposed that XFELs could overcome X-ray damage by femtosecond X-ray pulses and able to detect X-ray damage-free images of molecules⁹⁹. To study high resolution of dynamic structural changes on ultrashort time-scale at room temperature, time-resolved serial femtosecond crystallography (TR-SFX) has been performed and combined with XFEL¹⁰⁰⁻¹⁰². To obtain time-resolved data, the microcrystals or nanocrystals flow from the top, followed by a laser pump pulse triggering the optically active crystals and hitting same crystal by the XFEL probe pulse after a time-delay Δt (Figure 11)¹⁰³. With different time delays Δt , the crystals can undergo different time periods for conformational evolution after the pump pulse and provide thereby an opportunity to watch the structural changes in real time.

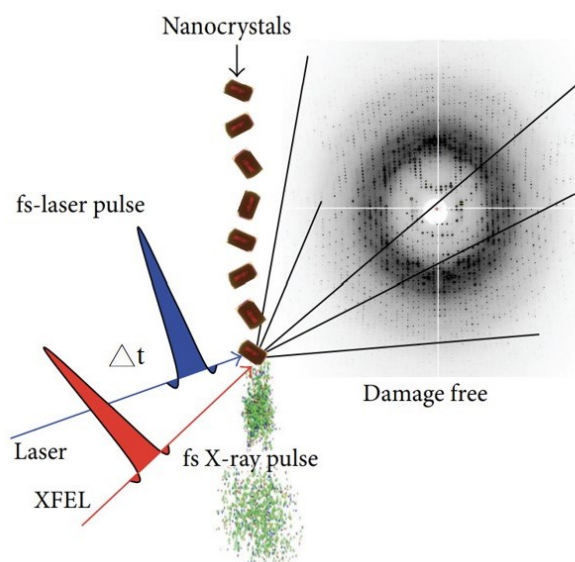


Figure 11. Time-resolved pump-probe experiment with serial femtosecond crystallography¹⁰³. Adapted from ref. (103). The setup can be used to stimulate photosystem I and II (PSI and PSII), photoactive yellow protein (PYP), bacteriorhodopsin (bR), myoglobin (Mb) or to activate caged substrates.

During data collection, tens of thousands of diffraction patterns from crystals in random orientations are required to obtain a structure at a resolution of a few angstroms. Therefore, the method of media as a carrier mixed with microcrystals has been developed to get a continuous and stable flow of crystals. As a good media, it has advantage of viscous enough and reduce sample consumption, such as lipidic cubic phase (LCP)¹⁰⁴, grease matrix¹⁰⁵ and vaseline (petroleum jelly)¹⁰⁶. However, some

media produce stronger X-ray scattering which increases background noise. To reduce background scattering from the carrier media, hydroxyethyl cellulose with low background scattering intensity has been introduced¹⁰⁷. Furthermore, as some sample materials suffer from grease-based matrices such as oil-sensitive proteins, the water-based hyaluronic acid matrix provides an alternative as crystal carrier¹⁰⁸.

2. Objective of the thesis

The biology of light sensing is mediated by photoreceptors, proteins carrying small photosensitive molecules called chromophores. The light-induced structural changes in the chromophore are detected by the protein moiety which is then responsible for transducing the signal towards downstream effectors. Cryptochromes are a well-known class of flavin-dependent photoreceptors and confer many biological light reactions in plants, microbes and animals. Here, a highly variable C-terminus is crucially involved in signaling³⁴⁻³⁶. However, the molecular mechanism of chromophore sensing and signal transduction is still not clear for most of the cryptochromes. In the animal-like cryptochrome from the green alga *Chlamydomonas reinhardtii*, *CraCRY*, previous studies have demonstrated that three tryptophans and a tyrosine residue (Y373) act as electron transfer chain, where Y373 forms an unusually stable radical state after photoreduction¹⁰⁹⁻¹¹¹. In addition, a model was proposed that the Y373[•] radical affects the α 22 helix conformation and suggests structural movement from the fully oxidized to the hydroquinone state based on the HDX data¹¹². For these reasons, one major aim of my PhD thesis was to unravel the mechanism of chromophore sensing and signal transduction structurally in *CraCRY* by using time-resolved serial femtosecond crystallography. To obtain more information about the residues, which are involved in photoreduction, I generated a series of *CraCRY* mutants to compare their structures and spectroscopic properties between their oxidized and semiquinone state, to gain a whole picture of the system.

Besides, *CraCRY* is not only a cryptochrome, but also exerts a (6-4) photolyase function,^{111, 113}. Currently, the repair mechanism of (6-4)PP is still an open issue. To provide a structure-based answer to this topic, a second aim of my thesis was to establish conditions for *CraCRY*-DNA co-crystals, which are suitable for TR-SFX. I also performed *in crystallo* cryo-trapping method to characterize the intermediates structures for post-illumination. We expect that TR-SFX experiments at X-ray free electron lasers will further elucidate the precise reaction, finally settling the long-standing controversy of (6-4) photolyase mode of action.

3. Materials and Methods

3.1 Cloning and site-directed mutagenesis

The *CraCRY*-WT plasmid was based on the pET28a vector as previously published¹¹¹. *CraCRY* mutants were generated by site-directed mutagenesis (QuikChange Lightning Site-Directed Mutagenesis Kit, Agilent). First, the forward primer was designed containing the desired mutation (Appendix 1) and its complementary sequence as the reverse primer. The WT plasmid was used as a template mixing with the reaction buffers and mutated nucleotides were amplified by the PCR (Appendix 2). Then 1 µl of the *Dpn* I restriction enzyme was added directly to each amplification reaction and incubated at 37 °C for 5 min to digest the parental supercoiled dsDNA. Two µl of the *Dpn* I-treated DNA were transformed into the DH5α competent cells.

3.2 Transformation

DH5α competent cells were put on ice to thaw cells, and 1 µl plasmid (~100ng) was added into cells. The cells were placed on ice for 10 min and followed by heat-shocked for 45 seconds at 42 °C. Then the cells were put back on ice for 2 min. One ml LB medium was added to let the cells recover at 37 °C for 1 hr. After recovery, the cells were spread on LB plates which containing kanamycin and incubated for 16 hours at 37°C.

3.3 Protein expression and purification

Escherichia coli BL21(DE3) was transformed with a pET-28a-based construct containing the *CraCRY* gene. An *E. coli* colony was picked up to grow in 50ml LB medium with kanamycin by using 200 ml flasks for 16 hours at 37 °C. Then 500 ml 2YT medium (Appendix 3) was incubated with 5 ml of overnight cell cultures by using 2000 ml flasks at 37 °C (Eppendorf, New Brunswick Innova 44R). Upon an OD₆₀₀ of 0.4, temperature was lowered to 18 °C and the culture was grown until OD₆₀₀ of 0.6. Five µl isopropyl β-d-1-thiogalactopyranoside (IPTG, 1 M stock) was added with final concentration of 10 µM and incubated 20 to 24 hours at 18 °C. The cells were centrifuged at 6000 rpm (Beckman Coulter, JA 8.1) for 30 min under 4 °C. Cell pellets were re-suspended in loading buffer and a tip of a spatula of lyophilized DNase I and lysozyme crystals were added. In addition, 50 µl 0.2 M PMSF was given directly before starting the cell lysis. Cell disruption was performed with a high pressure homogenizer (EmulsiFlex-C3, Avestin). A second centrifugation step cleared the cell lysate from debris by using 20000 rpm (Beckman Coulter, JA 25.5) for 1 hour, with the supernatant being loaded onto a self-packed 10 mL nickel-NTA (Roche) column which was pre-equilibrated with loading buffer. After protein binding to the nickel-NTA matrix, 5 column volumes (CV) of loading buffer and wash buffer were needed to remove

unbound proteins. After elution via addition of 250 mM imidazole to the loading buffer, afterwards an heparin affinity chromatography (HiTrap 5ml Heparin HP, GE Healthcare) step was carried out to remove DNA contaminants by buffer A and to elute the proteins by buffer B at high salt concentration. Finally, protein monodispersity was ensured via size exclusion chromatography (Superdex 200 material, GE Healthcare) using gel filtration buffer as running buffer. All relevant purification buffer components are described in Appendix 4.

3.4 *CraCRY* and its mutants: Protein crystallization

The crystallization of *CraCRY* followed previously conditions¹¹¹. The *CraCRY* protein was concentrated to 3mg/ml (Amicon, 30K) and sterile-filtered before crystallization. The protein concentration measurement was based on the Bradford method (Bio-Rad) using the 595 nm absorption (DU-800 spectrophotometer, Beckman coulter). Then the *CraCRY* protein was incubated overnight in the dark at 4°C. During crystallization, the environment required safety light to prevent light-induced reaction of *CraCRY*. Based on the micro-seeding method (Hampton Research), *CraCRY* crystals were grown in 0.1 M 2-(N-morpholino)ethanesulfonic acid (MES), pH 5.6 and 35% (w/v) PEG 4000 at 4 °C, to obtain crystal's sizes suitable for TR-SFX experiments. One ml crystals seeding tube was prepared in advance. First, 10 µl crystal sample was pipetted from stock solution, and added to 990 µl of crystallization mix (1:1 protein solution: crystallization solution). Afterwards, the crystals have to be crashed by vortex for 3 to 5 minutes and stopping for 30 second every 30 second. Finally, the vial was wrapped with aluminum foil for at least 8h until the crystals appear. The crystallization of *CraCRY* mutants followed the same method as the WT condition. Furthermore, different percentage and types of PEG can produce different sizes of crystals and are described in Appendix 5.

3.5 6-4 DNA synthesis and hybridization

The single-stranded photodamaged 6-4 DNA with sequence d(5'-AGCGGT<>TGCCGTG-3') was synthesized in-house by Prof. Dr. Junpei Yamamoto (Osaka university, Japan). The non-photodamaged DNA strand with sequence d(5'-CACGGCA<>ACCGCTCG-3') was ordered in large quantities from Genomics Ltd, Taipei, Taiwan. Both strands were solubilized in gel filtration buffer, and then mixed at an equal molar ratio (0.4 mM final concentration). Finally, they were hybridized in a thermocycler (Biometa, T3000) by first heating the solution to 95 °C and then slowly decreasing the temperature to 25 °C over a period of 3 hours.

3.6 *CraCRY*-DNA co-crystallization

Preparations of the *CraCRY* protein and DNA were generated as described above. The first *CraCRY*-DNA co-crystal was published by Franz, S. *et al.* in 2018 (PDB: 6FN0)¹¹¹. However, this co-crystallization condition was difficult to reproduce due to the unusual interlock of overhangs from the DNA duplexes between each symmetry crystal unit (Appendix 6A). Accordingly, altered DNA sequences (Appendix 7) were introduced and screened by crystallization robotics (Phoenix, Art Robbins Instruments). Initial co-crystal diffraction data were collected in Taiwan Photon Source 05A micro-crystallography beamline (National Synchrotron Radiation Research Center in Hsinchu), which gave a resolution of up to 1.8Å (Appendix 6B). Unfortunately, these *CraCRY*-DNA co-crystals were too big and few to perform TR-SFX experiments (Appendix 8A).

In order to obtain small and generically plentiful crystals, the streak seeding method was carried out¹¹⁴. During crystallization procedure, the environment required strict safety light to prevent (6-4)PP DNA repair by *CraCRY*. Here, a 10 mg/ml *CraCRY* solution was mixed in a 1:1 ratio with 0.2 mM Overhang-1 DNA. This mixture was incubated with crystallization buffer (0.1 M MES PH 6.0, 20% (w/v) PEG8000) at a 1:1 ratio so that the final concentrations of protein and DNA were 2.5 mg/ml and 50 µM, respectively. Twenty µL aliquots of the crystallization mix were pipetted in 24-well ultra-clear u-bottom microplates (Hampton Research). Afterwards, a streak seeding fiber was quickly wiped through already-grown crystals and dragged through new drops containing fresh crystallization solution. Finally, microplate was wrapped with aluminum foil for at least three to five days at 22 °C until co-crystals appeared (Appendix 8B).

3.7 Steady-state UV/Vis spectroscopy and photoreduction assay

Absorption spectra of *CraCRY* variants were recorded using a DU-800 spectrophotometer (Beckman coulter). The protein solutions were measured in buffer containing 20 mM Tris pH 8.5, 200 mM NaCl. In order to obtain the fully oxidized cofactor, all proteins were aliquoted and covered in darkness for at least 12 hours at 4°C before first spectra was recorded. For *in vitro* photoreduction, spectra were measured after 5 minutes by using a Leica KL300 microscope light source and a royal blue LED (450 nm, Cree) at a distance of 10 cm and 4 °C.

3.8 Degassing and obtaining fully reduce state of *CraCRY* crystals under anaerobic conditions

In order to prevent re-oxidation, all required buffers were degassed and put into anaerobic chamber (COY) to incubate at least 24 hours. The crystals aliquot and 77 mg

of aliquoted powdered DTT were first degassed for at least one hour by loading them into the airlock of the anaerobic chamber in an open container. To avoid sample overheating, both samples were kept at all times in pre-chilled Lab-Armor beads (ThermoFisher Scientific). Water ice was never used to avoid oxygen contamination derived from melting. Afterwards, subjected into airlock for seven cycles of evacuation and nitrogen flushing, followed by storage at 68 K mbar for one hour. Finally, the airlock was evacuated and flushed with working gas mix (96% N₂, 4% H₂) twice, after which both samples were loaded into the anaerobic chamber. Once inside the anaerobic chamber, the crystals were transferred into a Lab-Armor bead-filled dry bath at 4 °C. To get fully reduced of *CraCRY*, first, the aliquoted powdered DTT was mixed with 1 mL of gel filtration buffer to produce a fresh 0.5 M DTT solution. Then 2.7 ml crystals were taken to mix with 300 µl DTT solution, so that the final concentration of DTT was 50 mM. Afterwards, laid down the crystals and DTT mixture as flat as possible on the Lab-Armor bead-filled dry bath at 4 °C. Finally, the light source and a royal blue LED were adjusted so as to cover the entirety of tube, which was then illuminated for 30 minutes to induce fully reduce state.

3.9 *CraCRY* crystals filtration and crashing

For TR-SFX experiments, huge amounts of crystals were needed and had to be prepared few weeks in advance. During the period of storage, some crystals became big enough to block injector nozzles. In order to get smooth injection flows during TR-SFX experiments, crystals' filtration and crashing can solve the problem as following. Here, crystals were pre-concentrated 10X by centrifugation (Eppendorf, Minispin) at 3600 g for 5 minutes, followed by loading the crystal suspension to 50 µm sorting filter (pluriSelect). The bigger crystals stuck on the filter membrane, then washed by pipetting supernatant on the membrane gently. Afterwards, centrifuged again by 3600 g for 5 minutes to obtain filtrated and 10X concentrated crystals, then transferred into 1.5 ml tube. To prevent losing samples, one crashing run of maximum material volume was 500 µl. Finally, the stick of homogenizer inserted into the bottom of tube and push the button of the homogenizer firmly to crash crystals for 40 seconds twice. To avoid heating, the suspension was put into pre-chilled Lab-Armor beads for 40 seconds after the first crashing step. The crashed crystals are shown in Appendix 9.

3.10 *CraCRY* crystals embedding and injector building

The crashed crystal suspension was harvested by centrifugation at 3600 g for 15 minutes until crystals had been compacted completely to pellets. Supernatant was discarded as much as possible and crystal slurry was embedded in a 1:9 ratio with a hydrophobic grease matrix as described in previous research¹⁰⁵. Briefly, 270 µl grease

matrix was mixed with about 30 μL of crystal slurry, followed by a tip of spatula inserted to the bottom of tube and rotated until the mixture was homogenized. Then $\sim 300\text{ }\mu\text{L}$ of embedded crystalline material was spooned out to a cover glass slide and mixed well again. Afterwards, embedded material was transferred to a $\phi 4\text{ mm}$ cartridge by flat spatula and the Teflon cylinder was inserted on the top of cartridge with parafilm. Then spin cartridges were spun at 3000 g (6600 rpm) for 5 minutes with the Teflon cylinder pointing downwards to ensure the sample was compacted at the bottom. Finally, the injector was assembled with cartridge, O-ring and 75 μm nozzle, and carrying the whole injector body in opacity to protect it from light during transport to the hutch.

3.11 Data acquisition and on-site data processing at SACLA

The experiments took place at the SACLA BL2 beamline inside the DAPHNIS system¹¹⁵. It mainly consists of the helium chamber, injectors and a multi-port charge-coupled device detector (MPCCD)^{98, 116} with a 50 mm sample-to-detector distance for data collection. Inside the DAPHNIS system, the helium gas was controlled at least beyond 98% to prevent *in situ* oxidation and the temperature was adjusted at 20 $^{\circ}\text{C}$ by a water circulation device to avoid heating before sample flow started. For *CraCRY* experiments, a 75 μm nozzle was used with a flow rate of 2.6 $\mu\text{L}/\text{min}$ (for TR-SFX experiments) or 1 $\mu\text{L}/\text{min}$ (for SFX experiments). Images were obtained using a 10 keV X-ray beam with 30 Hz pulse frequency and a pulse duration of $< 10\text{ fs}$ and beam diameter of 1.5 μm . For triggering the photoreduction event, a 3-nanosecond pulse from a 408 nm OPO pump laser, which operated with 10 Hz and 50 μJ , was connected to the DAPHNIS system to point directly to excite crystals. Depending on the experiment, the delay times, before the XFEL hits the crystals, were varied between 10 ns and 300 μs . Furthermore, for millisecond region of delay time, the pump laser frequency was changed to 3 Hz, resulting in datasets between 33 ms and 233 ms.

In order to compare the difference between light illuminated datasets and dark datasets, the high-quality dark-adapted datasets without pump laser have been collected with at least 50000 indexed images. Next, in order to avoid light contamination, time-resolved data collection was performed at 10 Hz and collected two dark images for every light image (meaning light, dark 1 and dark 2). After collecting about 5000~6000 images, on-site structure and difference map generation showed that the dark 2 data were devoid of light-contamination free, while dark 1 was only minimally contaminated. Afterwards, data collection was performed at 10 Hz until at least 25000 indexed images had been obtained.

For on-site data processing at SACLA, the Cheetah pipeline¹¹⁷ was used to analyze all images in real-time and identify the hits from light and dark images. After a run for collecting data was finished, the offline pipeline started automatic spot finding and

indexing, followed by converting the hit images into HDF5 files and pass the information to the *CrystFEL* software¹¹⁸⁻¹¹⁹. The *CrystFEL* program suite produced then preliminary datasets to assess data quality, light contamination, initial detector geometry optimization, etc.

3.12 Off-site data processing and data extrapolation

Initial datasets obtained on site were further analyzed by optimization of detector geometry using *CrystFEL*¹¹⁸⁻¹¹⁹. All datasets were merged via *process_hkl*, followed by conversion to a file in MTZ format, which can be dealt with in the CCP4 suite¹²⁰. However, upon light illumination by pump laser, only a part of the molecules in the crystal lattice are activated. Therefore, in order to determine structures of reaction intermediates with low occupancy, the experimental structure factors (F_o) have to be deconvoluted by an extrapolation method^{73, 121}. After careful structural refinement of the high-quality dark datasets, the *SFALL* software of the CCP4 suite¹²⁰ was used for generation of a set of calculated structure factors ($F_{c_{dark}}$) and calculated phases ($PHI_{c_{dark}}$) for the dark structure. Afterwards, both dark observed structure factors ($F_{o_{dark}}$) and the time-resolved structure factors of interest for time X (F_{o_X}) were scaled against $F_{c_{dark}}$ via the *SCALEIT*¹²² tool in the CCP4 suite. Next, Bayesian and occupancy-weighted normalized difference structure factors ($dF_{o_{WN}}$) were calculated by following equations 1 and 2, which were then added to $F_{c_{dark}}$ to produce extrapolated structure factor (F_{ext}) (eq. 3). The occupancy parameter (N) was obtained from equation 4 by extrapolation at multiple N values until an inflexion point was found in the cumulative negative density of a particular region of interest, which in this case was Asn395 of *CraCRY*.

$$dF_{o_{WN}} = \frac{N * W * (F_{o_X} - F_{o_{dark}})}{n} \quad \text{eq. 1}$$

$dF_{o_{WN}}$: Normalized, Bayesian and occupancy weighted difference structure factor.

N: Occupancy weight parameter (eq. 4)

W: Bayesian weighting term (eq. 2)

n: average Bayesian weighting term for all structure factors of the dataset.

F_{o_X} : Observed structure factor for time X.

$F_{o_{dark}}$: Observed structure factor of dark dataset.

$$W = \frac{1}{1 + \frac{(F_{o_X} - F_{o_{dark}})^2}{(\overline{F_{o_X} - F_{o_{dark}}})^2 + \Delta\sigma^2}} \quad \text{eq. 2}$$

W: Bayesian weighting term.

F_{o_X} : Observed structure factor for time X.

$F_{o_{dark}}$: Observed structure factor for dark dataset.

$\Delta\sigma$: Difference standard deviation.

$\overline{F_{o_X} - F_{o_{dark}}}$: Average of the structure factor difference over the entire dataset.

$\Delta\sigma$: Average standard deviation over the entire dataset.

$$F_{ext} = dF_{o_{WN}} + F_{c_{dark}} \quad \text{eq. 3}$$

F_{ext}: extrapolated structure factor.

dF_{o_{WN}}: Normalized, Bayesian and occupancy weighted difference structure factor.

F_{c_{dark}}: Calculated dark structure factor.

$$\text{occupancy (\%)} = \frac{200}{N} \quad \text{eq. 4}$$

N: Occupancy weight parameter

3.13 Structural refinement

All dataset were solved via molecular replacement by Phaser¹²⁰, using the published *CraCRY* structure (6FN2)¹¹¹ for the TR-SFX experiment and the *CraCRY*-DNA structure (6FN0)¹¹¹ for 6-4 DNA repair experiments as start models. The dataset of initial refinement was always the corresponding dark dataset, which resulting in a basal model for the excited datasets. After molecular replacement by Phaser, rigid body refinement and restrained refinement was done with Refmac5 of the CCP4 suite and Coot¹²³. Data collection, processing and refinement details can be found in Tables 1-5.

3.14 Generating difference density maps

Determining the differences between similar structures allows several ways. One common procedure is to refine their models individually and superimposing and comparing the finally refined models. However, larger movements between models can still be artifactual, particularly in regions which are not well ordered or are present in multiple conformations. Isomorphous difference density maps (dFo) were calculated and used from experimental data directly in the comparisons¹²⁴. The dFo was generated via the phenix tool, and always scaled against datasets by using the *SCALEIT* tool¹²² in CCP4i software¹²⁰. To generate a difference map, a high quality structure for the basal (=dark) state C_X was first fully refined. Then, the observed structure factors (Fo) of the basal state E_{X/Y} were subtracted from those of a different state C_Y, resulting in difference structure factors. Afterwards, difference structure factors were phased via the high quality C_X structure, producing a dFo_(X-Y). Resolution limits here were always set to the worse of the two datasets for high resolution, while to 10 Å for low resolution. For the purpose of comparing the movements of several time-scales in C_{light}, all SACLA time-resolved datasets were scaled to C_{dark}.

3.15 Data processing for *KAMO*

KAMO is a program for automated processing and merging of microcrystal diffraction data¹²⁵. The diffraction images were indexed individually by *XDS*¹²⁶, followed by a check for cell compatibility and determination of the space group. If indexing was performed without any prior knowledge, then integration is performed with triclinic P1 symmetry. Afterwards, all target data were selected by using the checkboxes and click “Multi merge strategy” button to group with the same lattice. Then, via *BLEND*, which performs hierarchically cluster analysis by unit-cell parameters on several datasets, the most isomorphous datasets were merged. Only clusters with high completeness (>90%) were subjected to merging. Next, clusters were merged via *XSCALE*¹²⁶. For each cluster, datasets belonging to a cluster are subjected to merging with outlier rejections. *XSCALE* is used for merging and outliers are detected by analyzing the *XSCALE* output¹²⁵. Finally, a statistics report is automatically generated, when merging is finished, and further structure refinement was done. Data processing and refinement statistics are presented in Tables 4 and 5.

3.16 Unit cell analysis for *CraCRY* mutants

In order to investigate the *CraCRY* C-terminal unfolding in the semiquinone state, the related amino acids were generated by mutagenesis (see above), and all mutants of diffraction data were collected from a large number of microcrystals to obtain complete datasets in both oxidized and semiquinone states at the beamline BL32XU, SPring-8, Sayo, Japan. Upon photoreduction to the semiquinone state, crystals underwent compression, as indicated by pronounced shortening of the *c*-axis (Appendix 10). Therefore, the mutants of dataset were divided into two group via the length of *c*-axis which were either short (145 Å to 151 Å) or long (151 Å to 155 Å). Detailed statistics and B-factor distributions of the structures are described in the Results section.

3.17 Time-resolved *in crystallo* optical spectroscopy (TR-*icOS*)

In order to obtain more information about the protonation event after transition from the oxidized to the semiquinone state in *CraCRY*, UV/Vis spectra were collected to complement the TR-SFX structures. Therefore, time resolved *in crystallo* UV/Vis absorption spectroscopy was performed at the ID29S-*icOS* Laboratory, ESRF, Grenoble, France¹²⁷. First, 2 µl of crystals slurry were mounted between two layers of COC (100 µm each) to obtain a sandwich-like setup via using a double sticky tape (60 µm thick) (SwissCI - LCP kit) as the entire sample holder (Appendix 11). In addition, the sample holder setup was assembled under safety red light to prevent light excitation. Next, the laser pump signal used a 355 nm laser (Surelite EX) to generate pulses of 3 to 5 ns duration with a fixed 10 Hz repetition rate. The optical parametric oscillator

(OPO) box (Horizon) converted the 355 nm laser light into a 450 nm laser light with around 20 μ J per pulse to activate the photoreduction reaction of *CraCRY*. Next, the probe signal was used Xenon flash lamp (L11316-11, Hamamatsu) to provide 2 μ s white light pulses and obtained the spectrum data by connecting an optical fiber to the dual-channel spectrophotometer (Avantes). Finally, the CITY module which was developed at the ESRF allows to control the time delay between the laser pump to the probe signal from microsecond to a couple of hundred milliseconds. Additionally, oxidized crystals were also prepared as a control. The experiments were in cooperation with Dr. Sylvain Engilberge, ESRF.

3.18 Cryo-trapping setup

In order to investigate (6-4)PP repair by *CraCRY*, a simple cryo-trapping setup was performed in Taiwan Photon Source 07A (Appendix 12A). Briefly, *CraCRY*-DNA co-crystals (see above) were pre-concentrated for 10X by centrifugation at 8000 rpm for 5 minutes. Next, 4 μ l of crystal suspension which had been mixed with reducing agent was loaded into a single sample holder of loop (SWISSMXCM-SPINE), and dry the extra solution from the backside of loop by using filter paper. Afterwards, the crystals were illuminated with 405 nm of 5 mW laser pointer (MT OPTICS) in a 10 cm distance to activate the repair reaction. After illumination for a certain period of time, the crystals were flash-frozen in liquid nitrogen and mounted on the beamline for data acquisition. Each structure was refined against a corresponding “superdataset”, which was the result of merging roughly 400 individual small angle subdatasets each derived from one individual crystal via *KAMO*¹²⁵ (Appendix 12B). Data processing and refinement statistics are presented in Table 6.

4. Results and discussion

4.1 *CraCRY* signal transduction via time-resolved structural analysis

4.1.1. Photoreduction overview in *CraCRY*

In contrast to other cryptochromes, *CraCRY* absorbs not only blue but also red light when being in the semiquinone state.^{110, 128} *CraCRY* forms efficiently this semiquinone state (FADH^\bullet) under blue light illumination and stabilizes it sufficiently for life times of seconds to several minutes^{109, 128}. According to this feature, Y373 plays an important role that is located at the distal end of the tryptophan triad (W399, W376, and W322 in *CraCRY*) and acts as a final electron donor of the extended electron-transfer chain¹¹⁰. As other PCSf members, *CraCRY* photoreduction stalls out after photoreduction round 1 in the absence of an external reducing agent (Figure 12), because the Y373^\bullet radical needs to be reduced in order to act as an electron donor in photoreduction round 2. Further, the status of Y373 strongly depends on the environment of pH value¹⁰⁹. Especially in acidic environment, the short-lived $\text{FAD}^\bullet/\text{Y373}^{*\bullet}$ RP can be stabilized within microseconds via proton transfer towards FAD^\bullet to delay radical pair recombination, resulting in its semiquinone FADH^\bullet state. Notably, $\text{Y373}^{*\bullet}$ deprotonates in less than one nanosecond by proton-coupled electron transfer (PCET), whereas FAD^\bullet protonation requires several microseconds, excluding the possibility of direct proton transfer within the RP.

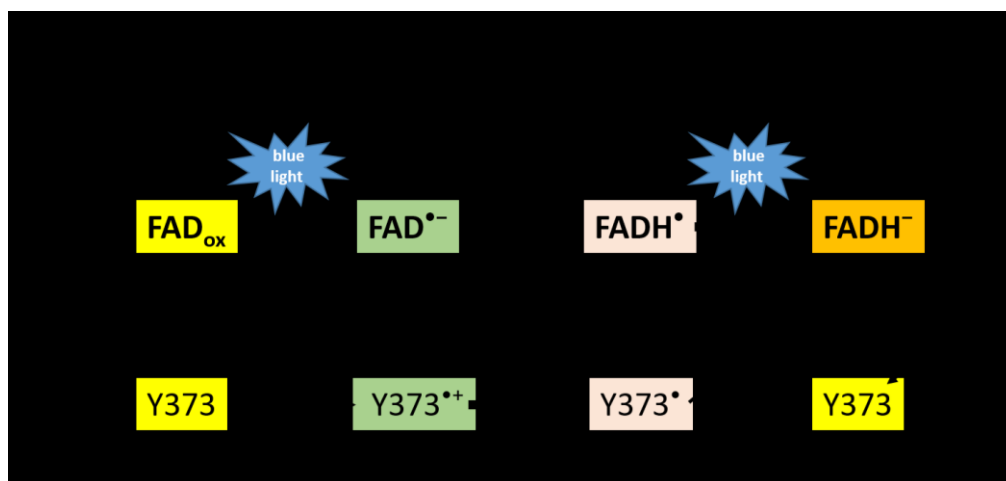


Figure 12. Schematic scheme of photoreduction in *CraCRY*. In the first round of photoreduction, via blue light excitation, dark-adapted of non-RP $\text{FAD}_{\text{ox}}/\text{Y373}$ (yellow background) abstracts an electron from Y373 by the Trp triad with concomitant deprotonation of $\text{Y373}^{*\bullet}$ by PCET to form the short-lived RP $\text{FAD}^\bullet/\text{Y373}^\bullet$ (green and pink background, bottom). $\text{FAD}^\bullet/\text{Y373}^\bullet$ converts then into signal state, which is long-lived RP $\text{FADH}^\bullet/\text{Y373}^\bullet$ (pink background). The second round of photoreduction will lead to the catalytically active state of FADH^- (orange background) for DNA repairing. In addition, all reactions presented here can be reversible by reoxidation. In this work, we are focus on the three steady states (dark-adapted state, signaling state, and catalytically active state) and decrypting the time-resolved transition in short-lived RP $\text{FAD}^\bullet/\text{Y373}^{*\bullet}$ to signal state long-lived RP $\text{FADH}^\bullet/\text{Y373}^\bullet$.

4.1.2. Structure changes between *CraCRY*'s dark-adapted, signaling and catalytic states

Overall structures of the three different redox states of *CraCRY* are shown in Figure 13. To obtain the dark-adapted FAD_{ox} state structure (C_{ox}), crystals had to be measured in darkness. For the semiquinone state, blue-light illuminated crystals were generated directly before data collection to allow us enrichment of the FADH[•]/Y373[•] RP and obtain a static, steady state structure of *CraCRY*'s signaling state (C_{signal}). Finally, by providing both light and a reducing agent under anaerobic conditions, we were able to generate crystals in the fully reduced FADH[•] state, which yielded *CraCRY*'s catalytically active structure (C_{cat}). SFX data statistics of C_{ox} , C_{signal} and C_{cat} are shown in Table 1.

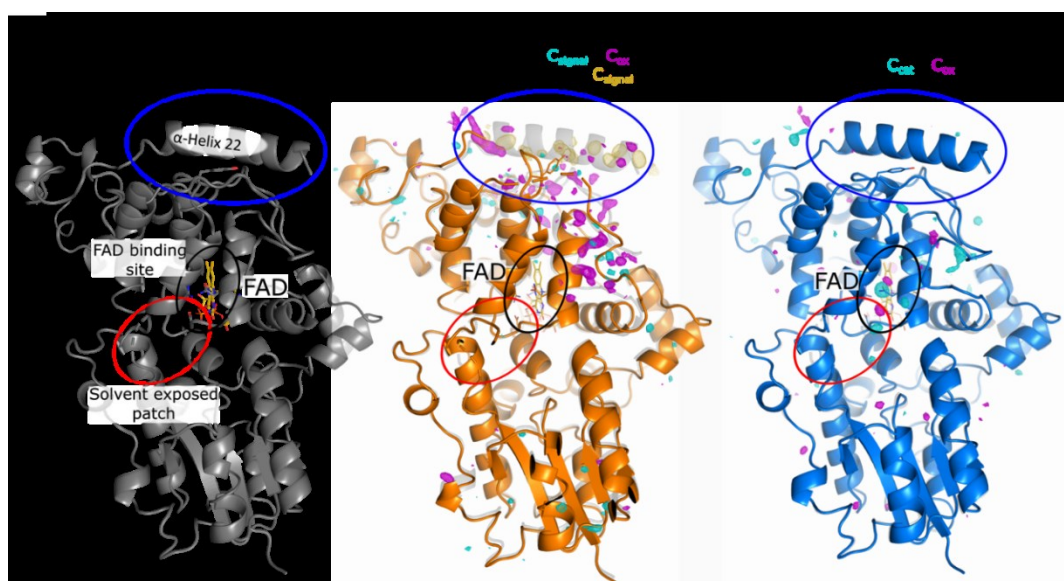


Figure 13. Overall structure of *CraCRY* in its three redox states. The dark-adapted and oxidized state (C_{ox}) is shown in grey, while the signaling, semiquinone (C_{signal}) and the catalytic, fully reduced (C_{cat}) states are depicted in orange and blue, respectively. Further, the FAD chromophore is shown as a stick model in yellow. To highlight the changes between states, C_{ox} is shown in the background behind C_{signal} and C_{cat} , while 3.5 σ contoured difference maps are overlaid in cyan for positive peaks, and magenta for negative ones. The disappearance of α -helix 22 in C_{signal} is illustrated by a 1.5 σ -contoured 2DFo-mFc omit map of the region as shown in gold. Finally, three regions of interest are highlighted with colored ellipsoids, namely the C-terminal region (blue), the FAD binding site (black) and the solvent exposed patch (red).

In both C_{ox} and C_{cat} structures, which were generated by SFX (Figure 13), *CraCRY* shares the highly conserved two-domain topology of other PCSf members, and both were largely identical to the previously published *CraCRY* synchrotron structure¹¹¹. For all three redox states, the FAD chromophore is held in a U-shaped conformation, with a single solvent facing channel in C_{ox} and C_{cat} which acts as the catalytic site for DNA repair. Unlike FAD, Y373 is near the protein's C-terminus, covered by the C-terminal α -helix 22. However, C_{signal} showed tremendously structural changes when comparing

C_{ox} and C_{cat} . In C_{signal} , neither α -helix 22, nor the other Y373 neighboring elements could be observed, with strong negative difference density signals appearing in the region (Figure 13). Further, upon blue light illumination, the c -axis of C_{signal} was shortened by about 3 Å (Table 1, Appendix 10), and the model of C-terminal region was mostly impossible to be determined due to its unfolding, that even the FAD and DNA binding site were strongly affected. Accordingly, we propose that C_{signal} may have no, or strongly reduced, DNA binding affinity. In the close-up view of the C-terminal region of C_{signal} , Y373 had become fully solvent exposed, with the phenolic hydroxyl group interacting with a crown-wise arrangement of three crystallographic waters (Figure 14).

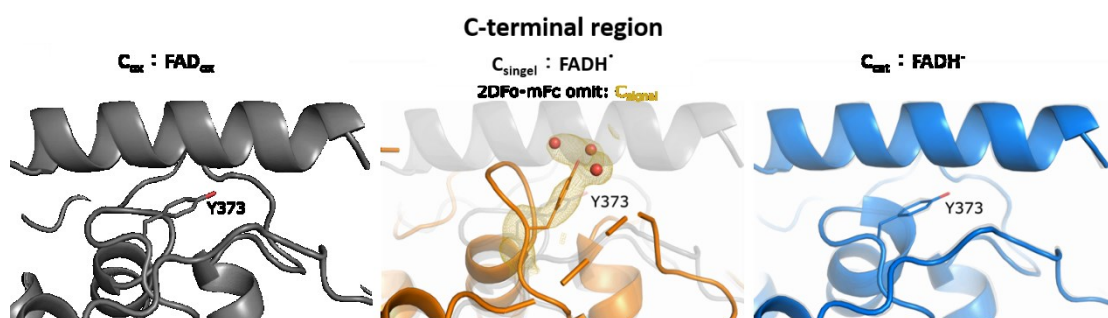


Figure 14. Detail of the C-terminal in each CraCRY state. In C_{signal} , 1.5σ-contoured 2DFo-mFc omit map highlighting the conformational change undergone by Y373, and its tight interaction with three crystallographic water molecules.

In addition, compared to previously published studies describing the photoreduction of a class II photolyase⁷³ (*Mm*CPDII), the local effects around the FAD binding site were relatively minor. The results indicated that the N395 Oδ1 atom approached the FAD N5 nitrogen position in both C_{signal} and C_{cat} (Figure 15), which has been shown to both stabilize and promote the formation of the neutral $FADH^{\bullet}$ state, while also stabilizing the catalytically active $FADH^{\bullet}$ ⁷³. Meanwhile, R360 approached the the FAD's isoalloxazine moiety in both C_{signal} and C_{cat} , apparently to electrostatically stabilize the radical and anionic flavin species, respectively (Figure 15).

Our three redox state structures demonstrated how each individual CraCRY state accomplishes its function. In the dark-adapted state of C_{ox} , the C-terminal region is tightly bound to the protein body and therefore unable to interact with downstream proteins^{34, 36}. In the C_{signal} state, the C-terminal region has become flexible by being mostly unfolded, providing large interaction surfaces at the former docking site of the α -helix 22 and possibly a reduced DNA binding capacity. Finally, in the C_{cat} state, full reduction required the action of an external reducing agent for converting Y373[•] to Y373. Accordingly, the unfolded C-terminus of C_{signal} is refolded to the generic conformation found in the structures of other PCSf members and provides a fully reduced $FADH^{\bullet}$, which is ready for light-driven DNA repair¹¹¹.

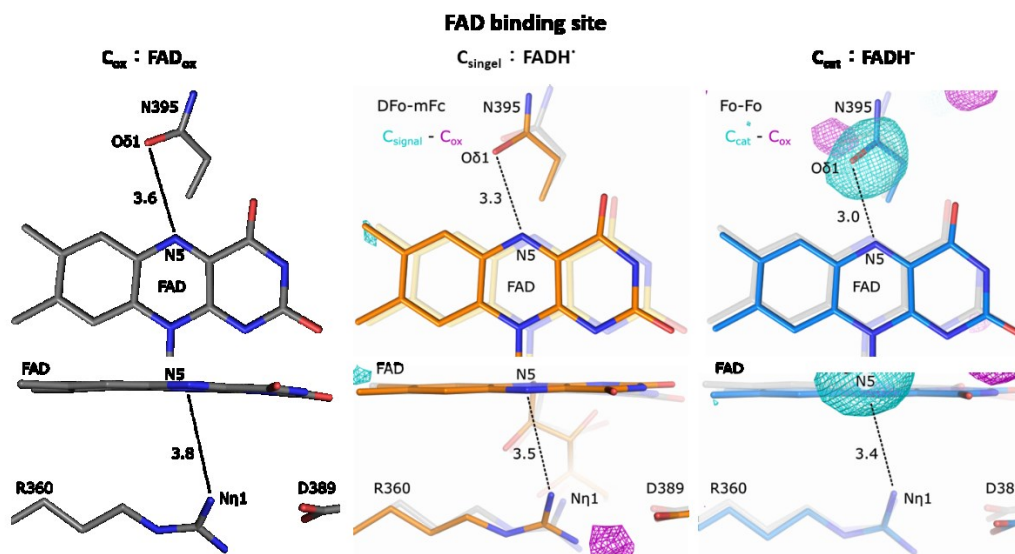


Figure 15. Detail of the FAD binding site. Local changes with FAD isoalloxazine's main interaction partners, i.e. N395 and R360. Structures are shown with 3.5σ contoured difference density maps for C_{signal} and C_{cat} . Cyan is used for positive peaks, magenta for negative peaks.

Table 1. SFX data statistics for steady-state structures. Numbers in parenthesis describe the highest resolution shell.

| Steady-state | Oxidized (FAD _{ox}) | Semiquinone (FADH [•]) | Reduced (FADH ⁻) |
|---------------------------|-------------------------------|----------------------------------|------------------------------|
| Space group | $P2_12_12_1$ | | |
| Unit cell (a, b, c)* | 50.32, 64.92, 151.54 | 50.59, 65.98, 148.72 | 50.32, 64.92, 151.54 |
| Processing statistics | | | |
| Completeness (%) | 99.98 (100) | 99.89 (100) | 99.94 (100) |
| Unique reflections | 34440 (1660) | 34552 (1688) | 34439 (1660) |
| Multiplicity | 245 (44.3) | 405 (70) | 307 (52) |
| CC1/2 | 0.9978 (0.551) | 0.9981 (0.5348) | 0.9949 (0.4831) |
| I/ σ | 8.446 (1.53) | 6.911 (1.58) | 9.119 (1.39) |
| Refinement statistics | | | |
| Resolution range (Å) | 41.95-2.05 (2.123-2.05) | 32.21-2.55 (2.641-2.55) | 31.25-2.1 (2.175-2.1) |
| Unique reflections | 31990 (3124) | 16875 (1636) | 29745 (2884) |
| R-work | 0.1618 (0.241) | 0.2478 (0.4024) | 0.1675 (0.3687) |
| R-free | 0.1948 (0.274) | 0.2841 (0.4464) | 0.1911 (0.3886) |
| Ramachandran outliers (%) | 0 | 0.66 | 0 |
| RMS (bonds, Å) | 0.013 | 0.002 | 0.002 |
| RMS (angles, deg) | 1.7 | 0.53 | 0.45 |
| Average B factor | 55.17 | 33.73 | 35.98 |

* $\alpha=\beta=\gamma=90^\circ$

4.1.3 Overall features of the C_{ox} to C_{signal} transition

The C_{ox} and C_{signal} static structures provided start- and end-points of the cryptochrome photoreduction reaction. Accordingly, the light-driven ET events for a detailed view in between were solved by TR-SFX. Our TR-SFX experiments were performed in SACLA BL2 beamline with a 3-nanosecond laser pulse to trigger photoreduction. Notably, the intramolecular electron transfer, i.e. the transition from oxidized FAD to radical, anionic $FAD^{\bullet-}$, is a sub-nanosecond process¹⁰⁹. Thus, it is not possible to resolve ultrafast movements below ~ 10 nanoseconds with our setup. The estimation of their lifetime after illumination is given based on data provided in reference¹⁰⁹. To do so, dark adapted, oxidized *CraCRY* crystals underwent TR-SFX experiments at delay times between 10 ns to 233 ms, resulting in a total of 19 time-resolved structural snapshot and one control dark structure (Table 2 and Table 3). In the following, time resolved structures will be denoted as C_X , with X corresponding to the time delay applied to it. Furthermore, difference electron density maps¹²⁴ were constructed to highlight structural differences, which are designated as the difference between to states, e.g. $C_X - C_X$.

When comparing any of the time resolved C_X structures and their respective difference electron density maps to the control dark structure C_{dark} (equivalent to C_{ox}), the differences were found in three main regions, namely the FAD binding site, the proteins' C-terminal region, and a solvent exposed patch adjacent to the FAD pocket (Figure 13). From our entire set of time-resolved datasets, three main changes could be observed. First, rapid changes (10 to 100 ns) could be observed mostly in the FAD binding site and D321, a residue within the C-terminal region (Figure 18A and 18C), which allows us to analyze the fast movement triggered by the short-lived $FAD^{\bullet-}/Y373^{\bullet}$ RP. Next, intermediate changes (100 ns to 100 μ s) localized in the FAD binding site and the solvent exposed patch (Figure 18A and 18B) which we could observe the process of proton transfer occurring for Y373. Finally, slow changes (100 μ s to 233 ms) were mostly focused around the C-terminal region, and specifically on and around α -helix-22 (Figure 18C). A detail of primary properties of all *CraCRY* TR-SFX structures was described in Appendix 13.

Clearly, previous spectroscopic data describing the initial ET and Y373 deprotonation as sub-nanosecond reaction¹⁰⁹, our time-resolved structural snapshots paint a picture in which ET between Y373 and FAD triggers early conformational changes in their vicinity, which are then propagated towards distant protein regions, where slower events take place. In the following sections, each of these regions will be analyzed in detail to explain their role in *CraCRY* signal transduction via C-terminal unfolding.

Table 2. TR-SFX data statistics for structures (ns to μ s). Numbers in parenthesis describe the highest resolution shell.

| Time point | C _{dark} | C _{10ns} | C _{30ns} | C _{100ns} | C _{300ns} | C _{1μs} | C _{3μs} | C _{10μs} | C _{30μs} | C _{100μs} | C _{300μs} |
|----------------------------|---|------------------------|---------------------------|---------------------------|-------------------------|---------------------------|---------------------------|---------------------------|--------------------------|--------------------------|--------------------------|
| Space group | P2 ₁ 2 ₁ 2 ₁ | | | | | | | | | | |
| Unit cell (a, b, c)* | 50.84, 65.6, 153.13 | | | | | | | | | | |
| Data collection statistics | | | | | | | | | | | |
| Total crystals | 121535 | 33539 | 39142 | 33889 | 37691 | 35914 | 35442 | 29832 | 31941 | 35612 | 31312 |
| Indexed crystals | 87112 | 24694 | 29537 | 25703 | 29189 | 26164 | 25574 | 21803 | 23375 | 26457 | 23565 |
| Indexing rate (%) | 71.7 | 73.6 | 75.5 | 75.8 | 77.4 | 72.9 | 72.2 | 73.1 | 73.2 | 74.3 | 75.3 |
| Resolution range | 33.06-1.64 | 32.8-1.75 | 32.8-1.81 | 33.06-1.87 | 33.1-1.83 | 32.07-1.83 | 32,8-1.77 | 32.8-1.85 | 33.06-1.78 | 32.81-1.78 | 32.8-1.8 |
| Merging statistics | | | | | | | | | | | |
| Completeness (%) | 99.98 (100) | 99.95 (100) | 99.93 (100) | 99.94 (100) | 99.95 (100) | 99.95 (100) | 99.95 (100) | 99.94 (100) | 99.95 (100) | 99.94 (100) | 99.94 (100) |
| Unique reflections | 63708 (3083) | 52639 (2596) | 47627 (2301) | 43294 (2113) | 46189 (2258) | 43294 (2113) | 50888 (2489) | 44700 (2229) | 50056 (2478) | 50127 (2482) | 48440 (2388) |
| Multiplicity | 909 (110) | 332 (53) | 427 (74) | 306 (64) | 374 (81) | 275 (59) | 328 (62) | 225 (62) | 326 (69) | 266 (59) | 320 (84) |
| CC1/2 | 0.997 (0.506) | 0.991 (0.5299) | 0.994 (0.527) | 0.993 (0.515) | 0.993 (0.515) | 0.991 (0.515) | 0.99 (0.522) | 0.987 (0.522) | 0.99 (0.536) | 0.988 (0.52) | 0.987 (0.536) |
| I/σ | 9.505 (1.37) | 6.496 (1.33) | 7.65 (1.43) | 7.08 (1.43) | 7.133 (1.38) | 6.76 (1.42) | 6.42 (1.41) | 5.99 (1.51) | 5.91 (1.38) | 6.07 (1.41) | 5.98 (1.37) |
| Refinement statistics | | | | | | | | | | | |
| Resolution range (Å) | 33.09-1.64 (1.699-1.64) | 30.1-1.9 (1.97-1.9) | 27.75-1.95 (2.02-1.95) | 30.15-1.95 (2.02-1.95) | 30.15-1.9 (1.97-1.9) | 30.15-1.95 (2.02-1.95) | 30.15-1.85 (1.91-1.85) | 27.75-1.95 (2.02-1.95) | 30.15-1.9 (1.968-1.9) | 27.75-1.9 (1.968-1.9) | 27.75-1.9 (1.968-1.9) |
| Unique reflections | 63625 (6235) | 41237 (4051) | 38203 (3781) | 38204 (3782) | 41238 (4051) | 38208 (3782) | 44619 (4403) | 38204 (3781) | 41237 (4051) | 41233 (4050) | 41235 (4050) |
| R-work | 0.1364 (0.239) | 0.1691 (0.308) | 0.207 (0.385) | 0.199 (0.352) | 0.188 (0.395) | 0.1944 (0.363) | 0.1805 (0.412) | 0.173 (0.374) | 0.167 (0.389) | 0.1575 (0.38) | 0.172 (0.382) |
| R-free | 0.1693 (0.295) | 0.211 (0.36) | 0.244 (0.395) | 0.236 (0.384) | 0.231 (0.412) | 0.2347 (0.386) | 0.2137 (0.482) | 0.2102 (0.429) | 0.2055 (0.413) | 0.1954 (0.468) | 0.2112 (0.41) |
| Ramachandran outliers | 0 | 0 | 0 | 0.41 | 0 | 0 | 0.41 | 0.41 | 0.21 | 0.21 | 0.21 |
| RMS (bonds, Å) | 0.0013 | 0.009 | 0.005 | 0.006 | 0.004 | 0.003 | 0.007 | 0.013 | 0.013 | 0.009 | 0.004 |
| RMS (angles, deg) | 1.67 | 0.97 | 0.73 | 0.81 | 0.7 | 0.6 | 0.92 | 1.32 | 1.27 | 1.03 | 0.63 |
| Average B factor | 30.76 | 17.36 | 20.79 | 19.83 | 22.72 | 26.76 | 21.65 | 20.58 | 22.67 | 22.79 | 22.94 |

* $\alpha=\beta=\gamma=90^\circ$

Table 3. TR-SFX data statistics for structures (ms). Numbers in parenthesis describe the highest resolution shell.

| Time point | C1ms | C7ms | C33ms | C66ms | C100ms | C133ms | C166ms | C200ms | C233ms |
|----------------------------|---|--------------------------|----------------------------|--------------------------|----------------------------|--------------------------|--------------------------|--------------------------|---------------------------|
| Space group | <i>P2₁2₁2₁</i> | | | | | | | | |
| Unit cell (a, b, c)* | 50.84,65.58,153.34 | 50.84,65.58,153.34 | 50.84,65.6,153.13 | 50.84,65.6,153.13 | 50.74,65.45,152.95 | 50.74,65.45,152.95 | 50.74,65.45,152.95 | 50.74,65.45,152.95 | 50.74,65.45,152.95 |
| Data collection statistics | | | | | | | | | |
| Total crystals | 31540 | 30271 | 20035 | 25681 | 82202 | 82198 | 81336 | 81148 | 81293 |
| Indexed crystals | 23978 | 22889 | 13360 | 17595 | 58107 | 58431 | 57634 | 57730 | 57729 |
| Indexing rate (%) | 76 | 75.6 | 66.9 | 68.5 | 70.7 | 71.1 | 70.9 | 71.1 | 71 |
| Resolution range | 35.59-1.85 | 35.59-1.82 | 33.16-1.73 | 33.1-1.7 | 33.02-1.8 | 33.02-1.8 | 33.02-1.8 | 33.02-1.85 | 33.02-1.8 |
| Merging statistics | | | | | | | | | |
| Completeness (%) | 99.92 (100) | 99.92 (100) | 99.95 (100) | 99.88 (100) | 99.81 (100) | 99.79 (100) | 99.79 (100) | 99.81 (100) | 99.8 (100) |
| Unique reflections | 44753 (2237) | 46926 (2280) | 54688 (2683) | 57384 (2825) | 48171 (2347) | 48171 (2347) | 48171 (2347) | 44448 (2205) | 48171 (2347) |
| Multiplicity | 377 (65) | 378 (66) | 314 (55) | 328 (79) | 1174 (107) | 1175 (110) | 1231 (179) | 1313 (200) | 1138 (94) |
| CC1/2 | 0.992 (0.52) | 6.65 (1.33) | 0.988 (0.537) | 0.988 (0.52) | 0.999 (0.548) | 0.999 (0.565) | 0.999 (0.504) | 0.999 (0.553) | 0.999 (0.503) |
| I/σ | 6.65 (1.33) | 6.53 (1.36) | 6.04 (1.4) | 5.8 (1.23) | 8.78 (1.31) | 8.84 (1.33) | 8.69 (1.28) | 9.31 (1.39) | 8.71 (1.27) |
| Refinement statistics | | | | | | | | | |
| Resolution range (Å) | 30.61-1.9 (1.968-1.9) | 31.59-2.0 (2.071-2.0) | 30.15-1.85 (1.916-1.85) | 31.59-2.3 (2.382-2.3) | 31.52-2.15 (2.227-2.15) | 30.54-2.2 (2.279-2.2) | 30.54-2.2 (2.279-2.2) | 30.54-2.2 (2.279-2.2) | 30.54-2.25 (2.33-2.25) |
| Unique reflections | 41264 (4052) | 35479 (3490) | 44620 (4403) | 23515 (2300) | 28484 (2812) | 26601 (2616) | 26601 (2616) | 26608 (2616) | 24911 (2453) |
| R-work | 0.1661 (0.4133) | 0.2149 (0.433) | 0.1638 (0.411) | 0.2234 (0.4245) | 0.2159 (0.3944) | 0.2133 (0.384) | 0.2163 (0.387) | 0.2267 (0.392) | 0.2269 (0.405) |
| R-free | 0.206 (0.4668) | 0.2491 (0.447) | 0.192 (0.42) | 0.2767 (0.4405) | 0.2531 (0.4551) | 0.256 (0.388) | 0.2483 (0.398) | 0.2531 (0.4137) | 0.2701 (0.4242) |
| Ramachandran outliers | 0.21 | 0.21 | 0.21 | 1.04 | 0 | 0 | 0 | 0 | 0 |
| RMS (bonds, Å) | 0.012 | 0.003 | 0.0013 | 0.013 | 0.002 | 0.002 | 0.002 | 0.002 | 0.002 |
| RMS (angles, deg) | 1.11 | 0.55 | 1.26 | 1.71 | 0.51 | 0.49 | 0.5 | 0.47 | 0.53 |
| Average B factor | 27.45 | 26.88 | 24.5 | 38.68 | 23.41 | 23.18 | 23.19 | 20.99 | 26.55 |

*α=β=γ=90°

4.1.4 Changes in the isoalloxazine geometry

Based on our previous research⁷³, when electrons are transferred onto the isoalloxazine moiety, subtle changes of the FAD chromophore could be observed upon photoreduction. Thus, the dihedral angle of ρ_C and ρ_N can describe the geometry of the FAD isoalloxazine moiety⁷³ (Section 1.4). Besides, from the structural view of the FAD binding site, the significant positive and negative density peaks around the isoalloxazine (Figure 18A) indicate that we can expect significant changes there. During FAD_{ox} to FADH^* transition, ρ_C values changed from 10 ns and reached a maximum at 10 μs , whereas ρ_N values followed the same pattern but the highest peak was 100 μs , suggesting a twisted geometry (Figure 16). After that, both ρ_C and ρ_N decreased and returned to their initial values over a few hundred milliseconds. The result shows a similar pattern for the isoalloxazine moiety as the class II photolyase *MmCPDII*⁷³ but milder changes, as the maximum differences between ρ_C and ρ_N were about 10° and 30° in *CraCRY* and *MmCPDII*, respectively. Accordingly, we assume that the kinetics of the FAD state transitions differ after photoreduction between cryptochromes and photolyases.

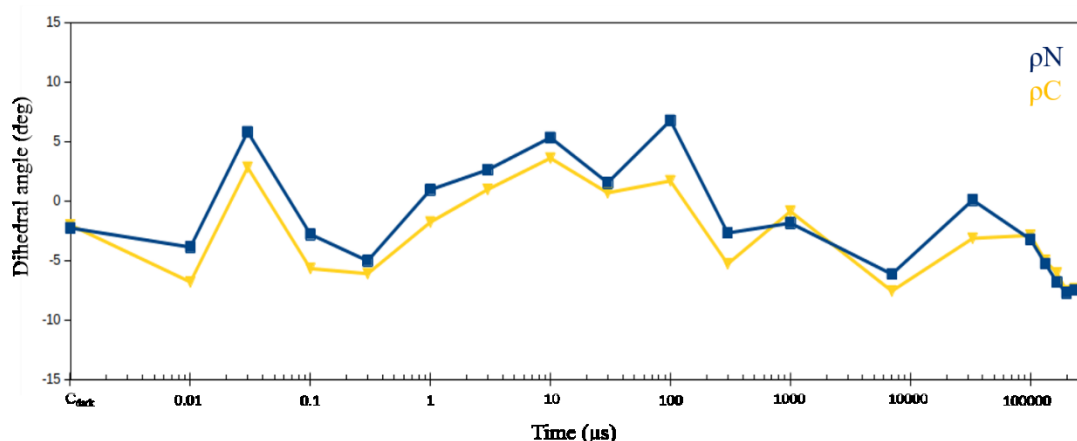


Figure 16. Pattern of isoalloxazine geometry. Evolution of ρ_C (yellow) and ρ_N (blue) dihedral angles over time for photoreduction.

4.1.5. Extrapolation and occupancies of time-solved datasets

As mentioned above in section 3.12, in order to detect low occupancies of active state structures upon light illumination, an extrapolation method was used that finds the intersection between the occupancy parameter (N) value and the corresponding cumulative negative density of interested region; the intersection point corresponds to the optimal occupancy parameter. First, regions of interested were selected via the clear structural changes in time-resolved datasets, which were H309, R360, E384, N395 and the end of C-terminal region (RMAAAYRRSK), to extrapolate multiple N values. The results showed that N395 maintained the highest occupancy (20-25%) in most of the time compared to other amino acids in terms of their occupancy distribution (Figure

17). Therefore, the time-resolved datasets were extrapolated based on the N395 occupancy for structure determination; detailed extrapolation plots are shown in Appendix 14. To obtain better extrapolation plots for long time delays, we noted that the calculated multiple N values differed by a factor up to three from the initial intersectional N value based on N395 (Appendix 14). Accordingly, in good agreement with the onset of C-terminal unfolding in the milliseconds range (Figure 18C), it was better to base extrapolate onto the C-terminal region in the time range exceeding 133 milliseconds (Appendix 14). On the other hand, the occupancy distribution indicated that no matter what kind of amino acid extrapolation was used, the overall occupancy decreased in the many milliseconds time range and strongly suggested that this occurs due to C terminal unfolding.

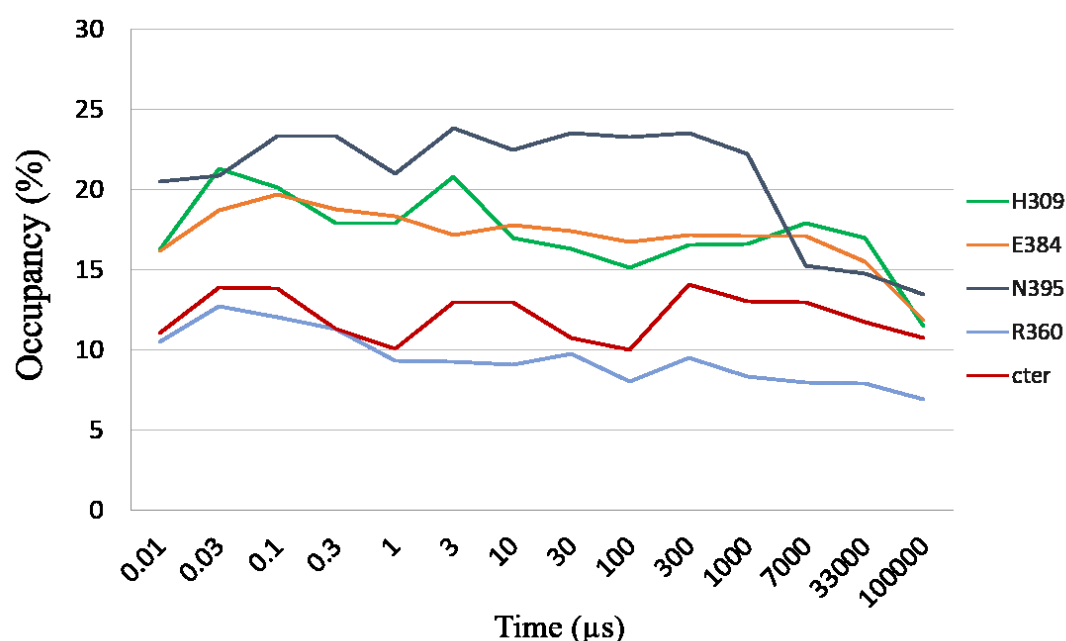


Figure 17. Occupancy distribution via multiple amino acids extrapolation. The occupancy parameter of N value was found and calculated by equation (section 3.12). The green, orange, black, blue and red color were represented H309, E384, N395, R360 and C-terminal region extrapolation, respectively, in each time point.

4.1.6. Observation of early events (10 to 100 ns)

In *CraCRY*, previous spectroscopic study has shown that the intramolecular electron transfer was sub-nanosecond¹⁰⁹. Thus, in our fastest time-point, i.e. 10 ns, both FAD and Y373 can be expected to exist in their RP form. In good agreement, in C_{10ns} the FAD isalloxazine moiety presented an already somewhat twisted geometry (ρ_C and ρ_N of -3.9° and -6.8° , compared to C_{dark} values of -2.2° and -2° , respectively), which is characteristic of the $FAD^{\bullet-}$ state⁷³. Meanwhile, N395 had rotated counterclockwise by ~ 10 degrees, which resulted in the N395 side-chain O δ 1 atom moving away from the FAD N5 atom (Figure 18A, plot). Here, we had observed a similar behavior during

photoreduction of a class II photolyase⁷³, and had suggested that repulsion occurred between the electronegative carbonyl and $\text{FAD}^{\bullet-}$. Besides, R360 appeared to approach the isoalloxazine moiety by 0.4 Å, thereby partially neutralizing the anionic radical, which was analogous to previous observations with a class II photolyase⁷³.

Although incompatible with an N395O δ 1- $\text{FAD}^{\bullet-}$ interaction, as the $\text{FAD}^{\bullet-}$ N5 cannot act as a hydrogen bond donor, the movement of N395 in $\text{C}_{10\text{ns}}$ was positioning the amide nitrogen closer to the $\text{FAD}^{\bullet-}$ N5. Under these condition, N395 may help to stabilize $\text{FAD}^{\bullet-}$ in the early event. Surprisingly, and unlike previous structural descriptions of the photoreduction process⁷³, within the next 100 ns, N395 rotation had been reversed. From $\text{C}_{100\text{ns}}$, and as supported by strong difference signals (Figure 18A), the N395 sidechain rotated clockwise by 85°, with O δ 1 approaching the isoalloxazine N5 atom to within 2.9 Å, and remained in this orientation for the remainder of the time-course (Figure 18A and Appendix 15). The results suggested that N395 was ready towards to stabilize neutral radical FADH^{\bullet} in the next microsecond and millisecond range. The detailed structural changes upon protonation will be described in the following section. Although we could not observe any Y373 conformational changes (Figure 18C), even for $\text{C}_{10\text{ns}}$ structure, a significant pair of negative/positive difference density peaks had accumulated around D321 (Figure 18C). The resulting structure showed a clear shift of D321 away from Y373. Meanwhile, D321's main interaction partner, R492 on α -helix 22 (α 22), also moved away from D321, as evidenced by a rapid accumulation of negative difference density around α 22 between C_{dark} and $\text{C}_{30\text{ns}}$ in the early time range (Figure 18C, plot). Recent transient-spectroscopy data¹⁰⁹ showed that the neutral Y373 $^{\bullet}$ radical is formed in a single step by PCET, i.e. concomitant transfer of an electron and proton, with a sub-ns time-constant, resulting in the extraordinarily long-lived Y373 $^{\bullet}$ radical. At this time, it had been proposed that D321 may be the most likely proton acceptor of Y373 in the reaction as it forms a hydrogen bond with Y373. Here, our data strongly supports this interpretation, as the now neutralized D321 can only very weakly interact with R492, causing the former salt bridge to break and relocate both residue sidechains to their new positions. Within the next 100 ns, D321 moves even further away from both Y373 and R492, with its position remaining essentially fixed from $\text{C}_{100\text{ns}}$ to $\text{C}_{233\text{ms}}$.

4.1.7 Observation of intermediate and late events (100 ns to 233 ms)

In our previous research on *Mm*CPDII photoreduction, we suggested a highly conserved arginine as a transient proton source during $\text{FAD}^{\bullet-}$ to FADH^{\bullet} conversion that is equivalent to R360 in *Cra*CRY⁷³. In *Cra*CRY, this may still be the case, as in the 100 ns to 1 μ s time-frame, strong difference signals accumulate in the immediate environment of R360 (Appendix 16). However, and unlike to the scenario presented by

the class II photolyase *Mm*CPDII, these changes appear to be transient, with signals in the immediate environment of R360 decaying from 3 μ s (Appendix 17), and the side-chain maintaining essentially the same orientation for the rest of the time-course. Here, analysis of the R360 difference signals indicated that the transient species had a much lower occupancy (about 10%) than the corresponding signals in the N395 environment (Figure. 17), indicating a rapid kinetic exchange between the major R360 conformation.

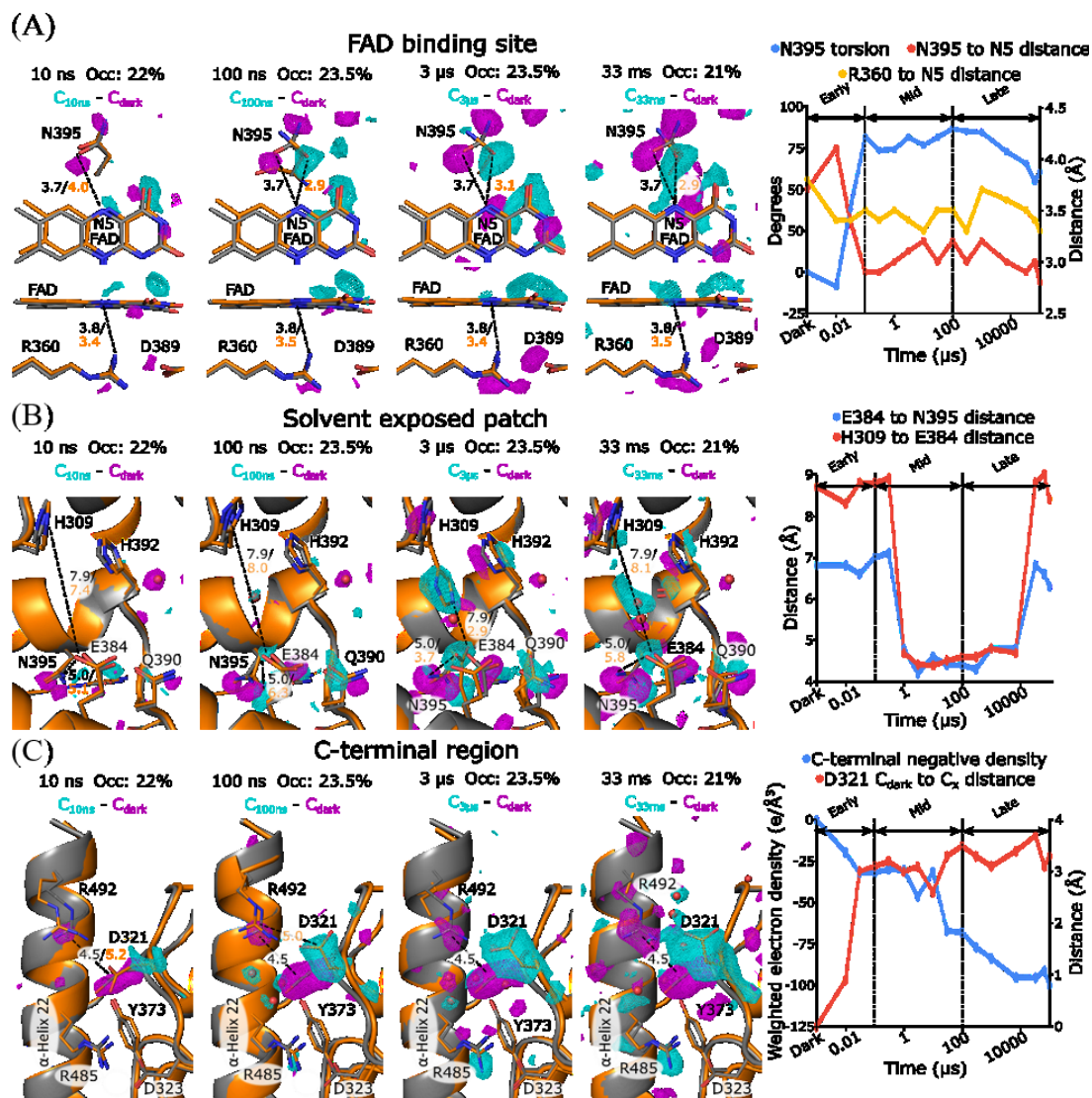


Figure 18. Highlights of the CraCRY C_{dark} to C_{signal} transition. TR-SFX structural snapshots of CraCRY (C_x , orange) are shown in comparison to C_{dark} (grey). To highlight the experimental significance of the observed differences, 3.5 σ contoured isomorphous difference electron densities are shown in cyan for positive peaks and magenta for negative ones. On the right of each panel, a time-course of relevant reaction coordinates is plotted, based on the data obtained from the refined structures. (A) The FAD binding site is shown from two different perspectives to highlight the changes in N395 and R360 geometry. The plot follows torsion of the N395 side-chain amide group (blue), as well as the N395 O δ 1 to FAD N5 distance (red) and R360 N η 1 to FAD N5 distance (yellow). (B) Changes in the solvent exposed patch, as shown in Figure 13.

The plot here follows the center of mass distances between E384 and N395 (blue) and H309 and E384 (red). (C) Changes in the C-terminal region. In this case, the occupancy weighted total negative electron density of the C_x - C_{dark} map region within 2.5 Å of the $\alpha 22$ backbone, representing the degree of delocalization of $\alpha 22$ over time is plotted in blue. Additionally, the distance between the center of mass of the D321 side-chain in C_{dark} versus C_x is also shown in red.

To figure out the events surrounding solvent exposure patch area, the entirety of the time-course is described in Appendix 18. In the $C_{100\text{ns}}$ state, difference signals started to accumulate near E384 and Q390 within the solvent exposed patch (Figure 18B). By $C_{1\mu\text{s}}$, these signals had become so strong that they resulted in significant conformational changes for both amino acids (Appendix 18), with the E384 side-chain rotating towards the FAD binding, and Q390 following suit in order to maintain E384's hydrogen bonding network. As a result, the distance between E384 and N395 was reduced by 3.7 Å, bringing the carboxylate of E384 closer to the FAD binding site (Figure 18B). Within the same time frame, although accumulating somewhat more slowly, difference density peaks also started to appear for the solvent exposed patch residues H309 and H392 (Figure 18B and Appendix 18). Accordingly, while by $C_{3\mu\text{s}}$ H392 suffered a subtle shift towards Q390, H309 dramatically rotates along the χ_1 torsion by $\sim 145^\circ$, bringing it in direct contact with E384 (Figure 18B). Clearly, this sequence of events suggests a coordination between early N395 and R360 movements within the FAD binding site (Figure 18A and Appendix 15) and intermediate E384 and H309 changes within the solvent exposed patch (Figure 18B and Appendix 18). Interestingly, while conformational changes in the FAD itself, as well as N395 and R360 in its binding site are irreversible within our 10 ns to 100 ms time frame (Figure 18A, plot), residues in the solvent exposed patch return to their original conformations within 33 ms (Figure 18B, plot).

Here, we suggest that the function of the solvent exposed patch is relevant as a transient protonation pathway during protonation of $\text{FAD}^{\bullet-}$. Accordingly, after proton transfer has taken place, the residues in this region are regenerated by return to their original positions, independently of the FAD's redox and protonation state. Thus, our data strongly points towards a proton transfer chain composed of R360, E384, and H309, which supplies the $\text{FAD}^{\bullet-}$ radical with solvent protons. Indeed, since in the $\text{FAD}^{\bullet-}$ to FADH^{\bullet} transition the flavin N5 atom is protonated, N395 O δ 1 then becomes its main interaction partner, significantly stabilizing the neutral radical, and even possibly driving the protonation reaction¹²⁹. Such an interaction can be observed in C_{signal} and C_{cat} , where the O δ 1-N5 distance permits hydrogen bonding between the two elements (Figure 15). Sequentially, N395 directly interacts with E384, meanwhile E384 forms a hydrogen bond with H309 in the same microsecond time frames. Finally, while protonation has occurred in the millisecond range, the relevant residues of the transient

protonation pathway (TPP) returned to their initial position, resulting in radical semiquinone flavin. In summary, photoreduction derived changes in the immediate vicinity of FAD and in the TPP respond to the changing electrostatics around the radical semiquinone FAD. Similar to our finding in previous studies regarding the *Mm*CPDII photolyase, early events in the FAD binding site mostly aim to stabilize the flavin, providing it with enough time to accept a proton before competing recombination with Y373[•] can take place. Meanwhile, the function of the TPP appears to be unique to animal cryptochromes, explaining how rapid protonation of the anionic semiquinone state can take place in this PCSf class.

Likewise, the entirety of the time-course for C-terminal conformational changes is described in Appendix 19. The early movements of D321 and R492 left a cavity between $\alpha 22$ and the main protein body, i.e. the C-terminal domain, which was filled in the subsequent 100 μ s by several water molecules (Figure 18C). Accordingly, nearby salt bridges were weakened, with R492 becoming so delocalized by C_{3 μ s}, that its side-chain could not be fully modeled (Fig. 3c). Further delocalization of R492 could be easily followed by the second accumulation step of negative electron density near $\alpha 22$ between C_{3 μ s} and C_{100 μ s} in the mid-range of the time course (Figure 18C, plot). Meanwhile, significant difference peaks appeared around R485 and D323, which act as a second, more N-terminally located equivalent of the R492-D321 salt bridge (Figure 18C, Appendix 19). Furthermore, following from C_{3 μ s} atomic model, R485 had moved away from D323, further weakening the $\alpha 22$ interaction with the rest of the C-terminal domain.

Following the intermediate events involving the R492-D321 and R485-D323 pairs, starting from C_{3 μ s} onward, a third step of negative difference electron density accumulation occurred around $\alpha 22$ (Figure 18C, plot). However, unlike the previous two steps, which could be directly attributed to the delocalization of R492, in this case the difference density was diffuse, occurring along the whole helix (Appendix 20), and indicating that the entirety of the helix was becoming more flexible. Furthermore, C-terminal residues started to delocalize so strongly that their side-chains could not be modeled even though the resolution of the corresponding datasets was comparable to earlier time-points (Appendix 13). By C_{7ms}, residue K494 had become completely delocalized and could not be modeled, demonstrating that $\alpha 22$ was gradually unravelling in a C- to N-terminal direction (Appendix 21). Finally, the side chain of R485 delocalized dramatically so that its position was occupied by three water molecules. Meanwhile D323 had rotated by 104° and the salt bridges were weakened between D323 and R485, resulting in the entire $\alpha 22$ helix receding away (Appendix 22). In conclusion, a clear sequence of events emerges from these data, where synchronous electron and proton transfer from Y373 drives a rapid weakening of the C-terminal salt-

bridge, which permits water to enter the $\alpha 22$ -protein interface, in turn extending the electron transfer and proton transfer derived effects towards more N-terminal portions, and finally causing $\alpha 22$ to ‘peel away’ from the main protein body in a C- to N-terminal direction, ultimately leading to the partially unfolded C_{signal} state.

4.1.8 E384 involves in proton transfer chain

In order to further confirm that E384 is participated in proton transfer, the single mutant E384Q was generated and measured in terms of the amount of FADH^\bullet formation upon light illumination. Accordingly, a previous study has reported that proton transfer to FAD^\bullet is highly pH-dependent¹⁰⁹. Indeed, E384Q had deleterious effects on photoreduction and impeding the formation of FADH^\bullet (Figure 19). Here, the UV/Vis spectrum was taken after 5 minutes of light illumination. To calculate the percentage of FADH^\bullet , the absorption of oxidized FAD (450 nm) and semiquinone FADH^\bullet (630 nm) were used via following equation. The increased FADH^\bullet concentration was calculated via difference of 630 nm absorption between light and non-light illumination, and divide by extinction coefficient of 630 nm (equation 5). Next, the concentration of non-light-illuminated FAD was obtained by equation 6. Finally, the percentage of FADH^\bullet accumulation was obtained by equation 7.

$$\Delta[\text{FADH}^\bullet] = \frac{\Delta A_{630}}{\epsilon_{630}} \quad \text{eq. 5}$$

$[\text{FADH}^\bullet]$: The increasing amount of FADH^\bullet concentration

A_{630} : Absorption of 630 nm.

ϵ_{630} : Extinction coefficient of 630 nm

$$[\text{FAD}_{\text{ox}}] = \frac{A_{450}}{\epsilon_{450}} \quad \text{eq. 6}$$

$[\text{FAD}_{\text{ox}}]$: The concentration of oxidized FAD in non-light illumination.

A_{450} : Absorption of 450 nm in non-light illumination.

ϵ_{450} : Extinction coefficient of 450 nm

$$\Delta(\%) = \frac{\Delta[\text{FADH}^\bullet]}{[\text{FAD}_{\text{ox}}]} \times 100\% \quad \text{eq. 7}$$

$\Delta\%$: percentage of FADH^\bullet accumulation.

The result indicated that *CraCRY* WT had accumulated very few FADH^\bullet in the high pH environment upon light illumination, whereas the FADH^\bullet level increased rapidly by lowering the pH value. However, in the E384Q mutant, the amount of FADH^\bullet was strongly hampered even at low pH, i.e. pH 6. Here, we strongly suggest that E384 is involved as part of the TPP in proton transfer to FAD^\bullet to form FADH^\bullet . The entire spectra are shown in Appendix 23.

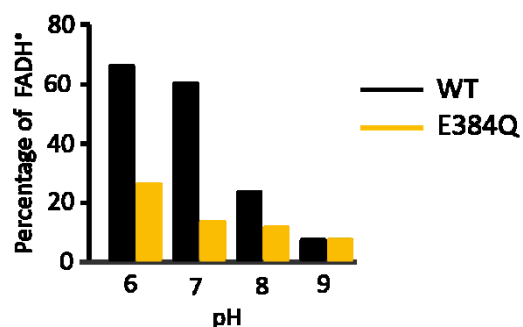


Figure 19. Calculating FADH* accumulation from UV/Vis spectroscopy in solution. The bar in color black and orange represent WT and E384Q respectively.

4.1.9 Time resolved *in crystallo* optical spectroscopy of CraCRY crystals

In order to ensure that our procedures yielded the correct redox state, we confirmed our structural data by *in crystallo* UV/Vis spectroscopy. To do this, one had to consider that our microcrystals for TR-SFX were too small to obtain good spectra, and different crystal sizes may affect signal intensity. Thus, as method section 3.4 outlined above, larger crystal sizes were produced via a different crystallization method so that the crystal spectra can be derived (Appendix 24). Encouragingly, in our fastest time point of 10 μ s, the spectrum of FAD^{•-} could be demonstrated and performed the same redox in the entire μ s range (Figure 20, Appendix 25). Further, from our TR-SFX structures suggest that the protonation event has taken place in a couple of milliseconds range, the spectrum of FADH* accumulated can be detectable from 100 ms measurement. Clearly, as our proposed mechanism above, the protonation indeed occurs in millisecond range, especially after 100 ms. The detail TR-*ic*OS measurements were described in Appendix 25, as FAD presents very characteristic, redox dependent spectra.

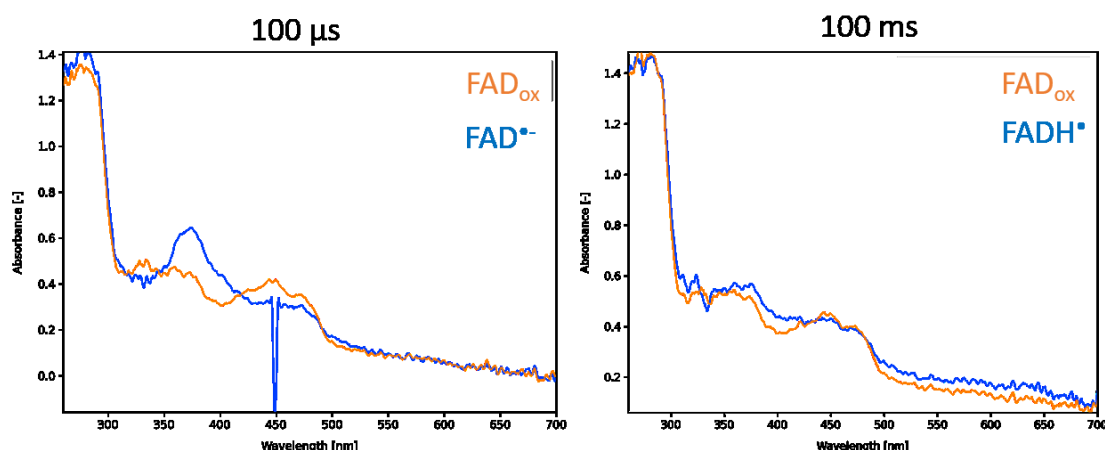


Figure 20. Highlights of the TR-*ic*OS spectrum in 100 μ s and 100ms. The FAD_{ox} spectrum was shown in orange and FAD^{•-} and FADH* were shown in blue respectively. In the 100 μ s measurement, an absorption peak appeared at a wavelength of 360 nm upon light illumination that is characteristic of FAD^{•-}. On the other hand, 630 nm was detected in 100 ms measurement which indicated presence of FADH*.

4.1.10 Unit cell classification of the relevant actors

In order to further understand the role of each of the actors involved in achieving the C_{signal} state, as described above, we generated a series of mutants (Appendix 1), and characterized them in crystallographically under cryo conditions at the BL32XU synchrotron beamline in SPring-8, Japan (Table 4, 5). Here, we took advantage of the fact that, due to $\alpha 22$ helix unfolding in the C_{signal} state, the *CraCRY* wild-type (WT) crystal's unit cell parameters changed upon illumination, particularly the c -axis becoming shorter by ~ 5 Å (Figure 21). Thus, a Gaussian fitting curve was performed in the oxidized state so that the distribution of the c -axis can be observed. Due to a partial shift of the c -axis in the semiquinone state, Gaussian fitting for multiple peaks was calculated by the following formula, and detail described as in Appendix 26 for the relevant actors.

Formula: $y0 + A * \sqrt{2/PI} / w * \exp(-2 * ((x - xc) / w)^2)$

A (area)

xc (center)

w (width)

$y0$ (offset)

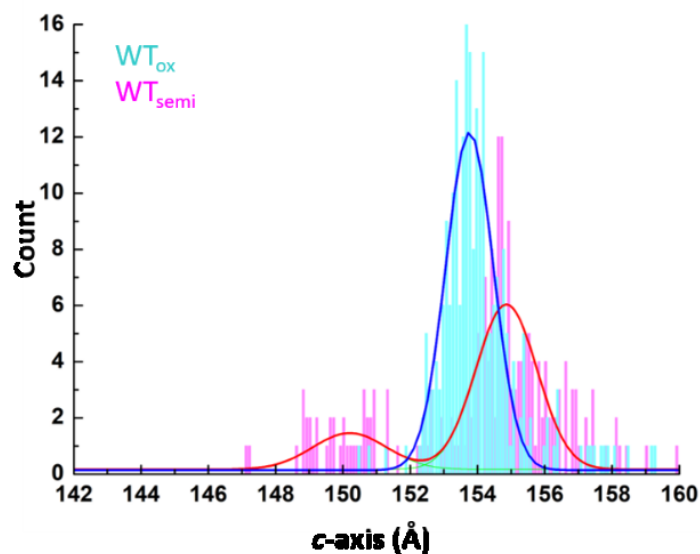


Figure 21. Histogram of c -axis in semiquinone dataset of *CraCRY* WT. The histogram of oxidized and semiquinone were shown in cyan and magenta and Gaussian fitting in blue and red, respectively.

Accordingly, by collecting data from a large number of crystals of each mutant both in the dark and after illumination and sorting them by their c -axis length, we could construct datasets for each state into two groups, the so called long and the short group. The long group contained datasets whose c -axis length varies between 151 to 155 Å,

whereas the short group corresponded to a range of 145 to 151 Å. These will be described as $X_{Y/Z/P}$ with X representing for mutation, Y for long or short c -axis, Z for their state and P for peak number. Finally, the individual classified datasets were processed via *KAMO* software and further refinement statistics is shown in Table 4 and 5.

Table 4. BL32XU data statistics for *CraCRY* mutant structures. Numbers in parenthesis describe the highest resolution shell.

| <i>CraCRY</i> | WT _{Long/Ox} | WT _{Long/Semi} | WT _{Short/Semi} | Y373F _{Long/Ox} | Y373F _{Long/Semi} | D323N _{Long/Ox/P1} | D323N _{Long/Ox/P2} | D323N _{Long/Semi} | D323N _{Short/Semi} |
|-----------------------|---|-------------------------|--------------------------|--------------------------|----------------------------|-----------------------------|-----------------------------|----------------------------|-----------------------------|
| Space group | <i>P</i> 2 ₁ 2 ₁ 2 ₁ | | | | | | | | |
| Unit cell (a, b, c)* | 50.47, 65.49, 153.55 | 50.5, 65.27, 154.54 | 50.59, 65.09, 149.7 | 50.49, 65.6, 153.53 | 50.7, 65.81, 151.98 | 50.66, 65.67, 154.1 | 50.66, 65.56, 154.6 | 50.7, 65.17, 151.12 | 50.74, 65.2, 150.06 |
| Processing statistics | | | | | | | | | |
| Completeness (%) | 99.97 (99.94) | 99.9 (100) | 98.04 (98.43) | 99.98 (99.97) | 99.96 (99.94) | 99.95 (100) | 99.95 (100) | 99.94 (99.96) | 99.83 (99.77) |
| Unique reflections | 35250(3455) | 27070 (2634) | 21446 (2126) | 32852 (3244) | 16679 (1651) | 28747 (2817) | 30900 (3040) | 23004 (2236) | 26723 (2598) |
| Multiplicity | 34 | 17.2 | 8.1 | 76.3 | 55.9 | 51.5 | 83.3 | 72.2 | 85.3 |
| CC1/2 | 0.985 (0.528) | 0.969 (0.509) | 0.957 (0.575) | 0.936 (0.679) | 0.971 (0.517) | 0.915 (0.5) | 0.949 (0.553) | 0.941 (0.58) | 0.958 (0.548) |
| I/σ | 8 (1.08) | 9.47 (2.4) | 4.68 (1.8) | 6.91 (1.5) | 8.18 (1.36) | 5.25 (1.01) | 6.67 (1.15) | 7.64 (1.59) | 8.57 (1.21) |
| Wilson B factor | 14.77 | 21.21 | 26.09 | 9.69 | 1.69 | 13.97 | 15.09 | 20.8 | 15.41 |
| Refinement statistics | | | | | | | | | |
| Resolution range (Å) | 47.95-2.0 (2.07-2.0) | 48.02-2.19 (2.268-2.19) | 49.12-2.33 (2.413-2.33) | 47.96-2.05 (2.123-2.05) | 49.75-2.58 (2.672-2.58) | 48.13-2.15 (2.227-2.15) | 38.65-2.1 (2.175-2.1) | 48.08-2.3 (2.382-2.3) | 48.07-2.18 (2.258-2.18) |
| Unique reflections | 35243 (3453) | 27062 (2634) | 21441 (2126) | 32848 (3243) | 16677 (1651) | 28737 (2818) | 30893 (3040) | 22996 (2235) | 26718 (2599) |
| R-work | 0.1401 (0.1771) | 0.187 (0.243) | 0.1958 (0.256) | 0.1695 (0.2609) | 0.2466 (0.2526) | 0.166 (0.2222) | 0.1646 (0.2474) | 0.1927 (0.2704) | 0.2053 (0.2653) |
| R-free | 0.1872 (0.2418) | 0.2281 (0.2679) | 0.2367 (0.2891) | 0.2162 (0.2688) | 0.2972 (0.2906) | 0.2123 (0.2523) | 0.2137 (0.2898) | 0.2426 (0.3406) | 0.2473 (0.2949) |
| Ramachandran outliers | 0 | 0.8 | 1.1 | 0.5 | 0.5 | 0.5 | 1.25 | 0.27 | 0.22 |
| RMS (bonds, Å) | 0.011 | 0.002 | 0.002 | 0.002 | 0.002 | 0.002 | 0.002 | 0.002 | 0.002 |
| RMS (angles, deg) | 0.95 | 0.56 | 0.56 | 0.54 | 0.53 | 0.53 | 0.57 | 0.55 | 0.56 |
| Average B factor | 17.27 | 31.19 | 33.34 | 13.72 | 16.19 | 19.14 | 18.52 | 26.44 | 21.21 |

*α=β=γ=90°

Table 5. BL32XU data statistics for *CraCRY* mutant structures. Numbers in parenthesis describe the highest resolution shell.

| <i>CraCRY</i> | D321N _{Long/Ox} | D321N _{Short/Semi} | D321ND323N _{Long/ox} | D321ND323N _{Short/Semi} | R485K _{Long/Ox} | R485K _{Long/Semi} | R485K _{Short/Semi} | C482S _{Long/Ox} ^a | C482S _{Short/Semi} ^a |
|-----------------------|--------------------------|-----------------------------|-------------------------------|----------------------------------|--------------------------|----------------------------|-----------------------------|---------------------------------------|--|
| Space group | $P2_12_1$ | | | | | | | | |
| Unit cell (a, b, c)* | 50.49, 65.42, 153.6 | 50.6, 65.07, 150.41 | 50.4, 65.06, 153.46 | 50.45, 64.76, 149.97 | 50.5, 65.73, 153.1 | 50.65, 66.1, 152.29 | 50.28, 65.5, 150.28 | 50.53, 65.9, 154.5 | 50.68, 65, 149.95 |
| Processing statistics | | | | | | | | | |
| Completeness (%) | 99.86 (99.81) | 93.97 (96.08) | 99.94 (99.92) | 99.95 (99.78) | 99.97 (99.86) | 99.97 (99.97) | 99.94 (99.95) | 97.8 (96.3) | 81.1 (81.9) |
| Unique reflections | 21400 (2106) | 9880 (980) | 37642 (3720) | 37235 (3672) | 57003 (5614) | 30683 (3012) | 38153 (3733) | 10692 (1646) | 9886 (1876) |
| Multiplicity | 22.8 | 6.7 | 205.9 | 219.1 | 109.5 | 38.1 | 33.3 | 5.4 | 3.1 |
| CC1/2 | 0.939 (0.5) | 0.981 (0.5) | 0.996 (0.575) | 0.995 (0.575) | 0.993 (0.584) | 0.982 (0.655) | 0.918 (0.606) | 0.974 (0.5) | 0.91 (0.567) |
| I/ σ | 5.74 (1.87) | 9.91 (2.16) | 19.44 (2.27) | 16.44 (1.67) | 11.13 (2.74) | 4.92 (2.46) | 6.52 (2.21) | 4.38 (2.14) | 3.83 (1.34) |
| Wilson B factor | 19.97 | 17.14 | 22.04 | 21.67 | 15.1 | 13.25 | 10.23 | nan | nan |
| Refinement statistics | | | | | | | | | |
| Resolution range (Å) | 47.97-2.37 (2.455-2.37) | 49.21-3.0 (3.107-3.0) | 47.87-1.95 (2.02-1.95) | 41.86-1.94 (2.009-1.94) | 49.87-1.7 (1.761-1.7) | 48.06-2.1 (21.75-2.1) | 49.37-1.93 (1.999-1.93) | - | - |
| Unique reflections | 21319 (2105) | 9851 (980) | 37631 (3717) | 37224 (3662) | 56987 (5606) | 30681 (3013) | 38148 (3732) | - | - |
| R-work | 0.1784 (0.2232) | 0.2196 (0.2824) | 0.1572 (0.2624) | 0.2344 (0.3473) | 0.1491 (0.3446) | 0.1854 (0.249) | 0.1544 (0.2093) | - | - |
| R-free | 0.2175 (0.2454) | 0.2688 (0.3375) | 0.205 (0.2907) | 0.2825 (0.3724) | 0.1828 (0.3782) | 0.2293 (0.3162) | 0.1912 (0.2561) | - | - |
| Ramachandran outliers | 0.25 | 0 | 0 | 0 | 0.5 | 0.77 | 0.51 | - | - |
| RMS (bonds, Å) | 0.003 | 0.002 | 0.007 | 0.003 | 0.006 | 0.014 | 0.005 | - | - |
| RMS (angles, deg) | 0.58 | 0.52 | 0.86 | 0.63 | 0.89 | 0.84 | 0.77 | - | - |
| Average B factor | 22.96 | 20.52 | 25.4 | 25.01 | 20.23 | 17.29 | 15.5 | - | - |

* $\alpha=\beta=\gamma=90^\circ$

a. Due to very few C482S crystals can be collected, the processing statistics were not ideal. Therefore, there were no refinement on C482S.

4.1.11 *CraCRY* mutational analysis of the relevant actors in $\alpha 22$ unraveling

After refining all the datasets from BL32XU, in order to demonstrate which relevant actor of the protein regions were most dynamic and causing $\alpha 22$ unfolding, the structures with their color-coded isotropic B -factor distributions are shown in Figure 22. First, we were able to get a WT_{Long/Semi} state with already high B -factors in the C-terminal region, following by c -axis compressing by ~ 5 Å in the WT_{Short/Semi} and $\alpha 22$ unfolding so that the model of the C-terminal region was unstructured also in the cryo-condition (Figure 22A). Next, we were able to confirm that $\alpha 22$ unfolding depended on photoreduction by the Y373F mutant, which is known to be incapable of photoreduction^{109, 111}. In this case, FAD remained in the oxidized state independently of illumination and 100% of crystals remained in the dark-adapted crystal form, independently of illumination (Figure 22B). Comparing to c -axis histogram distribution of the mutants, either Y373F_{Long/Ox} or Y373F_{Long/Semi} remained in the long c -axis region thus serving as a suitable negative control (Appendix 26).

On the other hand, mutating D321 to asparagine (D321N) prevented it from acting as proton acceptor from Y373, but also mimicked the already protonated D321 form by removing its charge. Spectroscopically, the mutant behaved exactly like WT *CraCRY*, with FAD achieving the FADH^{*} state upon illumination (Appendix 27), indicating that D321 can be replaced as proton acceptor, e.g. by water, as without deprotonation, the FAD^{*}/Y373⁺ RP would be too short lived for FADH^{*} accumulation¹⁰⁹.

Next, the second salt bridge partner of $\alpha 22$, D323, was mutated as well to D323N for weakening the second salt bridge. Furthermore, the D321N/D323N double mutant, in which both the D321-R492 and D323-R485 salt bridges were weakened, was generated. When observing these series of salt bridge relevant actors in the oxidized state, interestingly, the D323N mutant showed two main peaks in the oxidized state with shifts of ~ 0.5 -1 Å (Appendix 26). We think that due to cryo-condition may slight change the behavior in this specific mutant or somewhat other reason. However, from the structural view, the D323N_{Long/Ox/P1}, D323N_{Long/Ox/P2} (Figure 22C), D321N_{Long/Ox} (Figure 22D), and D321N/D323N_{Long/ox} (Figure 22E) showed very similar structures with higher B -factors starting around the C-terminal end of $\alpha 22$, even more in D321N/D323N_{Long/ox} indicating that salt bridge indeed affecting the stability of $\alpha 22$. In other words, as traced by the larger range covered by the B -factors, it showed an order of D321N/D323N_{Long/ox} > D321N_{Long/Ox} > D323N_{Long/Ox/P1} = D323N_{Long/Ox/P2} indicating that the D321 residue has a more pronounced role than D323 for $\alpha 22$ unraveling. On the other hand, the semiquinone D321N structure proved difficult to obtain, as crystals were strongly damaged upon illumination with blue light. Nonetheless, we were able to construct a dataset based on images from 44 crystals, which produced a 3 Å structure after combination. Here, we observed the same overall architecture as C_{signal} i.e. with a

completely delocalized $\alpha 22$ and an exposed Y373 in D321N_{Short/Semi}, D323N_{Short/Semi} and D321N/D323N_{Short/Semi}. By calculating the percentage of the short c -axis shifting of the semiquinone datasets, D321N and D323N showed more or less the same, but more in the double mutant as expected (Appendix 28).

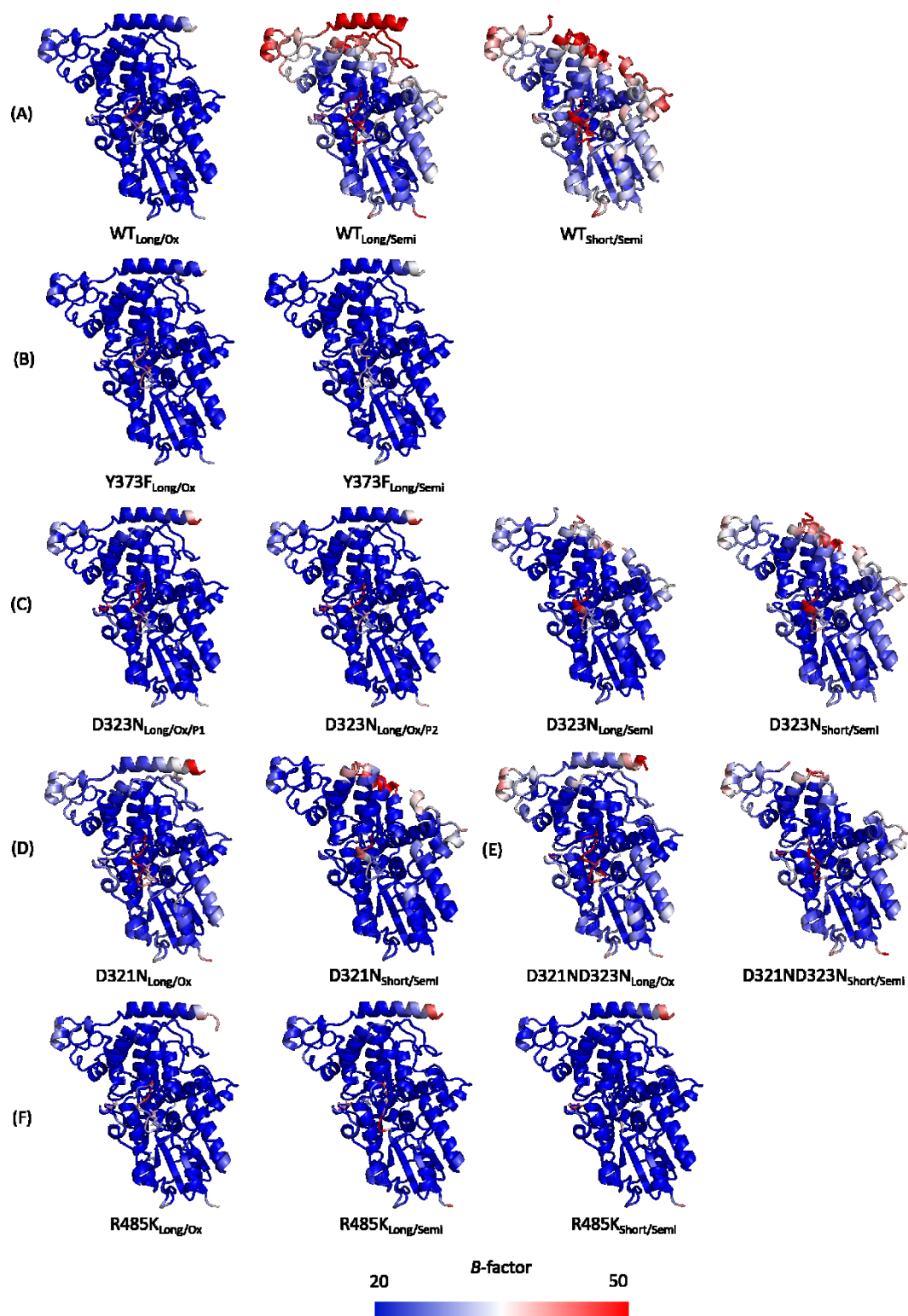


Figure 22. Overall relevant mutant structures assigning color by B-factor. B-factor coloring was done using a blue-white-red spectrum with a minimum value of 20 and a

maximum value of 50 \AA^2 . (A) and (B) were shown as positive and negative controls, respectively. Given (C), (D) and (E), the series of mutants in salt bridges between the photolyase-like domain and $\alpha 22$ showed similar features, with the most flexible C-terminus found for the double mutant. (F) R485K mutants showed all a well-ordered $\alpha 22$ helix, this may due to fast transition of the c-axis.

Finally, the mutation R485 to lysine (R485K) was made to change the interaction partner but still maintain the salt bridge with D323. Interestingly, both R485K_{Long/Semi} and R485K_{Short/Semi} were well-ordered at the $\alpha 22$ helix like in its oxidized state (Figure 22F). We think that R485K may change very rapidly between partial unfolding and refolding; only ~30% crystals can be hence observed with a shorter c-axis (Appendix 26, 28). To solve this problem, future millisecond of TR-SFX experiments may answer this question properly. Unfortunately, mutating cysteine to serine (C482S) was not successful in data collection (Table 5). The original idea of C482 was that the cysteine was in close proximity to the distal Y373 of the electron transfer tetrad, and a previous study proposed to act as a potential electron donor, which could form a disulfide bond with another oxidized species¹¹⁰.

In conclusion, illumination of the crystals prior to freezing triggered unfolding of the C-terminal region, achieving a state similar to C_{signal}. Thus, it appears that both the D321N and D323N mutations prime $\alpha 22$ for unfolding by weakening the D321-R492 and D323-R485 salt bridges, but that the electrostatic perturbation derived from Y373^{*} is still required to destabilize the C-terminal region enough to prevent folding under cryo-conditions.

4.1.12 Conclusion and outlook

Although cryptochrome-related research has always been somewhat enshrouded in mystery, currently, all evidence points towards RPs constituting the CRY signaling state^{44, 109, 130}. Furthermore, as orientation relative to Earth's geomagnetic field affects radical pair stability^{62, 131}, immobilized CRYs in migratory birds' eyes have been proposed to underlie magnetoreception¹³¹⁻¹³². Our data supports this notion by showing how *CraCRY* senses blue light by generation of a radical pair, translating the cryptochrome signal transduction into a transition from FAD^{•−} to FADH^{*} in several steps followed by extensive unfolding of its C-terminus. Previous time-resolved spectroscopic analyses showed that electron transfer proceeds through the tryptophan triad and causes initial formation of the biradical by ultrafast proton transfer to D321 to produce FAD^{•−}/Y373^{*} RP within less than an ns¹⁰⁹. To prove this process structurally, *CraCRY* should be activated via an ultra-rapid pump laser, e.g. at SwissFEL¹³³, whose optical fs-laser provides a pulse duration under 1 ps. According to our SACLA data between 10 ns and 100ns (Figure 18A and 18C), *CraCRY* behaved much like other PCSf⁷³, with N395 receding away from the flavin, while R360 approached it, stabilizing

FAD^{•-} and causing a loosening of the D321-R492 salt bridge. From these points of view, our entire *CraCRY* setup is highly suitable for faster time course analysis to decrypt structurally the ultrafast steps of radical pair formation.

Next, we suggested the proton source for the FAD^{•-} to FADH[•] transition to be the conserved R360 as in our previous research⁷³. By between 100 ns to 1 μ s, a rapid kinetic exchange happened for the R360 conformation (Appendix 16,17). From this point on, the FAD binding site remained constant. Afterwards, FAD^{•-} had already undergone protonation to FADH[•] via a proton transfer chain composed of at least R360, E384 and H309 within 33 ms, giving rise to the extremely long lived FADH[•]/ Y373[•] radical pair, followed by return of the relevant residues of the transient protonation pathway to their original conformations (Figure 18B). Clearly, we can observe the strong evidence of FADH[•] formation in 100 ms in TR-*icOS* (Figure 20) and supporting our models proposed a protonation mechanism that is taken place in milliseconds.

However, the largest conformational changes underlying the basis of *CraCRY* signal transduction took place in the C-terminal region surrounding Y373. The ultrafast D321 shift as described increases with its main interaction partner, R492, as it was completely delocalized by 3 μ s (Figure 18C, Appendix 20). Given this effect, water molecules were able to hydrate the space between α 22 and the main protein body, which in turn reduced the strength of the nearby salt bridge of D323-R485 and continued to do so over the rest of the time-course. With both salt bridges broken, the C-terminal residues becoming partially or fully delocalized at 233 ms, with diffuse negative density accumulating throughout the entire helix α 22 (Appendix 22). Ultimately, the helix can be observed in the C_{signal} structure of being completely unfolded, leading to strong re-arrangements in nearby loop regions (Figure 13). Although our longest time point of the 233 ms model give us a very good support for an unfolding of the entire α 22 helix, there is still a huge jump towards completely unraveling. To address this, in the future, millisecond time-resolved serial oscillation crystallography¹³⁴⁻¹³⁵ (TR-SOX) should be performed at the ESRF to observe and determine the continuous unfolding models in detail on millisecond to second time frames. Overall, the most important conclusion from our findings is that the presence of Y373[•] is sufficient and necessary to trigger the transition towards the C_{signal} state.

On the other hand, *CraCRY*'s multi-functionality mentioned above require a second round of photoreduction (Figure 12) to achieve DNA repair activity by reduction of FADH[•] to FADH⁻^{69, 136}. This reaction may be however also represent the base for a secondary function as a red light photoreceptor¹¹⁰. It is still unclear how *CraCRY* acts as a red light photoreceptor for FADH[•] to FADH⁻ conversion. An obvious hypothesis states that if Y373[•] regenerates to Y373 when being provided with a reducing agent in C_{signal}, α 22 refolding may take place and resulting in a non-signaling, red light sensitive

FADH[•] state (FADH[•]/Y373). Upon red light illumination, FADH[•] would undergo photoreduction 2, resulting in a hypothetical FADH[•]/Y373[•] C_{signal/red} state. Again, an external reducing agent may then regenerate Y373[•] to Y373 again to achieve the final C_{cat} state (FADH/Y373) and maintaining the canonical PCSf architecture required for DNA repair. To address this, first, C_{signal} crystals can be produced as usual, followed by adding reducing agent in the dark to regenerate Y373[•] to Y373 as the initial step of C_{FADH/Y373} model. Next, by TR-SOX experiments data collection with constant red light illumination simultaneously, we may obtain and observe the refolding events taking place, and finally ending up with the refolded model of C_{FADH/Y373} (Figure 13, C_{cat}). Finally, due to our *CraCRY* experimental setup without secondary chromophore (8-HDF), it would be interesting to analyze whether photoreduction is affected if the antenna chromophore 8-HDF is present or not. Surprisingly, when we superposed the previously published 8-HDF containing *CraCRY* model (6FN2)¹¹¹ with our C_{10ns}, isomorphous difference electron densities we could observe strong difference densities around the 8-HDF binding pocket. Here, we could observe the isomorphous difference electron densities decaying in K13, E107, H134, Q390 and disappearing until 10 us, indicating the relevant residues may compose another proton transfer chain and capture proton from the solvent environment.

4.2 Observing DNA post-repair dynamics in *CraCRY*-(6-4)PP complex

4.2.1 Overview of (6-4)PP repair in *CraCRY*

Upon exposure to UV radiation, two major types of compounds resulting from DNA damage were are, i.e. pyrimidine cyclobutane dimers (CPDs) and pyrimidine-pyrimidone (6-4) photoproducts⁹⁻¹⁰ (Figure 1). To repair these types of DNA photolesions, CPD-photolyases and (6-4)-photolyases use the energy of blue light to repair CPD and (6-4)PP lesions, respectively^{65, 69, 76}. Meanwhile, once the photolesions had been recognized, the damaged bases are forced out of the DNA double strand and into the photolyase active site via a poorly understood mechanism, resulting in a two nucleotide-long single stranded DNA locus called the unpaired bubble¹³⁷⁻¹³⁸. In turn, the unpaired bubble is stabilized by the photolyase bubble intruding region (BIR)¹³⁹. The function of BIR prevents the collapse of the unpaired bubble and is highly conserved in all known photolyase-DNA co-crystal structures^{136, 139}. The CPD repair mechanism and the base return pathway, followed by the initial stages of complex dissociation have been studied by us in detail via time resolved serial femtosecond crystallography (under revision). However, the (6-4)PP repair mechanism has been somewhat enshrouded in mystery, and several possible mechanisms have been proposed, but are still an issue of controversy (Section 1.5.2). Given that the first *CraCRY*-DNA co-crystal structure was consistent with a two-photon mechanism for (6-

4)PP repair, it was hypothesized that intermediate X may be a transiently formed oxetane within the (6-4)PP molecule^{87, 111}. Additionally, the post-repair base return and complex relaxation mechanism for (6-4)PP remained unknown. Overall, our findings in this thesis show the final stages demonstrating a significant portion of the poorly understood (6-4)PP repair mechanism.

4.2.2 Structure solution of (6-4)PP repaired models

In this work, we present six different *CraCRY*-DNA co-crystal structures corresponding to five different levels of illumination with a 5 mW, 405 nm laser (dark, 4 s, 8 s, 16 s, 32 s, Table 6) in the presence and absence of a reducing agent (DTT), and the overall co-crystals production and methodology were well-introduced in Section 3.6 and 3.18 respectively. By exposing the crystals to low levels of light over long periods of time, we hoped to enrich, isolate and structurally characterize one or more of the main intermediates in the (6-4)PP post-repair process by *CraCRY*. In addition, we performed a negative control experiment by illuminating crystals for 16 s in the absence of DTT. In the following sections, we refer to the structures called accordingly, i.e. *dark*, *4s*, *8s*, *16s*, and *control*. Meanwhile, we produced high quality difference density maps (dFo) between isomorphous datasets (*dark*, *4s* and *8s*)¹²⁴. Interestingly, prolonged illumination for the *16s* dataset caused significant shifts in the crystal lattice (Table 6), and therefore DFO-mFc (DFO_{16s}-mFc_{dark}) maps were used instead¹⁴⁰. Furthermore, by estimating the activated fraction in each of the illuminated datasets, we could use structure factor extrapolation techniques^{73, 121} to structurally characterize two long-lived intermediates of the (6-4)PP post-repair events for the *4s* and *8s* datasets. Meanwhile for *16s*, the activated fraction accounted for 80-100% within the crystal, and therefore non-isomorphous extrapolation was not performed.

Table 6. TPS07A data statistics for (6-4)PP repairing structures. Numbers in parenthesis describe the highest resolution shell.

| Time point | dark | 4s | 8s | 16s | Control _(16s) | 32s |
|-----------------------|-------------------------|-----------------------|-----------------------|-----------------------|--------------------------|-----------------------|
| Space group | $P4_32_12$ | | | | | |
| Unit cell (a, b, c)* | 189.29, 189.29, 45.99 | 189.29, 189.29, 45.99 | 189.01, 189.01, 46.15 | 188.14, 188.14, 45.98 | 187.96, 187.96, 45.98 | 187.45, 187.45, 45.91 |
| Processing statistics | | | | | | |
| Completeness (%) | 99.69 (100) | 99.96 (99.97) | 99.92 (100) | 99.72 (99.95) | 99.93 (100) | 99.56 (100) |
| Unique reflections | 52134 (7629) | 43891 (6794) | 43001 (6659) | 48950 (7918) | 42372 (6330) | 29104 (4552) |
| Multiplicity | 242.5 | 207.1 | 209.7 | 224.5 | 201.8 | 34.4 |
| CC1/2 | 0.993 (0.525) | 0.988 (0.545) | 0.985 (0.645) | 0.998 (0.573) | 0.995 (0.512) | 0.959 (0.536) |
| I/ σ | 7.85 (1.67) | 9.59 (1.89) | 12.32 (2.02) | 16.33 (2.14) | 7.45 (1.44) | 6.15 (1.2) |
| Wilson B factor | 22.04 | 25.69 | 38.64 | 38.51 | 29.47 | 34.46 |
| Refinement statistics | | | | | | |
| Resolution range (Å) | 18.39-2.14 (2.216-2.14) | 45.91-2.4 (2.486-2.4) | 44.84-2.5 (2.589-2.5) | 18.45-2.2 (2.279-2.2) | 46.99-2.3 (2.382-2.3) | 18.06-2.5 (2.589-2.5) |
| Unique reflections | 46716 (4598) | 33414 (3255) | 29647 (2912) | 42494 (4145) | 37290 (3622) | 28924 (2830) |
| Rwork | 0.1905 (0.2448) | 0.2394 (0.3196) | 0.2542 (0.3771) | 0.1889 (0.2603) | 0.2066 (0.3124) | 0.2318 (0.3132) |
| Rfree | 0.2376 (0.2704) | 0.2739 (0.3456) | 0.2788 (0.4088) | 0.227 (0.2909) | 0.2544 (0.3544) | 0.2551 (0.3221) |
| Ramachandran outliers | 0.21 | 0.21 | 0.21 | 0 | 0.41 | 0 |
| RMS (bonds, Å) | 0.017 | 0.007 | 0.006 | 0.002 | 0.011 | 0.024 |
| RMS (angles, deg) | 1.88 | 0.92 | 0.75 | 0.57 | 1.48 | 1.12 |
| Average B factor | 44.72 | 38.83 | 50.74 | 58.57 | 50.15 | 58.57 |

* $\alpha=\beta=\gamma=90^\circ$

4.2.3 Overall structural changes after (6-4)PP DNA repair

As with any catalytic reaction, DNA repair by *CraCRY* involves at least three steps, i.e. formation of the enzyme-substrate complex ($E+S \rightarrow ES$), transformation of ES into the enzyme-product complex ($ES \rightarrow EP$), and release of the product by dissociation of the EP complex ($EP \rightarrow E + P$) (Figure 23A). Similar to previous reports for the *CraCRY*-DNA complex structure¹¹¹, our co-crystals featured the pre-formed ES in *dark* (Figure 23B), in which the (6-4)PP moiety was held close to the FAD co-factor, and was bound between W294, H357, H361 and W401 (Figure 23C). Meanwhile, *CraCRY*'s bubble intruding region, corresponding to the F408 to R413 peptide, occupied the unpaired bubble, preventing its collapse (Figure 23D).

Interestingly, although the *CraCRY* protein moiety did not appear to undergo extensive conformational changes upon light illumination, DNA-localized changes were extensive, and illumination-dependent (Figure 23E). Here, both 4s and 8s difference maps localized to the (6-4)PP and its environment (Figure 23E). Meanwhile, 16s presented the most extensive conformational changes to the DNA, as large portions become too flexible to be refined conventionally and are hence disordered (Figure 23E). In the $DFo_{16s}-mFc_{Dark}$ map, strong negative difference peaks could be observed along the position occupied by the entire DNA molecule (Figure 23E).

In addition, the 16s superdataset had undergone significant changes in the crystal lattice, with the *a* and *b* axis being shortened by 1 Å, while the unique *c*-axis remained constant when compared to *dark* (Table 6 and Appendix 30). This could be explained by the partial dissociation of the protein-DNA complex. Accordingly, we assigned the 16s state as an intermediate stage between EP and $E+P$, $[E+P]_{16s}$ (Fig. 23A). However, in $[E+P]_{16s}$, DNA release had not been completed yet. Here, the entirety of the 5' DNA arm could not be refined due to disorder in 16s, but parts of the 3' arm could (Figure 23E). We further illuminated for 32 s, at which point the majority of crystals had completely dissolved. The resulting 32s super-dataset was constructed from only 51 sub-datasets collected from several loops (Table 6), resulting in a structure which differed very little from the 16s state (Figure 23A, Appendix 31). This indicated that $[E+P]_{16s}$ was the latest stage in the (6-4)PP post-repair process that can be captured by the current methodology, before diffraction power was lost due to deterioration of the crystal lattice.

Finally, we performed the control measurement of 16 s light illumination in absence of reducing agent, the result showed little differences to *control* and *dark* (Appendix 32), highlighting that DNA repair only takes place in catalytically active form of flavin, the $FADH^{\cdot-}$ state.

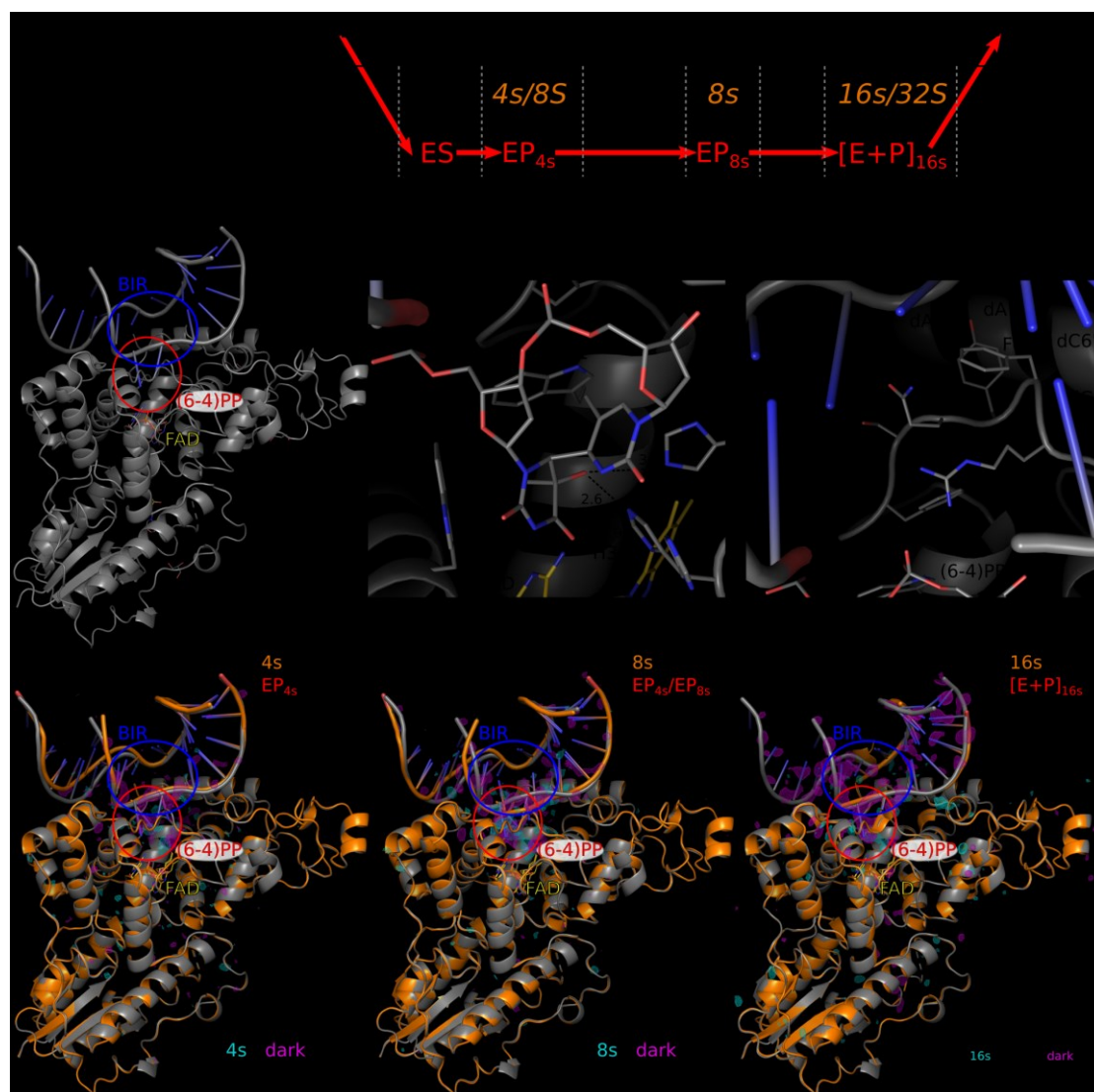


Figure 23. Overview of structural changes after CraCRY mediated (6-4)PP repair. (A) Reaction overview. Overall reaction shows the general steps for an enzyme catalyzed reaction, i.e. enzyme (E) and substrate (S) combine to form the enzyme-substrate complex (ES), which then reacts to the enzyme product complex (EP). The reaction is over when the product is released, and the enzyme is ready for a new reaction cycle (E+P). Here, we present a total of four structures showing different intermediate stages along this pathway for the CraCRY catalyzed (6-4)PP reaction, i.e. dark, 4s, 8s, 16s, and 32s, which harbor one of three reaction intermediates, ES, ES_{4s}, ES_{8s} and [E+P]_{16s}. (B) Overview of dark structure as a cartoon representation, highlighting the BIR/unpaired bubble region (blue, BIR), the (6-4)PP-occupied active site (red, (6-4)PP), and the FAD moiety (yellow, FAD), as well as the 5' and 3' DNA arms. Both in the overall topology and in detailed features, the dark state shows no significant difference to the published CraCRY-DNA complex structure¹¹¹. (C) Detail of the (6-4)PP-occupied active site with both the (6-4)PP and relevant interacting residues as gray stick models, as well as the nearby FAD (gold). All interatomic distances are shown in Å. (D) Detail of the bubble intruding region and unpaired bubble, with DNA and protein backbone elements as cartoons, while relevant protein side-chains as stick models. (E) Overall structural changes in 4s, 8s, and 16s, representing EP_{4s}, EP_{8s}, and [E+P]_{16s}, respectively. Protein and DNA moieties of each individually illuminated structure are shown in orange, in the same orientation as in (B), and superposed over dark (gray).

Additionally, difference electron density maps are shown at a 3.5σ contour level, with positive values in cyan, negative values in magenta.

4.2.4 Active site structural changes after (6-4)PP DNA repair

Although the $4s$ structure showed no significant overall architectural changes (Figure 23E), strong dFo peaks in the immediate environment of (6-4)PP suggested local changes, resulting in one or more EP stages (Figure 23A and 23E). Indeed, refinement of the $4s$ dataset with extrapolation techniques^{73, 121} permitted the enrichment and refinement of a distinct EP intermediate with an occupancy of 33.3%, which we named EP_{4s} (Figure 23A and 24A-C). Whereas, the $8s$ resulted in two major post-repair conformations being found in the vicinity of the active site (Appendix 33), with one of them being EP_{4s} (Figure 24C), and the second one EP_{8s} (Figure 24D). Here, the total active fraction was estimated at 40%, with EP_{4s} being more highly occupied than the EP_{8s} state, as demonstrated by the stronger EP_{4s}-derived signals in $8s$ (Figure 24D and Appendix 33).

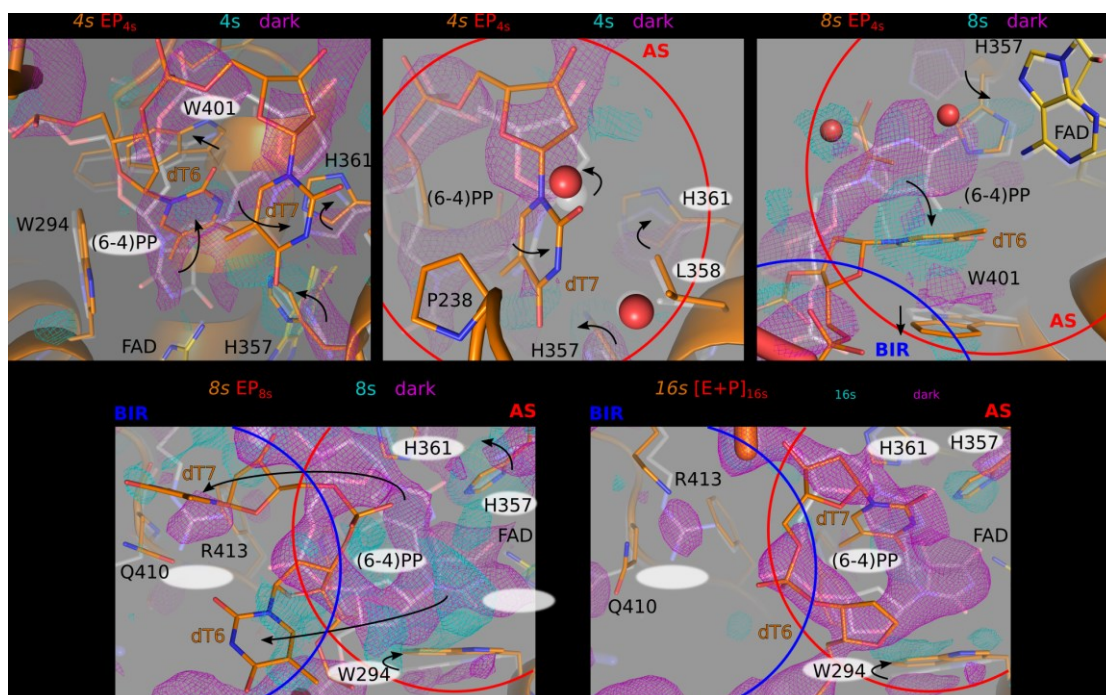


Figure 24. Post-repair dynamics of (6-4)PP and the active site. (A) Detail of the $4s$ (orange) active site harboring the EP_{4s} intermediate superposed over the dark active site (gray). Protein and DNA backbone is shown as cartoons, with individual side-chains as stick models. The 3.5σ contoured dFo($4s$ -dark) map is shown in cyan and magenta for positive and negative peaks, respectively. Movement of individual residues is highlighted by arrows pointing from their original positions in dark to their final positions in $4s$. (B) Side-detail of dT7, highlighting its sandwiched position along the water-filled crack between P238 and L358. The active site area is highlighted as a red circle. Water molecules within the crack are shown as red and gray spheres for $4s$ and dark, respectively. All other elements are shown as in (A). (C) Side-view of dT6 in the

EP_{4s} from the 8s structure with the boundaries of active site (AS) as a red circle, while those of the bubble intruding region as a blue one. All elements are shown as in (B) and (A). (D) Detail of the 8s EP_{8s} intermediate structure. Both dT6 and dT7 have flipped out of the active site (red circle), and are in the process of entering the unpaired bubble by displacing the BIR (blue circle). The panel is rotated 90 degrees clockwise from the orientation in (A), but otherwise structures are displayed as in all other panels, however the dFo(8s-dark) map is contoured at 3 σ to highlight the relatively weak difference density around the back-flipped dT6 and dT7. (E) Detail of the mixed states of 16s, which include [E+P]_{16s}. Figure is shown as in (D).

In EP_{4s}, (6-4)PP had been fully repaired (Figure 24A); as a result, the 3' thymine (dT7) rotated by 90° and shifted by 2.1 Å, suggesting that dT7 would promptly exit the active site via a water-filled crack between L358 and P238 (Figure 24B). Meanwhile, the 5' thymine (dT6) moved deeper into the active site, allowing water to invade the active site, with two or three additional water molecules found in EP_{4s} compared to ES (Figure 24C). Furthermore, the dT6 inward motion and 120° rotation profoundly altered its interaction network, as it is stacked with W401, pushing against it (Figure 24C). Meanwhile, H357, which had presented two equally populated alternative conformations in ES (Figure 23C), now occupied a single position which allowed it to interact directly with O4 of dT6 (Figure 24A), while the H361 side-chain rotated by 16° along its C α -C β bond, thus also orienting its N ϵ atom towards dT6 O4 (Figure 24A and 24B). Interestingly, H357 and H361 had been unequivocally connected to (6-4)PP repair⁸⁴, either as part of a water transfer mechanism⁶⁹, or via stabilization of an oxetane intermediate¹¹¹. Although our data cannot unambiguously discriminate between these two possibilities, the (6-4)PP repair-dependent changes in both histidines clearly show their role in post-repair stabilization of dT6 in the EP_{4s} stage.

In EP_{8s}, both dT6 and dT7 had left the active site (Figure 24D). Meanwhile, W294 slid towards the active site in 8s compared to EP_{4s} 4s (Figure 24A and 24D). We interpreted this as the result of the double conformation of dT6 in 8s, with the highly occupied EP_{4s} dT6 maintaining most of the features observed in 4s, while dT6 flipped in EP_{8s} allowing W294 to enter the active site.

Finally, in 16s, no unique dT6 conformation could be completely modeled, as the entire thymidine moiety was unable to be determined. Meanwhile a 70% occupied dT7 could still be refined within the active site in a conformation similar to EP_{4s} (Figure 24E). Thus, this suggests about ~70% of the complex population remaining in an EP_{4s}-like conformation, while ~30% completely missed the 5' arm of the DNA duplex (Figure 23E) and adopted a highly dynamic state as represented the partially released [E+P]_{16s} state.

Overall, our structures indicate that the post-repair process within the *Cra*CRY active site follows an ordered scheme by which the repaired bases leave the active site. First,

base repair resulted in fast release of dT7, and stabilization of dT6 via hydrogen bonding and π - π stacking (EP_{4s}, Figure 24A). dT6 was released at a later stage, and a process which was promoted by stabilization of the empty active site pocket via increased hydration and intrusion of W294 (EP_{8s}, Fig. 24D).

4.2.5 Detailed structural changes of the BIR releasing

As described above, during the initial stages of DNA release from the *CraCRY*-DNA complex, the repaired dT7 and dT6 flip out of the active site. Later, they must also enter the unpaired bubble, as shown in EP_{8s} (Figure 24D). However, because the *CraCRY*-bound unpaired bubble is stabilized by BIR (Figure 23D), the BIR must release the bubble and allow the bases entering it. Our structures demonstrate how these two events, namely base-flipping and BIR release, are coordinated via a pathway involving the dT7-R413 and the dT6-W401 interactions.

First, in our EP_{4s} containing structures, we observed that W401 π -stacking with dT6 in the active site caused W401 to slide by 0.6 Å towards BIR (Figure 24C), which in turn caused a shift of 0.3 and 1.3 Å in F407 and F408, respectively (Figure 25A). This change was caused via the S409 peptide backbone towards Q410, F412 and R413 (Figure 25B), which together with F408 formed BIR. Here, the partial dT7 exit from the active site caused re-arrangements of the dT7 phosphate moiety, which resulted in R413 moving away from its original position close to the dT7 phosphate, and towards Q410 (Figure 25B). This series of conformational rearrangements resulting from (6-4)PP repair in EP_{4s} caused the F408 side-chain to rotate by 26°, retracting towards the protein and moving out of the BIR. Meanwhile, the Q410 side-chain rotated by 28.5°, approaching R413 and breaking a π - π interaction with dA8', which, as a result, left the unpaired bubble (Figure 25B). In the 8s state, the positions of W401, F407, F408, and dA8' were similar to the 4s state, perhaps due to both the EP_{4s} and EP_{8s} intermediates being present within the 8s structure (Figure 25C). However, with dT7 entering the unpaired bubble, the R413 side-chain got completely delocalized, while the Q410 side-chain rotated by 101.5° and hydrogen-bonded with dT7 via the Q410's NE2 atom (Figure 25C). Finally, along with the highly dynamic dT7 and R413, the side-chain of Q410 only rotated by further 71° without interaction partner, resulting in partial dissociation of [E+P]_{16s} (Figure 25D).

These findings highlight how the (6-4)PP repair status is relayed via dT7-phosphate re-arrangements towards R413 to initiate C-terminal BIR release from the unpaired bubble, while dT6 interaction with W401 relays the same information towards the N-terminal BIR region. We propose that synchronization between the active site and BIR underlie the suggested kinetics for base release, namely fast dT7 release followed by slower dT6 release. While R413-mediated conformational changes in BIR are permanent upon dT7

entering the unpaired bubble, W401 can only act as a relay while dT6 is interacting with it. Thus, maximizing the duration of both interactions commits the complex into the base-flipping pathway. Finally, dT6 and dT7 entering the unpaired bubble arrests both it and the BIR towards complex release.

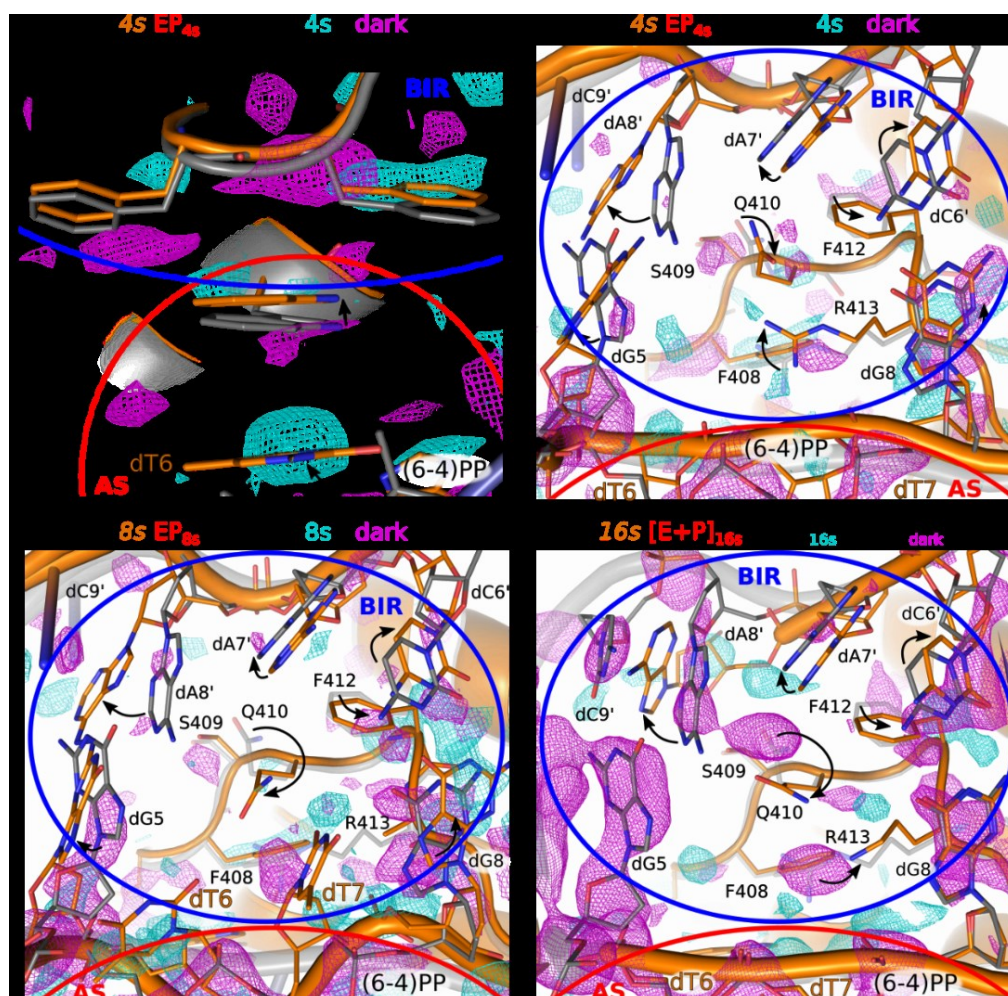


Figure 25. Post-repair dynamics in the bubble intruding region and unpaired bubble. (A) dT6-W401 relayed interaction between the active site (red circle) and the BIR (blue circle) in the EP_{4s} intermediate. Protein backbone is shown as cartoon, with relevant side-chains as stick models, with 4s in orange, and dark in grey. The 3σ-contoured dFo(4s-dark) map highlights differences between the two structures, with positive peaks in cyan, while negative ones in magenta. Arrows indicate movement between dark and 4s. (B) Conformational changes in BIR and the unpaired bubble for EP_{4s} intermediate. Structures and difference maps are shown as in (A), with the BIR and active site highlighted by blue and red circles, respectively. (C) Conformational changes in BIR and the unpaired bubble for EP_{8s} intermediate. The 8s (orange) and dark (gray) structures are shown as in (B), including the same orientation, dFo contour level, etc. (D) Conformational changes in BIR and the unpaired bubble for [E+P]_{16s} intermediate. The 16s (orange) and dark (gray) structures are shown as in (B), including the same orientation. The 3σ-contoured DFO_{16s}-mFc_{dark} is shown in the same color scheme as the dFo maps in (A), (B), and (C).

4.2.6 Conclusion and outlook

In this work, we elucidated the events which immediately occur after *in crystallo* (6-4)PP repair by *CraCRY* via fixed target serial crystallography. We were able to determine the structure of three reaction intermediates, EP_{4s}, EP_{8s} and [E+P]_{16s}, where (6-4)PP has been fully repaired, but has not yet left the active site. In particular, EP_{4s} represents an early post-repair stage in which the 3' base has started back-flipping, while the 5' is still buried within the active site pocket (Figure 24A). In EP_{8s} both bases have left the active site, but BIR, the protein elements stabilizing the DNA strand, has not yet been fully displaced (Figure 25C). With partial release of the DNA molecule in [E+P]_{16s}, the BIR residues are still being displaced (Figure 25D), probably only returning to their original positions upon complete product release. Importantly, the [E+P]_{16s} estate strongly suggested that its unpaired bubble had been closed upon partial DNA release, as the entirety of the 5' arm had disappeared (Figure 23E), given no ordered bases upstream from dT6 and dA8'. Meanwhile, all other bases overlapped with strong negative density peaks (Figure 25C), resulting in decreased occupancy for the entirety of the DNA.

This highly detailed mechanism contrasts with the challenge in determining post-repair features by spectroscopic techniques, where, once repaired, the neighboring thymines constituting (6-4)PP have essentially the same characteristics, whether they are in the active site, or embedded within the DNA molecule^{69, 88}. Overall, these structural data shows the final stages in (6-4)PP repair in detail demonstrating a significant portion of the poorly understood (6-4)PP repair mechanism. More importantly, it provides great molecular insight into the mechanisms and kinetics of DNA-protein interactions.

Furthermore, our data and methodology clearly shows that (6-4)PP repair by photolyases can be studied via time-resolved crystallographic techniques. Recently, we had been able to collect the SFX data in SACLA with oxidized *CraCRY*-DNA complex in a test run. We expect that TR-SFX experiments will further elucidate and decrypt the precise reaction intermediates during the entire (6-4)PP repair reaction.

4.3. Protonation study on mutant *Methanosarcina mazei* class II DNA photolyases

Protonation of the radical anion flavin (FAD^{•-}) at the N5 position is essential for the photoreduction to form neutral semiquinone (FADH[•]). As our previous study had shown that the geometry of the Arg378–Asp409 salt bridge was strongly affected by FAD^{•-} and its protonation⁷³, the R378Nε may act as transient proton donor for the transition of FAD^{•-} to FADH[•]. In this work, based on our findings⁷³, Dr. Igor Schapiro group has demonstrated via QM/MM simulation that a proton transfer event only takes place from R378Nε, and only if the Nε atom is stabilized by a nearby water and E407 (Appendix 34A). Indeed, either simulation or our previous study⁷³, the water movement can be

observed and stabilized N ϵ via hydrogen bonding (Appendix 34B). Thus, in order to investigate the protonation relevant partners, we mutated E407 to leucine (E407L), as E407 is not widely conserved outside the group of class II DNA photolyases, but mainly occurring as leucine in class I DNA photolyase and cryptochromes. Here, we propose that, in the E407L mutant, R378 proton transfer is transient, with protons being donated from solvent via the cavity opened due to the mutation as described in the following section.

4.3.1 E407L preparation, crystallization and data acquisition

E407 was mutated to leucine by the QuikChange lightning site-directed mutagenesis kit (Agilent). The plasmid vector was used pET28a and transformed into *E. coli* BL21 (DE3). For protein expression, cells were grown in terrific broth medium with kanamycin at 25 °C. The gene expression was controlled by auto-induction and incubated for at least 24 to 27 hours. After cell harvesting, pellets were re-suspended in buffer A (50mM NaH₂PO₄ PH 8.0, 300 mM NaCl) and added the tip of a spatula of lyophilized DNase and lysozyme. Cell disruption was performed with a high pressure homogenizer (EmulsiFlex-C3, Avestin) and centrifuged at 4 °C with 12000 rpm for 60 minutes. After centrifugation, the supernatant was sterile-filtered and applied to Ni²⁺-NTA agarose matrix (Roche) packed column which was equilibrated by buffer A in advance. The column was washed by 5 column volumes (CVs) of buffer A and afterwards by 5 CVs of 10% buffer B (50 mM NaH₂PO₄ PH 8.0, 300 mM NaCl, 250 mM imidazole) as second washing step. Next, E407L protein was eluted out of Ni²⁺-NTA column by 100% buffer B. Finally, followed by size exclusion chromatography with a Superdex200 column and gel filtration buffer (10 mM Tris-HCl, 100 mM NaCl, pH 8.0). For E407L protein crystallization, neither the original crystallization of the wild type nor modified crystallization conditions could succeed to obtain crystals. However, E407L co-crystallized with DNA was obtained as microcrystals (0.1 M Sodium acetate pH 4.6, 0.25 M ammonium sulfate, 4% PEG4000) (Figure 26) using previous conditions (under revision).

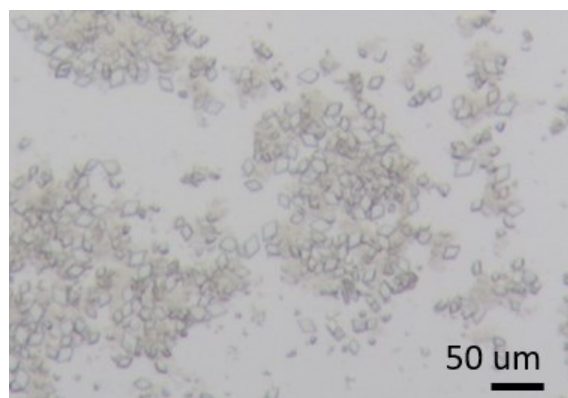


Figure 26. E407L-DNA co-crystals feature. The co-crystals had shown plenty and tiny crystal features with below 10 μm crystal size.

To obtain different redox states, the grown oxidized crystals had been covered in the dark for at least 12 hours to make sure that they are completely oxidized. Then, the E407L-DNA microcrystals slurry was embedded in a hydrophobic grease matrix in a 1:9 crystal:matrix ratio and flash-frozen. Likewise, the semiquinone crystals were generated by illumination for 5 minutes of embedded crystals and immediately flash-frozen in liquid nitrogen with light being switched off. Diffraction data were collected from a large amount of microcrystals to generate complete datasets at the beamline BL32XU, SPring-8, Sayo, Japan, with an EIGER X 9M detector. For data processing, the *KAMO* system has been used, which automates the data processing of multiple small-wedge partial datasets and subsequent merging¹²⁵. The refinement statistics for the E407L structures are summarized in Table 7.

Table 7. Refinement statistics for E407L structures. Numbers in parenthesis describe the highest resolution shell.

| E407L redox state | E407L _{ox} | E407L _{semi} |
|-----------------------------|------------------------|-----------------------|
| Space group | $P2_12_12_1$ | |
| Unit cell (a, b, c)* | 71.68, 114.83, 167.23 | 71.3, 115.49, 167.35 |
| Resolution range (Å) | 47.33-2.35 (2.434-2.3) | 47.53-2.3 (2.382-2.3) |
| Unique reflections | 57994 (5594) | 62139 (6104) |
| Completeness (%) | 99.42 (97.58) | 99.96 (100) |
| Wilson B factor | 41.21 | 42.43 |
| Macromolecules | 8145 | 8149 |
| ligands | 111 | 111 |
| solvent | 481 | 424 |
| Reflections used for R-free | 2894 (288) | 3101 (317) |
| R-work | 0.2182 (0.3369) | 0.1783 (0.2478) |
| R-free | 0.2449 (0.3641) | 0.2176 (0.3211) |
| Ramachandran outliers | 0.45 | 0.34 |
| Clashscore | 2.2 | 5.6 |
| RMS (bonds, Å) | 0.012 | 0.005 |
| RMS (angles, deg) | 1.53 | 0.71 |
| Average B factor | 47.61 | 52.11 |

* $\alpha=\beta=\gamma=90^\circ$

4.3.2 *MmCPDII* E407L mimics *CraCRY* behavior (transition from FAD_{ox} to FADH^{\bullet})

In photolyases, and in the absence of an external reducing agent, photoreduction stops at the step of the FAD_{ox} to $\text{FAD}^{\bullet-}$ transition, but is unable to proceed further to FADH^{\bullet} ^{64, 141}. Further, as we mentioned above, E407 in class II DNA photolyases is not widely conserved, and mainly replaced by leucine in class I DNA photolyase and cryptochromes. Interestingly, when we superposed the published *MmCPDII* and *CraCRY* structures, there was no crystallographic water near the leucine in contrast to the glutamate residue (Appendix 35A). Accordingly, in the E407Lox model, no crystallographic water can be found nearby L407 (Appendix 35B). Additionally, another evidence as suggested by molecular dynamic simulations, where E407 was replaced by leucine showed a very low density for water, indicating that the water had been indeed stabilized by the polar E407 in the *MmCPDII* structure (Appendix 36).

Surprisingly, upon light illumination for 5 minutes, E407L showed a FAD_{ox} to FADH^{\bullet} transition in its UV/Vis spectra in contrast to the WT of *MmCPDII* (Figure 27). Furthermore, after elution purification step in Ni^{2+} -NTA column, the deep blue color characteristic for the semiquinone state could be observed in E407L as well, similar to *CraCRY* (Figure 27). Clearly, the E407L mutant mimics *CraCRY* behavior to achieve a stable FADH^{\bullet} species in the absence of a reducing agent.

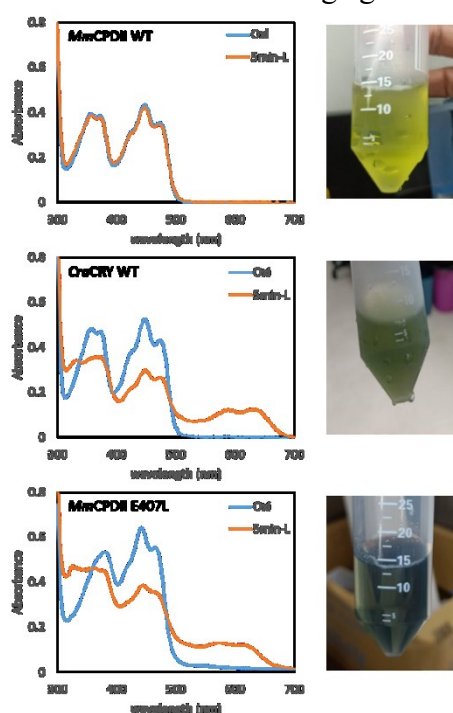


Figure 27. Features of the semiquinone state in both the *MmCPDII* E407L mutant and *CraCRY* WT. As the spectra indicated, upon light illumination for 5 minutes, FADH^{\bullet} was detectable in the absence of a reducing agent in E407L thus displaying high similarity to *CraCRY*; the same can be observed for the crude protein obtained after NiNTA-chromatography as first purification step.

4.3.3 Possible mechanism of proton donation from solvent

As our previous study suggested that the geometry of salt bridge is changed, causing the R378 side chain to break its salt bridge with D409 with a swiveling motion from both side chains during protonation⁷³. Unlike 4.8 Å of R378Nε to N5 distance in oxidized WT, a distance of only 3.5 Å in E407L_{ox} in between could be found for its structure. Here, in a good agreement with our previous findings, upon light illumination, E407L_{ox} revealed a very clear negative signal above the R378 side chain, and additional difference map peaks surrounding the guanidinium moiety, which appear to be consistent with a protonation event taking place with concomitant weakening of the salt bridge (Figure 28). Finally, the FADH' formation shows a 4.6 Å distance between R378 and the N5 position (Figure 28). Interestingly, in E407L_{semi}, L407 had shift upwards 1.1 Å, resulting in R378 having more connection to the solvent. Meanwhile, L367 rotated 110° from the original position in the oxidized state as well as W381 receding away by 0.4 Å (Figure 28). Based on these observations, we propose that in the E407L mutant, the R378-mediated proton transfer is transient, with protons being donated from solvent via the cavity opened upon illumination due to the mutation. In conclusion, our finding of E407 residue is extremely important for the protonation, as substitution of E407 with leucine completely altered the photoreduction behavior compared to WT *Mm*CPDII. In the future, it will be interesting to apply TR-SFX to investigate this specific mutation in the photolyase photoreduction process.

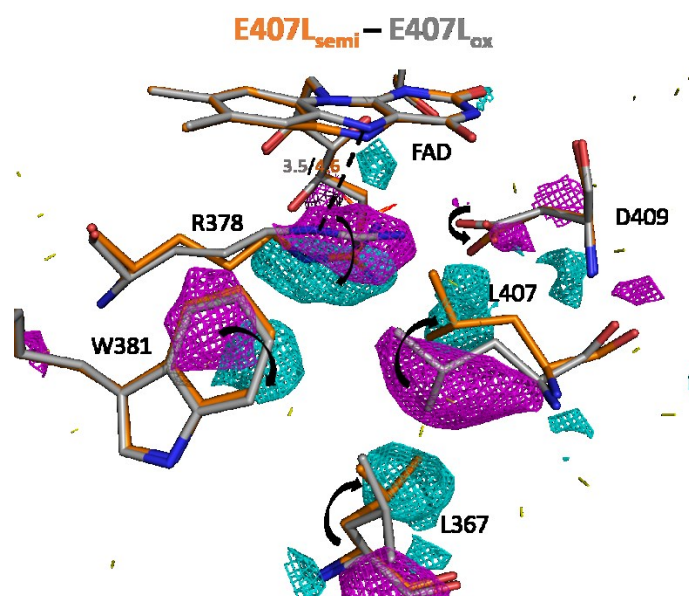


Figure 28. In *Mm*CPDII E407L, R378 was more directly connected to solvent. Relevant side-chains as stick models, with E407L_{semi} in orange, and E407L_{ox} in grey. The 3.5σ-contoured dFo(semi-ox) map highlights differences between the two structures, with positive peaks in cyan, while negative ones in magenta. The movement of individual residues is highlighted by arrows pointing from their original positions in oxidized to their final positions in semiquinone.

5. Perspectives

Enzymology is aiming to understand how enzymes work through the relationship between structure and function. In the past three decades, many functional enzymology studies have been performed, while advanced techniques for their analysis are continuously developing. However, from a structural point of view, although several strategies are able to obtain a view on the enzyme itself or of enzyme-substrate complex models, determining intermediates of complex enzymatic reaction is still somewhat challenging. During the last decade, time-resolved serial femtosecond X-ray crystallography has been well developed as a mature technique and allowed to observe the conformational changes in light-driven biological systems, i.e. a structure-based solution to determinate the intermediate models at different time scales after triggering by light illumination. In our previous study on the *Methanosarcina mazei* class II DNA photolyase (*MmCPDII*)⁷³, we were able to structurally characterize FAD post-ET, redox-dependent changes in the nanosecond-to-millisecond range, and analyze how each intermediate species was stabilized via TR-SFX. Furthermore, our findings uncovered the structural mechanism of how DNA photolyases (*MmCPDII*) repair cyclobutane pyrimidine dimer (CPD) lesion at atomic and picosecond resolutions via TR-SFX (under revision). With these encouraging findings, we were able to uncover the detail mechanism and observe how a light-driven DNA repair enzyme displays its function, as a model system for structural dynamic enzymology.

Based on this, my main project in this thesis was the elucidation of the molecular mechanism how animal-like cryptochromes such as *CraCRY* utilize proton transfer events to act as radical pair sensors, and how (partial) protein unfolding underlies CRY signaling. Overall, these time-resolved structural data and their analysis rationalized the CRY's role in photoreception. Although my minor project on (6-4)PP repair by *CraCRY* was performed by *in crystallo* cryo-trapping techniques instead of TR-SFX, the post repair scheme of complex dissociation events was already able to capture three intermediate stages, i.e. (1) base relaxation within the active site, (2) base return towards the unpaired bubble and (3) DNA release from the (6-4)PP active site. Together, they are reminiscent of the analogous post-repair reactions of *MmCPDII* and demonstrate how enzyme and substrate dissociate from each other since the enzyme has performed its repair function. Finally, my second minor project is an extension of our previous study⁷³, as I found that a key mutation in *MmCPDII* causes an alternative photoreception behavior. Clearly, this study will be a candidate for TR-SFX as well to investigate how proton donation from the solvent is mediated by different types of photolyases/cryptochromes of the PCSf. Overall, this thesis shows time-resolved structural enzymology in light-driven enzymes, and sheds light on different strategies to capture enigmatic intermediates.

6. Reference

1. Ernst, O. P.; Lodowski, D. T.; Elstner, M.; Hegemann, P.; Brown, L. S.; Kandori, H., Microbial and Animal Rhodopsins: Structures, Functions, and Molecular Mechanisms. *Chemical Reviews* **2014**, *114* (1), 126-163.
2. Losi, A.; Gärtner, W., The evolution of flavin-binding photoreceptors: an ancient chromophore serving trendy blue-light sensors. *Annual review of plant biology* **2012**, *63*, 49-72.
3. van der Horst, M. A.; Hellingwerf, K. J., Photoreceptor proteins, "star actors of modern times": a review of the functional dynamics in the structure of representative members of six different photoreceptor families. *Accounts of chemical research* **2004**, *37* (1), 13-20.
4. Ahmad, M.; Cashmore, A. R., HY4 gene of *A. thaliana* encodes a protein with characteristics of a blue-light photoreceptor. *Nature* **1993**, *366* (6451), 162-166.
5. Wang, H., Signaling mechanisms of higher plant photoreceptors: a structure-function perspective. *Current topics in developmental biology* **2005**, *68*, 227-61.
6. Pedmale, U. V.; Huang, S. C.; Zander, M.; Cole, B. J.; Hetzel, J.; Ljung, K.; Reis, P. A. B.; Sridevi, P.; Nito, K.; Nery, J. R.; Ecker, J. R.; Chory, J., Cryptochromes Interact Directly with PIFs to Control Plant Growth in Limiting Blue Light. *Cell* **2016**, *164* (1-2), 233-245.
7. Ozturk, N.; Selby, C. P.; Annayev, Y.; Zhong, D.; Sancar, A., Reaction mechanism of *Drosophila* cryptochrome. *Proceedings of the National Academy of Sciences* **2011**, *108* (2), 516-521.
8. Ozturk, N.; Selby, C. P.; Zhong, D.; Sancar, A., Mechanism of photoreception by *Drosophila* cryptochrome: role of the redox status of the flavin chromophore. *The Journal of biological chemistry* **2014**, *289* (8), 4634-42.
9. Mitchell, D. L.; Nairn, R. S., The biology of the (6-4) photoproduct. *Photochemistry and photobiology* **1989**, *49* (6), 805-19.
10. Kavakli, I. H.; Baris, I.; Tardu, M.; Gül, Ş.; Öner, H.; Çal, S.; Bulut, S.; Yarpavvar, D.; Berkel, Ç.; Ustaoglu, P.; Aydın, C., The Photolyase/Cryptochrome Family of Proteins as DNA Repair Enzymes and Transcriptional Repressors. *Photochemistry and photobiology* **2017**, *93* (1), 93-103.
11. Maul, M. J.; Barends, T. R.; Glas, A. F.; Cryle, M. J.; Domratcheva, T.; Schneider, S.; Schlichting, I.; Carell, T., Crystal structure and mechanism of a DNA (6-4) photolyase. *Angewandte Chemie (International ed. in English)* **2008**, *47* (52), 10076-80.
12. Ozturk, N., Phylogenetic and Functional Classification of the Photolyase/Cryptochrome Family. *Photochemistry and photobiology* **2017**, *93* (1), 104-111.

13. Rivera, A. S.; Ozturk, N.; Fahey, B.; Plachetzki, D. C.; Degnan, B. M.; Sancar, A.; Oakley, T. H., Blue-light-receptive cryptochrome is expressed in a sponge eye lacking neurons and opsin. *The Journal of experimental biology* **2012**, *215* (Pt 8), 1278-86.
14. Oztürk, N.; Song, S. H.; Ozgür, S.; Selby, C. P.; Morrison, L.; Partch, C.; Zhong, D.; Sancar, A., Structure and function of animal cryptochromes. *Cold Spring Harbor symposia on quantitative biology* **2007**, *72*, 119-31.
15. Oztürk, N.; Kao, Y. T.; Selby, C. P.; Kavakli, I. H.; Partch, C. L.; Zhong, D.; Sancar, A., Purification and characterization of a type III photolyase from *Caulobacter crescentus*. *Biochemistry* **2008**, *47* (39), 10255-61.
16. Selby, C. P.; Sancar, A., A cryptochrome/photolyase class of enzymes with single-stranded DNA-specific photolyase activity. *Proceedings of the National Academy of Sciences of the United States of America* **2006**, *103* (47), 17696-700.
17. Sancar, A., Structure and function of photolyase and in vivo enzymology: 50th anniversary. *The Journal of biological chemistry* **2008**, *283* (47), 32153-7.
18. Emery, P.; So, W. V.; Kaneko, M.; Hall, J. C.; Rosbash, M., CRY, a *Drosophila* clock and light-regulated cryptochrome, is a major contributor to circadian rhythm resetting and photosensitivity. *Cell* **1998**, *95* (5), 669-79.
19. Lin, C.; Yang, H.; Guo, H.; Mockler, T.; Chen, J.; Cashmore, A. R., Enhancement of blue-light sensitivity of *Arabidopsis* seedlings by a blue light receptor cryptochrome 2. *Proceedings of the National Academy of Sciences of the United States of America* **1998**, *95* (5), 2686-90.
20. Ozgür, S.; Sancar, A., Analysis of autophosphorylating kinase activities of *Arabidopsis* and human cryptochromes. *Biochemistry* **2006**, *45* (44), 13369-74.
21. Müller, W. E.; Wendt, K.; Geppert, C.; Wiens, M.; Reiber, A.; Schröder, H. C., Novel photoreception system in sponges? Unique transmission properties of the stalk spicules from the hexactinellid *Hyalonemasieboldi*. *Biosensors & bioelectronics* **2006**, *21* (7), 1149-55.
22. Müller, W. E.; Wang, X.; Schröder, H. C.; Korzhev, M.; Grebenjuk, V. A.; Markl, J. S.; Jochum, K. P.; Pisignano, D.; Wiens, M., A cryptochrome-based photosensory system in the siliceous sponge *Suberites domuncula* (Demospongiae). *The FEBS journal* **2010**, *277* (5), 1182-201.
23. Müller, W. E. G.; Schröder, H. C.; Markl, J. S.; Grebenjuk, V. A.; Korzhev, M.; Steffen, R.; Wang, X., Cryptochrome in Sponges: A Key Molecule Linking Photoreception with Phototransduction. *Journal of Histochemistry & Cytochemistry* **2013**, *61* (11), 814-832.
24. Le, S. Q.; Gascuel, O., An improved general amino acid replacement matrix. *Molecular biology and evolution* **2008**, *25* (7), 1307-20.
25. Park, H. W.; Kim, S. T.; Sancar, A.; Deisenhofer, J., Crystal structure of DNA

- photolyase from *Escherichia coli*. *Science (New York, N.Y.)* **1995**, 268 (5219), 1866-72.
26. Tamada, T.; Kitadokoro, K.; Higuchi, Y.; Inaka, K.; Yasui, A.; de Ruiter, P. E.; Eker, A. P.; Miki, K., Crystal structure of DNA photolyase from *Anacystis nidulans*. *Nature structural biology* **1997**, 4 (11), 887-91.
 27. Chaves, I.; Pokorny, R.; Byrdin, M.; Hoang, N.; Ritz, T.; Brettel, K.; Essen, L. O.; van der Horst, G. T.; Batschauer, A.; Ahmad, M., The cryptochromes: blue light photoreceptors in plants and animals. *Annual review of plant biology* **2011**, 62, 335-64.
 28. Kiontke, S.; Gnau, P.; Haselsberger, R.; Batschauer, A.; Essen, L. O., Structural and evolutionary aspects of antenna chromophore usage by class II photolyases. *The Journal of biological chemistry* **2014**, 289 (28), 19659-69.
 29. Klar, T.; Pokorny, R.; Moldt, J.; Batschauer, A.; Essen, L. O., Cryptochrome 3 from *Arabidopsis thaliana*: structural and functional analysis of its complex with a folate light antenna. *Journal of molecular biology* **2007**, 366 (3), 954-64.
 30. Klar, T.; Kaiser, G.; Hennecke, U.; Carell, T.; Batschauer, A.; Essen, L. O., Natural and non-natural antenna chromophores in the DNA photolyase from *Thermus thermophilus*. *Chembiochem : a European journal of chemical biology* **2006**, 7 (11), 1798-806.
 31. Zhang, F.; Scheerer, P.; Oberpichler, I.; Lamparter, T.; Krauß, N., Crystal structure of a prokaryotic (6-4) photolyase with an Fe-S cluster and a 6,7-dimethyl-8-ribityllumazine antenna chromophore. *Proceedings of the National Academy of Sciences of the United States of America* **2013**, 110 (18), 7217-22.
 32. Fujihashi, M.; Numoto, N.; Kobayashi, Y.; Mizushima, A.; Tsujimura, M.; Nakamura, A.; Kowabayasi, Y.; Miki, K., Crystal structure of archaeal photolyase from *Sulfolobus tokodaii* with two FAD molecules: implication of a novel light-harvesting cofactor. *Journal of molecular biology* **2007**, 365 (4), 903-10.
 33. Partch, C. L.; Clarkson, M. W.; Ozgür, S.; Lee, A. L.; Sancar, A., Role of structural plasticity in signal transduction by the cryptochrome blue-light photoreceptor. *Biochemistry* **2005**, 44 (10), 3795-805.
 34. Yang, H. Q.; Wu, Y. J.; Tang, R. H.; Liu, D.; Liu, Y.; Cashmore, A. R., The C termini of *Arabidopsis* cryptochromes mediate a constitutive light response. *Cell* **2000**, 103 (5), 815-27.
 35. Wang, H.; Ma, L. G.; Li, J. M.; Zhao, H. Y.; Deng, X. W., Direct interaction of *Arabidopsis* cryptochromes with COP1 in light control development. *Science (New York, N.Y.)* **2001**, 294 (5540), 154-8.
 36. Ceriani, M. F.; Darlington, T. K.; Staknis, D.; Más, P.; Petti, A. A.; Weitz, C. J.; Kay, S. A., Light-dependent sequestration of TIMELESS by CRYPTOCHROME. *Science (New York, N.Y.)* **1999**, 285 (5427), 553-6.
 37. Dissel, S.; Codd, V.; Fedic, R.; Garner, K. J.; Costa, R.; Kyriacou, C. P.; Rosato,

- E., A constitutively active cryptochrome in *Drosophila melanogaster*. *Nature neuroscience* **2004**, 7 (8), 834-40.
38. Busza, A.; Emery-Le, M.; Rosbash, M.; Emery, P., Roles of the two *Drosophila* CRYPTOCHROME structural domains in circadian photoreception. *Science (New York, N.Y.)* **2004**, 304 (5676), 1503-6.
 39. van der Schalie, E. A.; Conte, F. E.; Marz, K. E.; Green, C. B., Structure/function analysis of *Xenopus* cryptochromes 1 and 2 reveals differential nuclear localization mechanisms and functional domains important for interaction with and repression of CLOCK-BMAL1. *Molecular and cellular biology* **2007**, 27 (6), 2120-9.
 40. Chaves, I.; Yagita, K.; Barnhoorn, S.; Okamura, H.; van der Horst, G. T.; Tamanini, F., Functional evolution of the photolyase/cryptochrome protein family: importance of the C terminus of mammalian CRY1 for circadian core oscillator performance. *Molecular and cellular biology* **2006**, 26 (5), 1743-53.
 41. Gao, P.; Yoo, S. H.; Lee, K. J.; Rosensweig, C.; Takahashi, J. S.; Chen, B. P.; Green, C. B., Phosphorylation of the cryptochrome 1 C-terminal tail regulates circadian period length. *The Journal of biological chemistry* **2013**, 288 (49), 35277-86.
 42. Harada, Y.; Sakai, M.; Kurabayashi, N.; Hirota, T.; Fukada, Y., Ser-557-phosphorylated mCRY2 is degraded upon synergistic phosphorylation by glycogen synthase kinase-3 beta. *The Journal of biological chemistry* **2005**, 280 (36), 31714-21.
 43. Kao, Y. T.; Tan, C.; Song, S. H.; Oztürk, N.; Li, J.; Wang, L.; Sancar, A.; Zhong, D., Ultrafast dynamics and anionic active states of the flavin cofactor in cryptochrome and photolyase. *Journal of the American Chemical Society* **2008**, 130 (24), 7695-701.
 44. Liu, B.; Liu, H.; Zhong, D.; Lin, C., Searching for a photocycle of the cryptochrome photoreceptors. *Current opinion in plant biology* **2010**, 13 (5), 578-86.
 45. Kim, S. T.; Sancar, A.; Essenmacher, C.; Babcock, G. T., Time-resolved EPR studies with DNA photolyase: excited-state FADH0 abstracts an electron from Trp-306 to generate FADH-, the catalytically active form of the cofactor. *Proceedings of the National Academy of Sciences of the United States of America* **1993**, 90 (17), 8023-7.
 46. Kavakli, I. H.; Sancar, A., Analysis of the role of intraprotein electron transfer in photoreactivation by DNA photolyase in vivo. *Biochemistry* **2004**, 43 (48), 15103-10.
 47. Essen, L. O., Photolyases and cryptochromes: common mechanisms of DNA repair and light-driven signaling? *Current opinion in structural biology* **2006**, 16 (1), 51-9.
 48. Sancar, G. B.; Sancar, A., Purification and characterization of DNA photolyases. *Methods in enzymology* **2006**, 408, 121-56.
 49. Kottke, T.; Batschauer, A.; Ahmad, M.; Heberle, J., Blue-Light-Induced Changes in Arabidopsis Cryptochrome 1 Probed by FTIR Difference Spectroscopy. *Biochemistry* **2006**, 45 (8), 2472-2479.

50. Lin, C.; Robertson, D. E.; Ahmad, M.; Raibekas, A. A.; Jorns, M. S.; Dutton, P. L.; Cashmore, A. R., Association of flavin adenine dinucleotide with the Arabidopsis blue light receptor CRY1. *Science (New York, N.Y.)* **1995**, 269 (5226), 968-70.
51. Ahmad, M.; Grancher, N.; Heil, M.; Black, R. C.; Giovani, B.; Galland, P.; Lardemer, D., Action spectrum for cryptochrome-dependent hypocotyl growth inhibition in Arabidopsis. *Plant physiology* **2002**, 129 (2), 774-85.
52. Zeugner, A.; Byrdin, M.; Bouly, J. P.; Bakrim, N.; Giovani, B.; Brettel, K.; Ahmad, M., Light-induced electron transfer in Arabidopsis cryptochrome-1 correlates with in vivo function. *The Journal of biological chemistry* **2005**, 280 (20), 19437-40.
53. Banerjee, R.; Schleicher, E.; Meier, S.; Viana, R. M.; Pokorny, R.; Ahmad, M.; Bittl, R.; Batschauer, A., The signaling state of Arabidopsis cryptochrome 2 contains flavin semiquinone. *The Journal of biological chemistry* **2007**, 282 (20), 14916-22.
54. Bouly, J. P.; Schleicher, E.; Dionisio-Sese, M.; Vandenbussche, F.; Van Der Straeten, D.; Bakrim, N.; Meier, S.; Batschauer, A.; Galland, P.; Bittl, R.; Ahmad, M., Cryptochrome blue light photoreceptors are activated through interconversion of flavin redox states. *The Journal of biological chemistry* **2007**, 282 (13), 9383-9391.
55. Shirdel, J.; Zirak, P.; Penzkofer, A.; Breitzkreuz, H.; Wolf, E., Absorption and fluorescence spectroscopic characterisation of the circadian blue-light photoreceptor cryptochrome from *Drosophila melanogaster* (dCry). *Chemical Physics* **2008**, 352 (1), 35-47.
56. Berndt, A.; Kottke, T.; Breitzkreuz, H.; Dvorsky, R.; Hennig, S.; Alexander, M.; Wolf, E., A Novel Photoreaction Mechanism for the Circadian Blue Light Photoreceptor *Drosophila* Cryptochrome*. *Journal of Biological Chemistry* **2007**, 282 (17), 13011-13021.
57. Liedvogel, M.; Maeda, K.; Henbest, K.; Schleicher, E.; Simon, T.; Timmel, C. R.; Hore, P. J.; Mouritsen, H., Chemical magnetoreception: bird cryptochrome 1a is excited by blue light and forms long-lived radical-pairs. *PloS one* **2007**, 2 (10), e1106.
58. Hoang, N.; Schleicher, E.; Kacprzak, S.; Bouly, J.-P.; Picot, M.; Wu, W.; Berndt, A.; Wolf, E.; Bittl, R.; Ahmad, M., Human and *Drosophila* Cryptochromes Are Light Activated by Flavin Photoreduction in Living Cells. *PLOS Biology* **2008**, 6 (7), e160.
59. Song, S.-H.; Öztürk, N.; Denaro, T. R.; Arat, N. Ö.; Kao, Y.-T.; Zhu, H.; Zhong, D.; Reppert, S. M.; Sancar, A., Formation and Function of Flavin Anion Radical in Cryptochrome 1 Blue-Light Photoreceptor of Monarch Butterfly*. *Journal of Biological Chemistry* **2007**, 282 (24), 17608-17612.
60. Aubert, C.; Vos, M. H.; Mathis, P.; Eker, A. P.; Brettel, K., Intraprotein radical transfer during photoactivation of DNA photolyase. *Nature* **2000**, 405 (6786), 586-90.
61. Li, Y. F.; Heelis, P. F.; Sancar, A., Active site of DNA photolyase: tryptophan-306 is the intrinsic hydrogen atom donor essential for flavin radical photoreduction and

DNA repair in vitro. *Biochemistry* **1991**, *30* (25), 6322-6329.

62. Henbest, K. B.; Maeda, K.; Hore, P. J.; Joshi, M.; Bacher, A.; Bittl, R.; Weber, S.; Timmel, C. R.; Schleicher, E., Magnetic-field effect on the photoactivation reaction of Escherichia coli DNA photolyase. *Proceedings of the National Academy of Sciences* **2008**, *105* (38), 14395-14399.
63. Giovani, B.; Byrdin, M.; Ahmad, M.; Brettel, K., Light-induced electron transfer in a cryptochrome blue-light photoreceptor. *Nature structural biology* **2003**, *10* (6), 489-90.
64. Liu, Z.; Tan, C.; Guo, X.; Li, J.; Wang, L.; Sancar, A.; Zhong, D., Determining complete electron flow in the cofactor photoreduction of oxidized photolyase. *Proceedings of the National Academy of Sciences* **2013**, *110* (32), 12966-12971.
65. Brettel, K.; Byrdin, M., Reaction mechanisms of DNA photolyase. *Current opinion in structural biology* **2010**, *20* (6), 693-701.
66. Müller, P.; Yamamoto, J.; Martin, R.; Iwai, S.; Brettel, K., Discovery and functional analysis of a 4th electron-transferring tryptophan conserved exclusively in animal cryptochromes and (6-4) photolyases. *Chemical Communications* **2015**, *51* (85), 15502-15505.
67. Nohr, D.; Franz, S.; Rodriguez, R.; Paulus, B.; Essen, L. O.; Weber, S.; Schleicher, E., Extended Electron-Transfer in Animal Cryptochromes Mediated by a Tetrad of Aromatic Amino Acids. *Biophysical journal* **2016**, *111* (2), 301-311.
68. Zhao, X.; Liu, J.; Hsu, D. S.; Zhao, S.; Taylor, J. S.; Sancar, A., Reaction mechanism of (6-4) photolyase. *The Journal of biological chemistry* **1997**, *272* (51), 32580-90.
69. Zhang, M.; Wang, L.; Zhong, D., Photolyase: Dynamics and electron-transfer mechanisms of DNA repair. *Archives of biochemistry and biophysics* **2017**, *632*, 158-174.
70. Nakai, S.; Yoneda, F.; Yamabe, T., Theoretical study on the lowest-frequency mode of the flavin ring. *Theoretical Chemistry Accounts* **1999**, *103* (2), 109-116.
71. Fox, K. M.; Karplus, P. A., Old yellow enzyme at 2 Å resolution: overall structure, ligand binding, and comparison with related flavoproteins. *Structure (London, England : 1993)* **1994**, *2* (11), 1089-105.
72. Lennon, B. W.; Williams, C. H., Jr.; Ludwig, M. L., Crystal structure of reduced thioredoxin reductase from Escherichia coli: structural flexibility in the isoalloxazine ring of the flavin adenine dinucleotide cofactor. *Protein science : a publication of the Protein Society* **1999**, *8* (11), 2366-79.
73. Maestre-Reyna, M.; Yang, C.-H.; Nango, E.; Huang, W.-C.; Ngurah Putu, E. P. G.; Wu, W.-J.; Wang, P.-H.; Franz-Badur, S.; Saft, M.; Emmerich, H.-J.; Wu, H.-Y.; Lee, C.-C.; Huang, K.-F.; Chang, Y.-K.; Liao, J.-H.; Weng, J.-H.; Gad, W.; Chang, C.-W.;

- Pang, A. H.; Sugahara, M.; Owada, S.; Hosokawa, Y.; Joti, Y.; Yamashita, A.; Tanaka, R.; Tanaka, T.; Luo, F.; Tono, K.; Hsu, K.-C.; Kiontke, S.; Schapiro, I.; Spadaccini, R.; Royant, A.; Yamamoto, J.; Iwata, S.; Essen, L.-O.; Bessho, Y.; Tsai, M.-D., Serial crystallography captures dynamic control of sequential electron and proton transfer events in a flavoenzyme. *Nature Chemistry* **2022**, *14* (6), 677-685.
74. Liu, Z.; Tan, C.; Guo, X.; Kao, Y. T.; Li, J.; Wang, L.; Sancar, A.; Zhong, D., Dynamics and mechanism of cyclobutane pyrimidine dimer repair by DNA photolyase. *Proceedings of the National Academy of Sciences of the United States of America* **2011**, *108* (36), 14831-6.
75. Zhong, D., Electron transfer mechanisms of DNA repair by photolyase. *Annual review of physical chemistry* **2015**, *66*, 691-715.
76. Kavakli, I. H.; Ozturk, N.; Gul, S., DNA repair by photolyases. *Advances in protein chemistry and structural biology* **2019**, *115*, 1-19.
77. Tan, C.; Liu, Z.; Li, J.; Guo, X.; Wang, L.; Sancar, A.; Zhong, D., The molecular origin of high DNA-repair efficiency by photolyase. *Nature Communications* **2015**, *6* (1), 7302.
78. Kao, Y. T.; Saxena, C.; Wang, L.; Sancar, A.; Zhong, D., Direct observation of thymine dimer repair in DNA by photolyase. *Proceedings of the National Academy of Sciences of the United States of America* **2005**, *102* (45), 16128-32.
79. Thiagarajan, V.; Byrdin, M.; Eker, A. P.; Müller, P.; Brettel, K., Kinetics of cyclobutane thymine dimer splitting by DNA photolyase directly monitored in the UV. *Proceedings of the National Academy of Sciences of the United States of America* **2011**, *108* (23), 9402-7.
80. Espagne, A.; Byrdin, M.; Eker, A. P.; Brettel, K., Very fast product release and catalytic turnover of DNA photolyase. *ChemBiochem : a European journal of chemical biology* **2009**, *10* (11), 1777-80.
81. Zhang, M.; Wang, L.; Zhong, D., Photolyase: Dynamics and Mechanisms of Repair of Sun-Induced DNA Damage. *Photochemistry and photobiology* **2017**, *93* (1), 78-92.
82. Kim, S. T.; Malhotra, K.; Smith, C. A.; Taylor, J. S.; Sancar, A., Characterization of (6-4) photoproduct DNA photolyase. *Journal of Biological Chemistry* **1994**, *269* (11), 8535-8540.
83. Hitomi, K.; Kim, S. T.; Iwai, S.; Harima, N.; Otoshi, E.; Ikenaga, M.; Todo, T., Binding and catalytic properties of Xenopus (6-4) photolyase. *The Journal of biological chemistry* **1997**, *272* (51), 32591-8.
84. Hitomi, K.; Nakamura, H.; Kim, S.-T.; Mizukoshi, T.; Ishikawa, T.; Iwai, S.; Todo, T., Role of Two Histidines in the (6-4) Photolyase Reaction*. *Journal of Biological Chemistry* **2001**, *276* (13), 10103-10109.

85. Faraji, S.; Dreuw, A., Proton-Transfer-Steered Mechanism of Photolesion Repair by (6–4)-Photolyases. *The Journal of Physical Chemistry Letters* **2012**, 3 (2), 227-230.
86. Yamamoto, J.; Martin, R.; Iwai, S.; Plaza, P.; Brettel, K., Repair of the (6-4) photoproduct by DNA photolyase requires two photons. *Angewandte Chemie (International ed. in English)* **2013**, 52 (29), 7432-6.
87. Sadeghian, K.; Bocola, M.; Merz, T.; Schütz, M., Theoretical Study on the Repair Mechanism of the (6–4) Photolesion by the (6–4) Photolyase. *Journal of the American Chemical Society* **2010**, 132 (45), 16285-16295.
88. Yamamoto, J.; Plaza, P.; Brettel, K., Repair of (6-4) Lesions in DNA by (6-4) Photolyase: 20 Years of Quest for the Photoreaction Mechanism. *Photochemistry and photobiology* **2017**, 93 (1), 51-66.
89. Domratcheva, T., Neutral Histidine and Photoinduced Electron Transfer in DNA Photolyases. *Journal of the American Chemical Society* **2011**, 133 (45), 18172-18182.
90. Faraji, S.; Groenhof, G.; Dreuw, A., Combined QM/MM Investigation on the Light-Driven Electron-Induced Repair of the (6–4) Thymine Dimer Catalyzed by DNA Photolyase. *The Journal of Physical Chemistry B* **2013**, 117 (35), 10071-10079.
91. Faraji, S.; Zhong, D.; Dreuw, A., Characterization of the Intermediate in and Identification of the Repair Mechanism of (6-4) Photolesions by Photolyases. *Angewandte Chemie (International ed. in English)* **2016**, 55 (17), 5175-8.
92. Li, J.; Liu, Z.; Tan, C.; Guo, X.; Wang, L.; Sancar, A.; Zhong, D., Dynamics and mechanism of repair of ultraviolet-induced (6-4) photoproduct by photolyase. *Nature* **2010**, 466 (7308), 887-890.
93. Domratcheva, T.; Schlichting, I., Electronic Structure of (6–4) DNA Photoproduct Repair Involving a Non-Oxetane Pathway. *Journal of the American Chemical Society* **2009**, 131 (49), 17793-17799.
94. Emma, P.; Akre, R.; Arthur, J.; Bionta, R.; Bostedt, C.; Bozek, J.; Brachmann, A.; Bucksbaum, P.; Coffee, R.; Decker, F. J.; Ding, Y.; Dowell, D.; Edstrom, S.; Fisher, A.; Frisch, J.; Gilevich, S.; Hastings, J.; Hays, G.; Hering, P.; Huang, Z.; Iverson, R.; Loos, H.; Messerschmidt, M.; Miahnahri, A.; Moeller, S.; Nuhn, H. D.; Pile, G.; Ratner, D.; Rzepiela, J.; Schultz, D.; Smith, T.; Stefan, P.; Tompkins, H.; Turner, J.; Welch, J.; White, W.; Wu, J.; Yocky, G.; Galayda, J., First lasing and operation of an ångstrom-wavelength free-electron laser. *Nature Photonics* **2010**, 4 (9), 641-647.
95. Ishikawa, T.; Aoyagi, H.; Asaka, T.; Asano, Y.; Azumi, N.; Bizen, T.; Ego, H.; Fukami, K.; Fukui, T.; Furukawa, Y.; Goto, S.; Hanaki, H.; Hara, T.; Hasegawa, T.; Hatsui, T.; Higashiya, A.; Hirono, T.; Hosoda, N.; Ishii, M.; Inagaki, T.; Inubushi, Y.; Itoga, T.; Joti, Y.; Kago, M.; Kameshima, T.; Kimura, H.; Kirihaara, Y.; Kiyomichi, A.; Kobayashi, T.; Kondo, C.; Kudo, T.; Maesaka, H.; Maréchal, X. M.; Masuda, T.; Matsubara, S.; Matsumoto, T.; Matsushita, T.; Matsui, S.; Nagasono, M.; Nariyama, N.;

Ohashi, H.; Ohata, T.; Ohshima, T.; Ono, S.; Otake, Y.; Saji, C.; Sakurai, T.; Sato, T.; Sawada, K.; Seike, T.; Shirasawa, K.; Sugimoto, T.; Suzuki, S.; Takahashi, S.; Takebe, H.; Takeshita, K.; Tamasaku, K.; Tanaka, H.; Tanaka, R.; Tanaka, T.; Togashi, T.; Togawa, K.; Tokuhisa, A.; Tomizawa, H.; Tono, K.; Wu, S.; Yabashi, M.; Yamaga, M.; Yamashita, A.; Yanagida, K.; Zhang, C.; Shintake, T.; Kitamura, H.; Kumagai, N., A compact X-ray free-electron laser emitting in the sub-ångström region. *Nature Photonics* **2012**, 6 (8), 540-544.

96. Pellegrini, C.; Marinelli, A.; Reiche, S., The physics of x-ray free-electron lasers. *Reviews of Modern Physics* **2016**, 88 (1), 015006.

97. Milton, S. V.; Gluskin, E.; Arnold, N. D.; Benson, C.; Berg, W.; Biedron, S. G.; Borland, M.; Chae, Y.-C.; Dejus, R. J.; Den Hartog, P. K.; Deriy, B.; Erdmann, M.; Eidelman, Y. I.; Hahne, M. W.; Huang, Z.; Kim, K.-J.; Lewellen, J. W.; Li, Y.; Lumpkin, A. H.; Makarov, O.; Moog, E. R.; Nassiri, A.; Sajaev, V.; Soliday, R.; Tieman, B. J.; Trakhtenberg, E. M.; Travish, G.; Vasserman, I. B.; Vinokurov, N. A.; Wang, X. J.; Wiemerslage, G.; Yang, B. X., Exponential Gain and Saturation of a Self-Amplified Spontaneous Emission Free-Electron Laser. *Science (New York, N.Y.)* **2001**, 292 (5524), 2037-2041.

98. Yabashi, M.; Tanaka, H.; Ishikawa, T., Overview of the SACLA facility. *Journal of synchrotron radiation* **2015**, 22 (3), 477-84.

99. Neutze, R.; Wouts, R.; van der Spoel, D.; Weckert, E.; Hajdu, J., Potential for biomolecular imaging with femtosecond X-ray pulses. *Nature* **2000**, 406 (6797), 752-757.

100. Spence, J. C.; Weierstall, U.; Chapman, H. N., X-ray lasers for structural and dynamic biology. *Reports on progress in physics. Physical Society (Great Britain)* **2012**, 75 (10), 102601.

101. Neutze, R.; Moffat, K., Time-resolved structural studies at synchrotrons and X-ray free electron lasers: opportunities and challenges. *Current opinion in structural biology* **2012**, 22 (5), 651-9.

102. Tenboer, J.; Basu, S.; Zatsepin, N.; Pande, K.; Milathianaki, D.; Frank, M.; Hunter, M.; Boutet, S.; Williams, G. J.; Koglin, J. E.; Oberthuer, D.; Heymann, M.; Kupitz, C.; Conrad, C.; Coe, J.; Roy-Chowdhury, S.; Weierstall, U.; James, D.; Wang, D.; Grant, T.; Barty, A.; Yefanov, O.; Scales, J.; Gati, C.; Seuring, C.; Srajer, V.; Henning, R.; Schwander, P.; Fromme, R.; Ourmazd, A.; Moffat, K.; Van Thor, J. J.; Spence, J. C. H.; Fromme, P.; Chapman, H. N.; Schmidt, M., Time-resolved serial crystallography captures high-resolution intermediates of photoactive yellow protein. *Science (New York, N.Y.)* **2014**, 346 (6214), 1242-1246.

103. Schmidt, M., Mix and Inject: Reaction Initiation by Diffusion for Time-Resolved Macromolecular Crystallography. *Advances in Condensed Matter Physics* **2013**, 2013,

167276.

104. Weierstall, U.; James, D.; Wang, C.; White, T. A.; Wang, D.; Liu, W.; Spence, J. C. H.; Bruce Doak, R.; Nelson, G.; Fromme, P.; Fromme, R.; Grotjohann, I.; Kupitz, C.; Zatsepin, N. A.; Liu, H.; Basu, S.; Wacker, D.; Won Han, G.; Katritch, V.; Boutet, S.; Messerschmidt, M.; Williams, G. J.; Koglin, J. E.; Marvin Seibert, M.; Klinker, M.; Gati, C.; Shoeman, R. L.; Barty, A.; Chapman, H. N.; Kirian, R. A.; Beyerlein, K. R.; Stevens, R. C.; Li, D.; Shah, S. T. A.; Howe, N.; Caffrey, M.; Cherezov, V., Lipidic cubic phase injector facilitates membrane protein serial femtosecond crystallography. *Nature Communications* **2014**, *5* (1), 3309.

105. Sugahara, M.; Mizohata, E.; Nango, E.; Suzuki, M.; Tanaka, T.; Masuda, T.; Tanaka, R.; Shimamura, T.; Tanaka, Y.; Suno, C.; Ihara, K.; Pan, D.; Kakinouchi, K.; Sugiyama, S.; Murata, M.; Inoue, T.; Tono, K.; Song, C.; Park, J.; Kameshima, T.; Hatsui, T.; Joti, Y.; Yabashi, M.; Iwata, S., Grease matrix as a versatile carrier of proteins for serial crystallography. *Nature Methods* **2015**, *12* (1), 61-63.

106. Botha, S.; Nass, K.; Barends, T. R.; Kabsch, W.; Latz, B.; Dworkowski, F.; Foucar, L.; Panepucci, E.; Wang, M.; Shoeman, R. L.; Schlichting, I.; Doak, R. B., Room-temperature serial crystallography at synchrotron X-ray sources using slowly flowing free-standing high-viscosity microstreams. *Acta crystallographica. Section D, Biological crystallography* **2015**, *71* (Pt 2), 387-97.

107. Sugahara, M.; Nakane, T.; Masuda, T.; Suzuki, M.; Inoue, S.; Song, C.; Tanaka, R.; Nakatsu, T.; Mizohata, E.; Yumoto, F.; Tono, K.; Joti, Y.; Kameshima, T.; Hatsui, T.; Yabashi, M.; Nureki, O.; Numata, K.; Nango, E.; Iwata, S., Hydroxyethyl cellulose matrix applied to serial crystallography. *Scientific Reports* **2017**, *7* (1), 703.

108. Sugahara, M.; Song, C.; Suzuki, M.; Masuda, T.; Inoue, S.; Nakane, T.; Yumoto, F.; Nango, E.; Tanaka, R.; Tono, K.; Joti, Y.; Kameshima, T.; Hatsui, T.; Yabashi, M.; Nureki, O.; Numata, K.; Iwata, S., Oil-free hyaluronic acid matrix for serial femtosecond crystallography. *Scientific Reports* **2016**, *6* (1), 24484.

109. Lacombat, F.; Espagne, A.; Dozova, N.; Plaza, P.; Müller, P.; Brettel, K.; Franz-Badur, S.; Essen, L.-O., Ultrafast Oxidation of a Tyrosine by Proton-Coupled Electron Transfer Promotes Light Activation of an Animal-like Cryptochrome. *Journal of the American Chemical Society* **2019**, *141* (34), 13394-13409.

110. Oldemeyer, S.; Franz, S.; Wenzel, S.; Essen, L.-O.; Mittag, M.; Kottke, T., Essential Role of an Unusually Long-lived Tyrosyl Radical in the Response to Red Light of the Animal-like Cryptochrome aCRY. *Journal of Biological Chemistry* **2016**, *291* (27), 14062-14071.

111. Franz, S.; Ignatz, E.; Wenzel, S.; Zielosko, H.; Putu, E.; Maestre-Reyna, M.; Tsai, M. D.; Yamamoto, J.; Mittag, M.; Essen, L. O., Structure of the bifunctional cryptochrome aCRY from *Chlamydomonas reinhardtii*. *Nucleic acids research* **2018**,

46 (15), 8010-8022.

112. Franz-Badur, S.; Penner, A.; Straß, S.; von Horsten, S.; Linne, U.; Essen, L.-O., Structural changes within the bifunctional cryptochrome/photolyase CraCRY upon blue light excitation. *Scientific Reports* **2019**, 9 (1), 9896.

113. Beel, B.; Müller, N.; Kottke, T.; Mittag, M., News about cryptochrome photoreceptors in algae. *Plant signaling & behavior* **2013**, 8 (2), e22870.

114. Stura, E. A.; Wilson, I. A., Applications of the streak seeding technique in protein crystallization. *Journal of Crystal Growth* **1991**, 110 (1), 270-282.

115. Tono, K.; Nango, E.; Sugahara, M.; Song, C.; Park, J.; Tanaka, T.; Tanaka, R.; Joti, Y.; Kameshima, T.; Ono, S.; Hatsui, T.; Mizohata, E.; Suzuki, M.; Shimamura, T.; Tanaka, Y.; Iwata, S.; Yabashi, M., Diverse application platform for hard X-ray diffraction in SACLA (DAPHNIS): application to serial protein crystallography using an X-ray free-electron laser. *Journal of synchrotron radiation* **2015**, 22 (3), 532-7.

116. Kameshima, T.; Ono, S.; Kudo, T.; Ozaki, K.; Kirihaara, Y.; Kobayashi, K.; Inubushi, Y.; Yabashi, M.; Horigome, T.; Holland, A.; Holland, K.; Burt, D.; Murao, H.; Hatsui, T., Development of an X-ray pixel detector with multi-port charge-coupled device for X-ray free-electron laser experiments. *The Review of scientific instruments* **2014**, 85 (3), 033110.

117. Barty, A.; Kirian, R. A.; Maia, F. R.; Hantke, M.; Yoon, C. H.; White, T. A.; Chapman, H., Cheetah: software for high-throughput reduction and analysis of serial femtosecond X-ray diffraction data. *J Appl Crystallogr* **2014**, 47 (Pt 3), 1118-1131.

118. White, T. A.; Kirian, R. A.; Martin, A. V.; Aquila, A.; Nass, K.; Barty, A.; Chapman, H. N., CrystFEL: a software suite for snapshot serial crystallography. *Journal of Applied Crystallography* **2012**, 45 (2), 335-341.

119. White, T., Processing serial crystallography data with CrystFEL: a step-by-step guide. *Acta Crystallographica Section D* **2019**, 75 (2), 219-233.

120. Winn, M. D.; Ballard, C. C.; Cowtan, K. D.; Dodson, E. J.; Emsley, P.; Evans, P. R.; Keegan, R. M.; Krissinel, E. B.; Leslie, A. G.; McCoy, A.; McNicholas, S. J.; Murshudov, G. N.; Pannu, N. S.; Potterton, E. A.; Powell, H. R.; Read, R. J.; Vagin, A.; Wilson, K. S., Overview of the CCP4 suite and current developments. *Acta crystallographica. Section D, Biological crystallography* **2011**, 67 (Pt 4), 235-42.

121. Schmidt, M., Time-Resolved Macromolecular Crystallography at Pulsed X-ray Sources. *International journal of molecular sciences* **2019**, 20 (6).

122. Howell, P. L.; Smith, G. D., Identification of heavy-atom derivatives by normal probability methods. *Journal of Applied Crystallography* **1992**, 25 (1), 81-86.

123. Emsley, P.; Lohkamp, B.; Scott, W. G.; Cowtan, K., Features and development of Coot. *Acta crystallographica. Section D, Biological crystallography* **2010**, 66 (Pt 4), 486-501.

124. Rould, M. A.; Carter, C. W., Isomorphous Difference Methods. In *Methods in enzymology*, Academic Press: 2003; Vol. 374, pp 145-163.
125. Yamashita, K.; Hirata, K.; Yamamoto, M., KAMO: towards automated data processing for microcrystals. *Acta crystallographica. Section D, Structural biology* **2018**, 74 (Pt 5), 441-449.
126. Kabsch, W., Automatic processing of rotation diffraction data from crystals of initially unknown symmetry and cell constants. *Journal of Applied Crystallography* **1993**, 26 (6), 795-800.
127. von Stetten, D.; Giraud, T.; Carpentier, P.; Sever, F.; Terrien, M.; Dobias, F.; Juers, D. H.; Flot, D.; Mueller-Dieckmann, C.; Leonard, G. A.; de Sanctis, D.; Royant, A., In crystallo optical spectroscopy (icOS) as a complementary tool on the macromolecular crystallography beamlines of the ESRF. *Acta crystallographica. Section D, Biological crystallography* **2015**, 71 (Pt 1), 15-26.
128. Beel, B.; Prager, K.; Spexard, M.; Sasso, S.; Weiss, D.; Müller, N.; Heinrickel, M.; Dewez, D.; Ikoma, D.; Grossman, A. R.; Kottke, T.; Mittag, M., A flavin binding cryptochrome photoreceptor responds to both blue and red light in *Chlamydomonas reinhardtii*. *The Plant cell* **2012**, 24 (7), 2992-3008.
129. Ludwig, M. L.; Schopfer, L. M.; Metzger, A. L.; Patridge, K. A.; Massey, V., Structure and oxidation-reduction behavior of 1-deaza-FMN flavodoxins: modulation of redox potentials in flavodoxins. *Biochemistry* **1990**, 29 (45), 10364-75.
130. Balland, V.; Byrdin, M.; Eker, A. P. M.; Ahmad, M.; Brettel, K., What Makes the Difference between a Cryptochrome and DNA Photolyase? A Spectroelectrochemical Comparison of the Flavin Redox Transitions. *Journal of the American Chemical Society* **2009**, 131 (2), 426-427.
131. Ritz, T.; Adem, S.; Schulten, K., A model for photoreceptor-based magnetoreception in birds. *Biophysical journal* **2000**, 78 (2), 707-18.
132. Günther, A.; Einwich, A.; Sjulstok, E.; Feederle, R.; Bolte, P.; Koch, K. W.; Solov'yov, I. A.; Mouritsen, H., Double-Cone Localization and Seasonal Expression Pattern Suggest a Role in Magnetoreception for European Robin Cryptochrome 4. *Current biology : CB* **2018**, 28 (2), 211-223.e4.
133. Prat, E.; Abela, R.; Aiba, M.; Alarcon, A.; Alex, J.; Arbelo, Y.; Arrell, C. A.; Arsov, V. R.; Bacellar, C.; Beard, C.; Beaud, P.; Bettoni, S.; Biffiger, R.; Bopp, M.; Braun, H. H.; Calvi, M.; Cassar, A.; Celcer, T.; Chergui, M.; Chevtsov, P.; Cirelli, C.; Citterio, A.; Craievich, P.; Divall, M. C.; Dax, A. J.; Dehler, M.; Deng, Y.; Dietrich, A.; Dijkstal, P.; Dinapoli, R.; Dordevic, S.; Ebner, S. G.; Engeler, D.; Erny, C.; Esposito, V. J.; Ferrari, E.; Flechsig, U.; Follath, R.; Frei, F.; Ganter, R.; Garvey, T.; Geng, Z.; Gobbo, A.; Gough, C.; Hauff, A.; Hauri, C. P.; Hiller, N.; Hunziker, S. G.; Huppert, M.; Ingold, G.; Ischebeck, R.; Janousch, M.; Johnson, P. J. M.; Johnson, S. L.; Juranić, P. N.; Jurcevic,

- M.; Kaiser, M.; Kalt, R.; Keil, B.; Kiselev, D.; Kittel, C.; Knopp, G.; Koprek, W.; Laznovsky, M.; Lemke, H. T.; Sancho, D. L.; Löhl, F.; Malyzhenkov, A.; Mancini, G. F.; Mankowsky, R.; Marcellini, F.; Marinkovic, G.; Martiel, I.; Märki, F.; Milne, C. J.; Mozzanica, A.; Nass, K.; Orlandi, G. L.; Loch, C. O.; Paraliev, M.; Patterson, B. D.; Patthey, L.; Pedrini, B. F.; Pedrozzi, M.; Pradervand, C.; Radi, P. P.; Raguin, J. Y.; Redford, S.; Rehanek, J.; Reiche, S.; Rivkin, L.; Romann, A.; Sala, L.; Sander, M.; Schietinger, T.; Schilcher, T.; Schlott, V.; Schmidt, T.; Seidel, M.; Stadler, M.; Stingelin, L.; Svetina, C.; Treyer, D. M.; Trisorio, A.; Vicario, C.; Voulot, D.; Wrulich, A.; Zerdane, S.; Zimoch, E., A compact and cost-effective hard X-ray free-electron laser driven by a high-brightness and low-energy electron beam. *Nature Photonics* **2020**, *14*, 748-754.
134. Aumonier, S.; Santoni, G.; Gotthard, G.; von Stetten, D.; Leonard, G. A.; Royant, A., Millisecond time-resolved serial oscillation crystallography of a blue-light photoreceptor at a synchrotron. *IUCrJ* **2020**, *7* (4), 728-736.
135. Aumonier, S.; Engilberge, S.; Caramello, N.; von Stetten, D.; Gotthard, G.; Leonard, G. A.; Mueller-Dieckmann, C.; Royant, A., Slow protein dynamics probed by time-resolved oscillation crystallography at room temperature. *IUCrJ* **2022**, *9* (6), 756-767.
136. Essen, L. O.; Klar, T., Light-driven DNA repair by photolyases. *Cellular and molecular life sciences : CMLS* **2006**, *63* (11), 1266-77.
137. Kiontke, S.; Geisselbrecht, Y.; Pokorny, R.; Carell, T.; Batschauer, A.; Essen, L.-O., Crystal structures of an archaeal class II DNA photolyase and its complex with UV-damaged duplex DNA. *The EMBO Journal* **2011**, *30* (21), 4437-4449.
138. Mees, A.; Klar, T.; Gnau, P.; Hennecke, U.; Eker, A. P.; Carell, T.; Essen, L. O., Crystal structure of a photolyase bound to a CPD-like DNA lesion after in situ repair. *Science (New York, N.Y.)* **2004**, *306* (5702), 1789-93.
139. Maestre-Reyna, M.; Yamamoto, J.; Huang, W. C.; Tsai, M. D.; Essen, L. O.; Bessho, Y., Twist and turn: a revised structural view on the unpaired bubble of class II CPD photolyase in complex with damaged DNA. *IUCrJ* **2018**, *5* (Pt 5), 608-618.
140. Murshudov, G. N.; Skubák, P.; Lebedev, A. A.; Pannu, N. S.; Steiner, R. A.; Nicholls, R. A.; Winn, M. D.; Long, F.; Vagin, A. A., REFMAC5 for the refinement of macromolecular crystal structures. *Acta crystallographica. Section D, Biological crystallography* **2011**, *67* (Pt 4), 355-67.
141. Müller, P.; Ignatz, E.; Kiontke, S.; Brettel, K.; Essen, L.-O., Sub-nanosecond tryptophan radical deprotonation mediated by a protein-bound water cluster in class II DNA photolyases. *Chemical Science* **2018**, *9* (5), 1200-1212.

7. Appendix

Appendix 1. Primer design for *CraCRY* mutants.

| Name | Forward primer sequence (5' to 3') |
|-----------------------------|--|
| <i>CraCRY</i> R485A | GATAGGCTGCCATGGCTGCAATACATGCTTTGC |
| <i>CraCRY</i> R485K | CGACGATAGGCTGCTGCCATCTTTGCAATACA TGCTTTGCTTG |
| <i>CraCRY</i> Y373F | GTTCCCAAGCTAACAAACAGATCACCACGGGTCA |
| <i>CraCRY</i> C482S | CAGTTGCAAGCAAAGCAAGTATTGCACGCATGGCA |
| <i>CraCRY</i> D321N | AGGTAATCCGGTGTGCAAACAAATTAATTGG GATGATAACC |
| <i>CraCRY</i> D323N | CCAGAAATTCCGGGTATCATTCCAATCAATTT GTTTGACAC |
| <i>CraCRY</i> D321ND323N | GTAATCCGGTGTGCAAACAAATTAATTGGAAT GATAACCCGGAATTTC |
| <i>CraCRY</i> E384Q | CTGATCAATCAGATGTTCTGAAAACTTC CATACCACG |
| <i>CraCRY</i> L387E | GAAGTGTTTGAAGAACATGAAATTGATCAGGATCATTAT |

Appendix 2. Reaction buffer of site-directed mutagenesis.

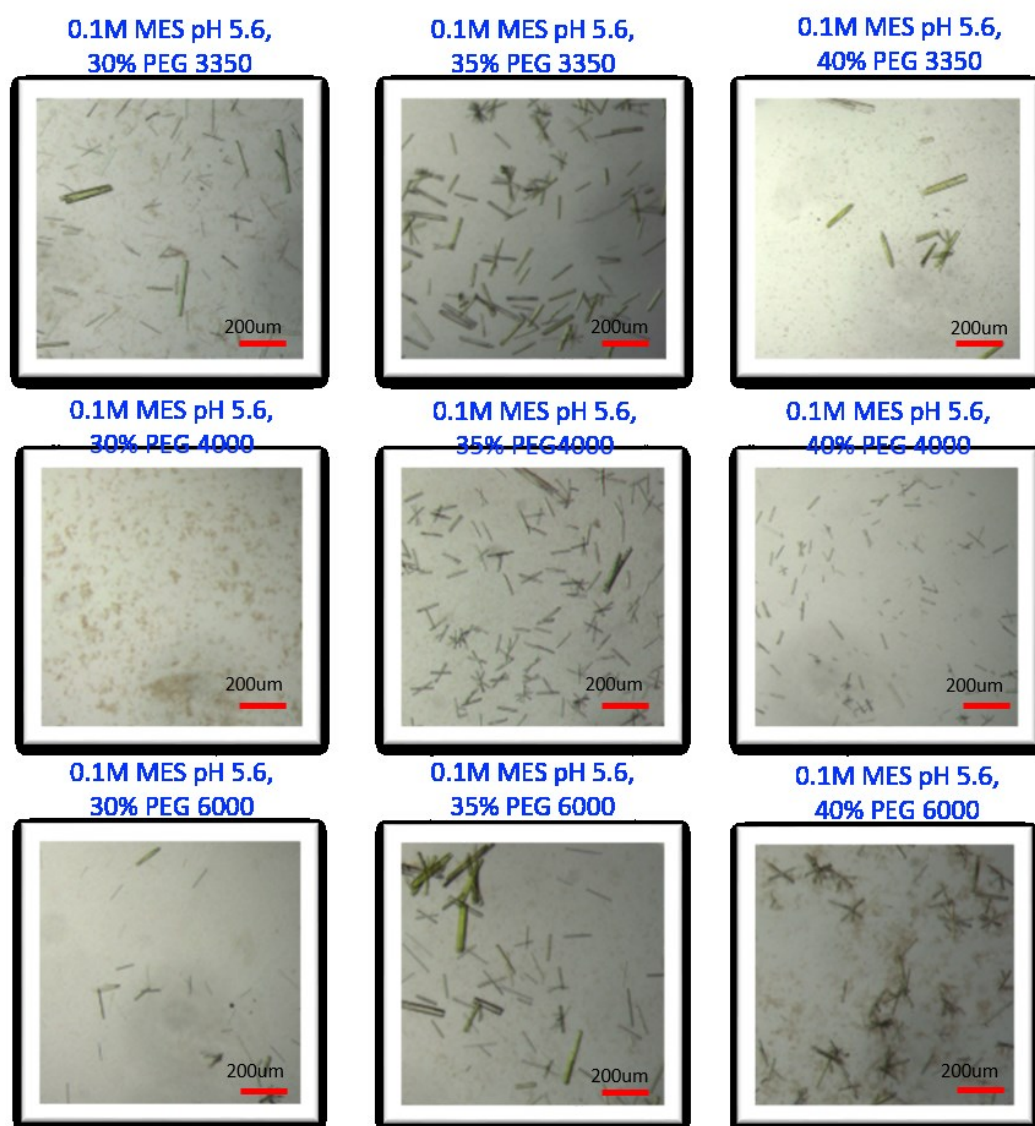
| Content | Volume |
|---|---------|
| 10 x reaction buffer | 2.5 µl |
| 25 ng of dsDNA template | 2.5 µl |
| 125 ng of primer F | 0.5 µl |
| 125 ng of primer R | 0.5 µl |
| dNTP mix | 0.5 µl |
| QuickSolution reagent | 0.75 µl |
| QuickChange Lightning Enzyme | 0.5 µl |
| Add ddH ₂ O to a final volume of 25 µl | |

Appendix 3. 2YT medium preparation.

| Content per liter | Amount |
|---|--------|
| Tryptone | 16g |
| Yeast extract | 10g |
| Sodium Chloride | 5g |
| 50 mg/L Kanamycin | 1ml |
| Add ddH ₂ O to a final volume of 1 L | |

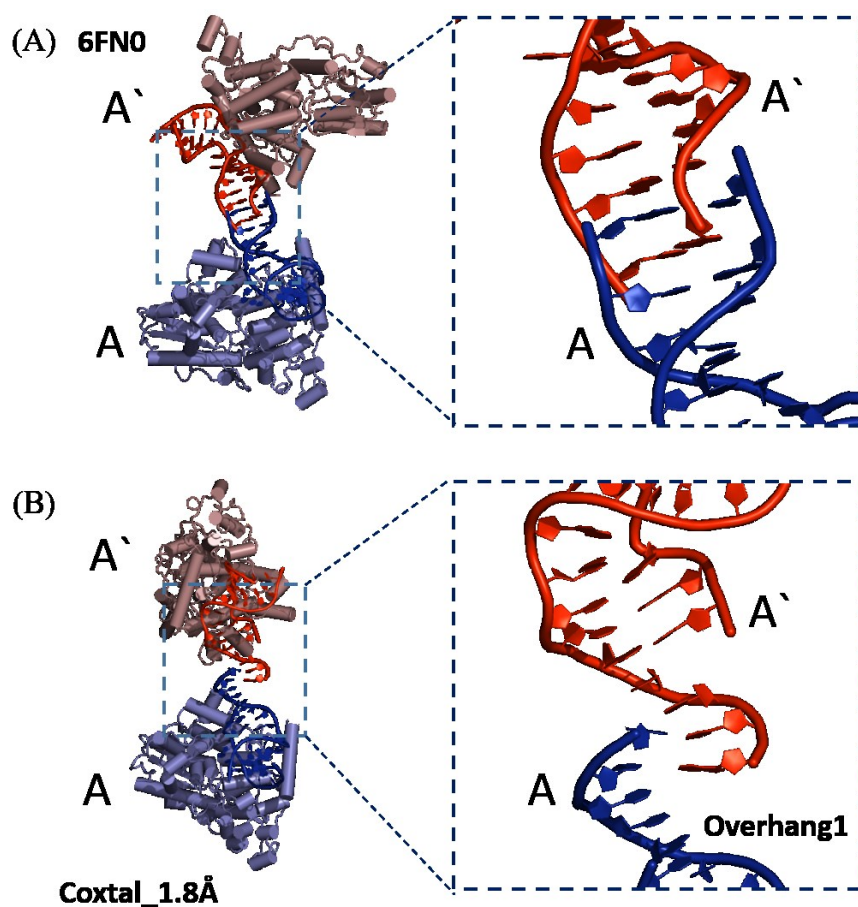
Appendix 4. Purification buffers of *CraCRY*.

| Purification Step | Buffer name | Content |
|---------------------------------|-----------------------|-------------------------------|
| Nickel-NTA | Loading buffer | 50 mM sodium phosphate pH 7.8 |
| | | 100 mM NaCl |
| | | 20% (v/v) glycerol |
| | Wash buffer | 50 mM sodium phosphate pH 7.8 |
| | | 100 mM NaCl |
| | | 20% (v/v) glycerol |
| | | 25 mM imidazole |
| | Elution buffer | 50 mM sodium phosphate pH 7.8 |
| | | 100 mM NaCl |
| | | 20% (v/v) glycerol |
| | | 250 mM imidazole |
| Heparin affinity chromatography | A buffer | 50 mM sodium phosphate pH 7.8 |
| | | 100 mM NaCl |
| | | 20% (v/v) glycerol |
| | B buffer | 50 mM sodium phosphate pH 7.8 |
| | | 250 mM NaCl |
| Size exclusion chromatography | Gel filtration buffer | 0.1 M Tris PH8.5 |
| | | 200mM NaCl |

Appendix 5. Size screening of CraCRY crystals.

Different types and percentage (w/v) of PEG can cause different sizes of CraCRY crystals. There is a trend showing that higher percentages of PEG reduce the amount of crystals.

Appendix 6. Structure comparison between 6FN0 and TPS05A data.

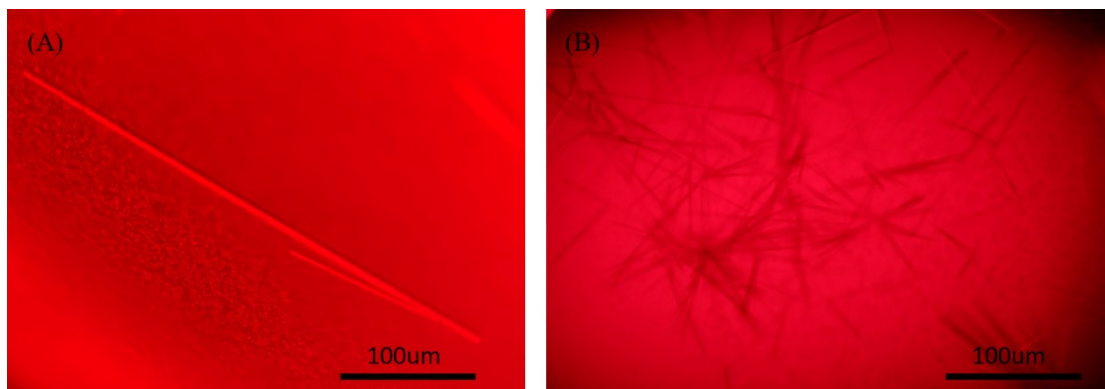


(A) Base on 6FN0, the DNA between symmetry crystal units were cross together, so that the crystal was hard to perform. (B) The CraCRY and overhang1 DNA can perform a non-interlock form of DNA, and was obtained at 1.8Å resolution from TPS05A.

Appendix 7. Different sequences of 6-4 DNAs.

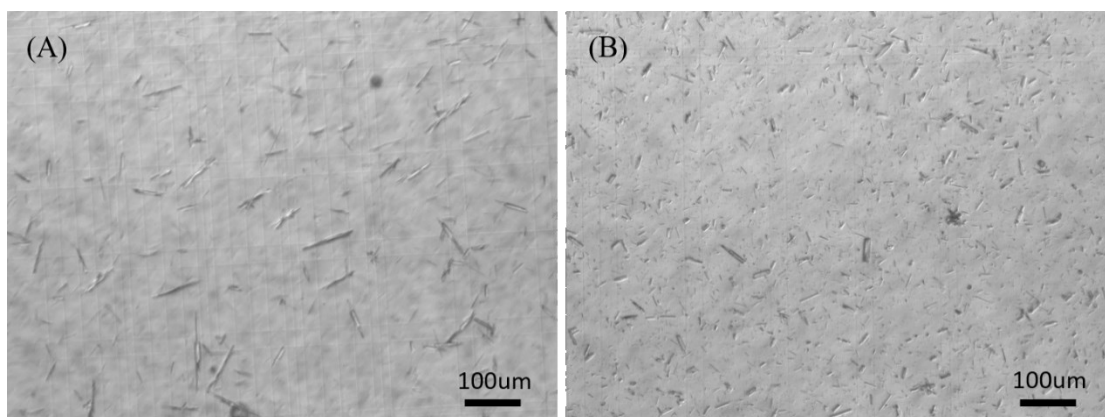
| Name | Sequence |
|--------------------|--|
| Overhang1 DNA | 5'-AGCGGT\trianglerightTGCCGTG-3' 3'-GCTCGCCA\trianglerightACGGCAC-5' |
| Overhang2 DNA | 5'-CGCGGT\trianglerightTGCCGTG-3' 3'-GCGCGCCA\trianglerightACGGCAC-5' |
| Shorter DNA | 5'-CGCGGT\trianglerightTGCCGTG-3' 3'-GCGCCA\trianglerightACGGCAC-5' |
| Labile-overlap DNA | 5'-AGCGGT\trianglerightTGCCGTG-3' 3'-GCTCGCCA\trianglerightACGGCAC-5' |

Appendix 8. CraCRY-DNA crystals comparison between with and without streak seeding.



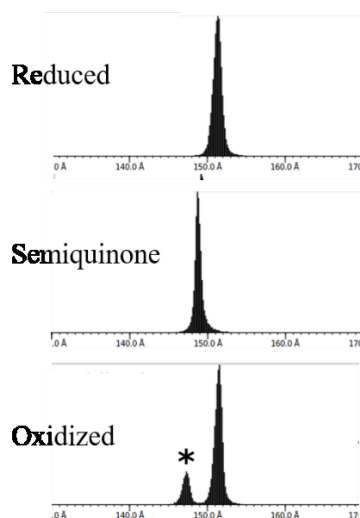
(A) The co-crystals were grow about 300 μm in length and provided few crystals. (B) With streak seeding method, plenty smaller crystals (about 75 μm in length) were grow and suitable for TR-SFX experiments.

Appendix 9. CraCRY crystals comparison between with and without crashing.



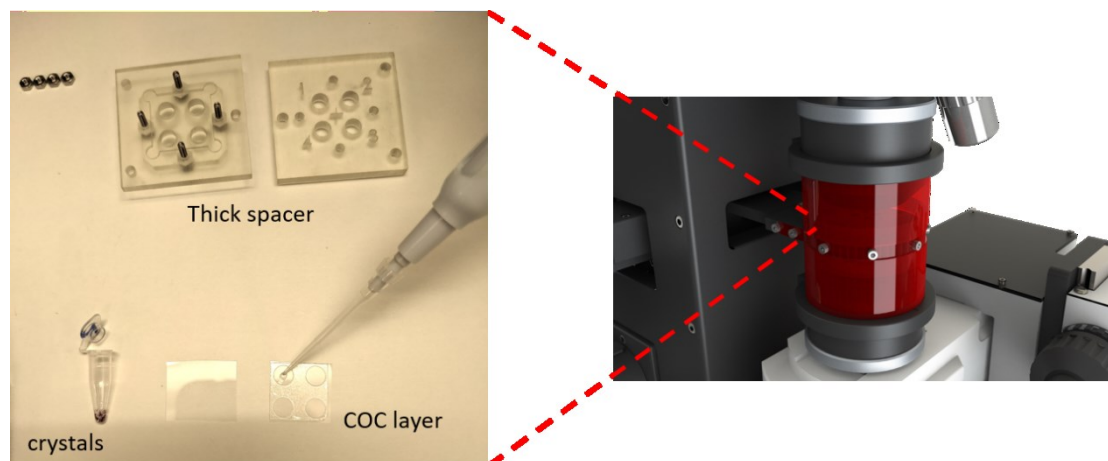
(A) During storage, some CraCRY crystals grow over 100 μm in length which affected the injecting flow of TR-SFX experiments. (B) After crashing with homogenizer, large size of crystals crashed to fragmentary crystals.

Appendix 10. Unit cell of *c*-axis changes upon photoreduction in *CraCRY*.



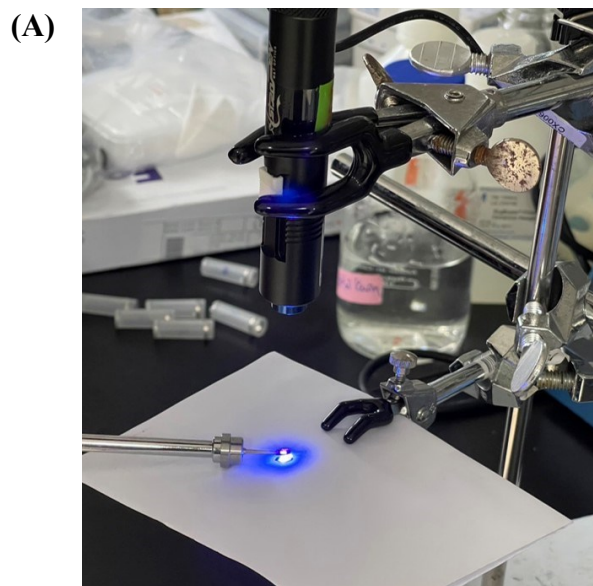
The *c*-axis distributions of indexed crystals in the oxidized form (bottom), semiquinone (middle) and fully reduced hydroquinone (top). Upon photoreduction to the semiquinone state, crystals compressed, as shown by shortening of the *c*-axis. If the sample was further photoreduced to the fully reduced state, this effect was reversed, and crystals adopted the same form as in the oxidized state. All crystals used for these experiments were derived from the same crystallization batch. Further, the effect could be reproduced in situ, as shown for the oxidized crystals. Here, oxidized data collection was briefly stopped, and part of the sample was illuminated with constant white light for about 5 minutes. As a result, a small number of crystals adopted the semiquinone compact form, as marked by an asterisk. The *c*-axis was 151.54 Å in oxidized, 148.72 Å in semiquinone and 151.54 Å in reduced state respectively.

Appendix 11. Schematic of sample holder for TR-icOS.

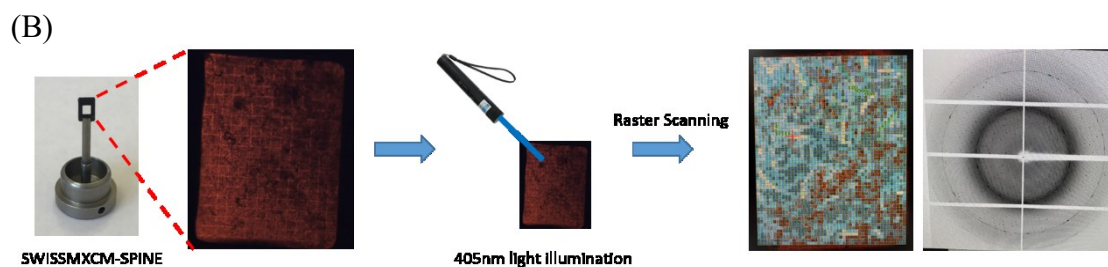


The sample holder was composed by two COC layers which containing 2 μ l crystals slurry and covered by two thick spacers form the top and the bottom to produce a sandwich. The sandwich was protected by a red plastic cover to avoid light contamination as much as possible. The photos were provided by Dr. Sylvain Engilberge, ESRF.

Appendix 12. Schematic of Cryo-trapping setup.



The 405 nm laser pointer was setup in a 10 cm distance with the sample holder. After illuminating, froze the crystals immediately.



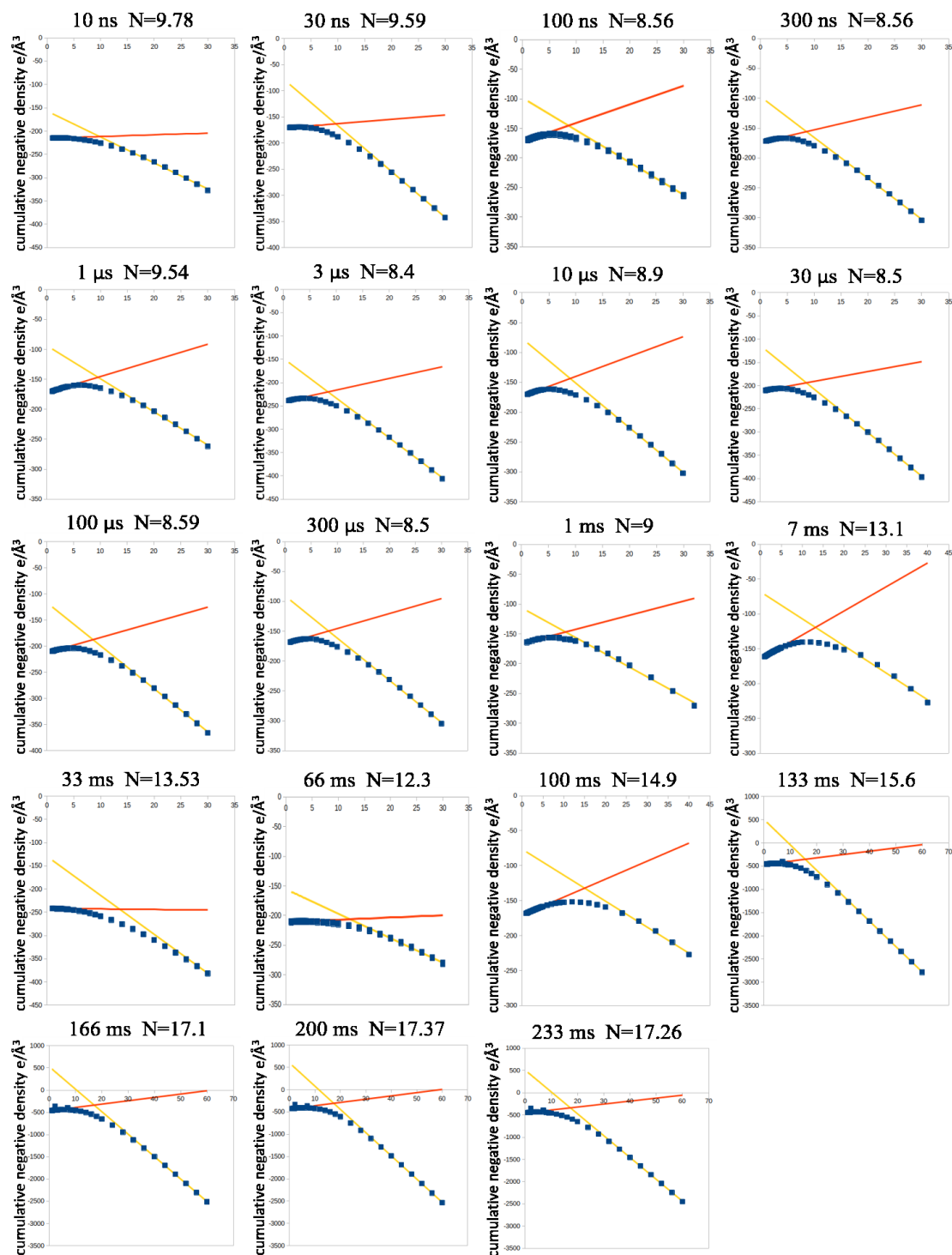
A flow chart of the entire experiments. Under the safety red light, the hundreds of microcrystals were loaded on the spine. After illuminated and mounted the crystals to goniometer, rasterization scanning was to check the crystals position and collected small angle of diffraction images around 400 crystals.

Appendix 13. Primary properties of the *Cra*CRY TR-SFX structures.

| Structure name | Torsion N395 (deg) | Distance FADN5–R360Nε (Å) | Distance FADN5–N395Oδ (Å) | Distance N395–E384 (Å) | Distance H309–E384 (Å) | Distance R492–D321 (Å) ^a | Res. |
|--------------------|--------------------|---------------------------|---------------------------|------------------------|------------------------|-------------------------------------|------|
| C _{dark} | 0 | 3.8 | 3.7 | 5.0 | 7.9 | 4.5 | 1.64 |
| C _{10ns} | -1.69 | 3.78 | 3.87 | 5.1 | 7.4 | 5.2 | 1.9 |
| C _{30ns} | 21.23 | 3.66 | 3.17 | 5.2 | 8.1 | 5.5 | 1.95 |
| C _{100ns} | 74.52 | 3.67 | 2.95 | 6.3 | 8 | 5 | 1.95 |
| C _{300ns} | 81.01 | 3.67 | 2.96 | 6.3 | 6.7 | 5.4 | 1.9 |
| C _{1μs} | 73.77 | 3.49 | 2.8 | 4.4 | 3.1 | N/A | 1.95 |
| C _{3μs} | 83.15 | 3.5 | 3.03 | 3.7 | 2.9 | N/A | 1.85 |
| C _{10μs} | 75.11 | 3.39 | 3.05 | 4.7 | 2.9 | N/A | 1.95 |
| C _{30μs} | 75.87 | 3.57 | 3.01 | 4.1 | 3.2 | N/A | 1.9 |
| C _{100μs} | 77.63 | 3.57 | 3.14 | 4.2 | 3.1 | N/A | 1.9 |
| C _{300μs} | 71.54 | 3.47 | 2.98 | 4 | 3.2 | N/A | 1.9 |
| C _{1ms} | 50.66 | 3.99 | 2.92 | 3.9 | 3.3 | N/A | 1.9 |
| C _{7ms} | 75.17 | 3.88 | 3.18 | 4 | 3.1 | N/A | 2.0 |
| C _{33ms} | 72.13 | 3.64 | 2.85 | 5.8 | 8.1 | N/A | 1.85 |
| C _{66ms} | 33.81 | 3.8 | 2.8 | 5.5 | 7.5 | N/A | 2.3 |
| C _{100ms} | 39.77 | 4.22 | 2.47 | 5.5 | 7.5 | N/A | 2.15 |
| C _{133ms} | 27.91 | 3.99 | 2.41 | 5.5 | 8.1 | N/A | 2.2 |
| C _{166ms} | 29.58 | 3.94 | 2.71 | 6.7 | 8.4 | N/A | 2.2 |
| C _{200ms} | 29.41 | 4.09 | 2.38 | 4.9 | 7.3 | N/A | 2.2 |
| C _{233ms} | 24.68 | 4.42 | 2.32 | 5.4 | 7.1 | N/A | 2.25 |

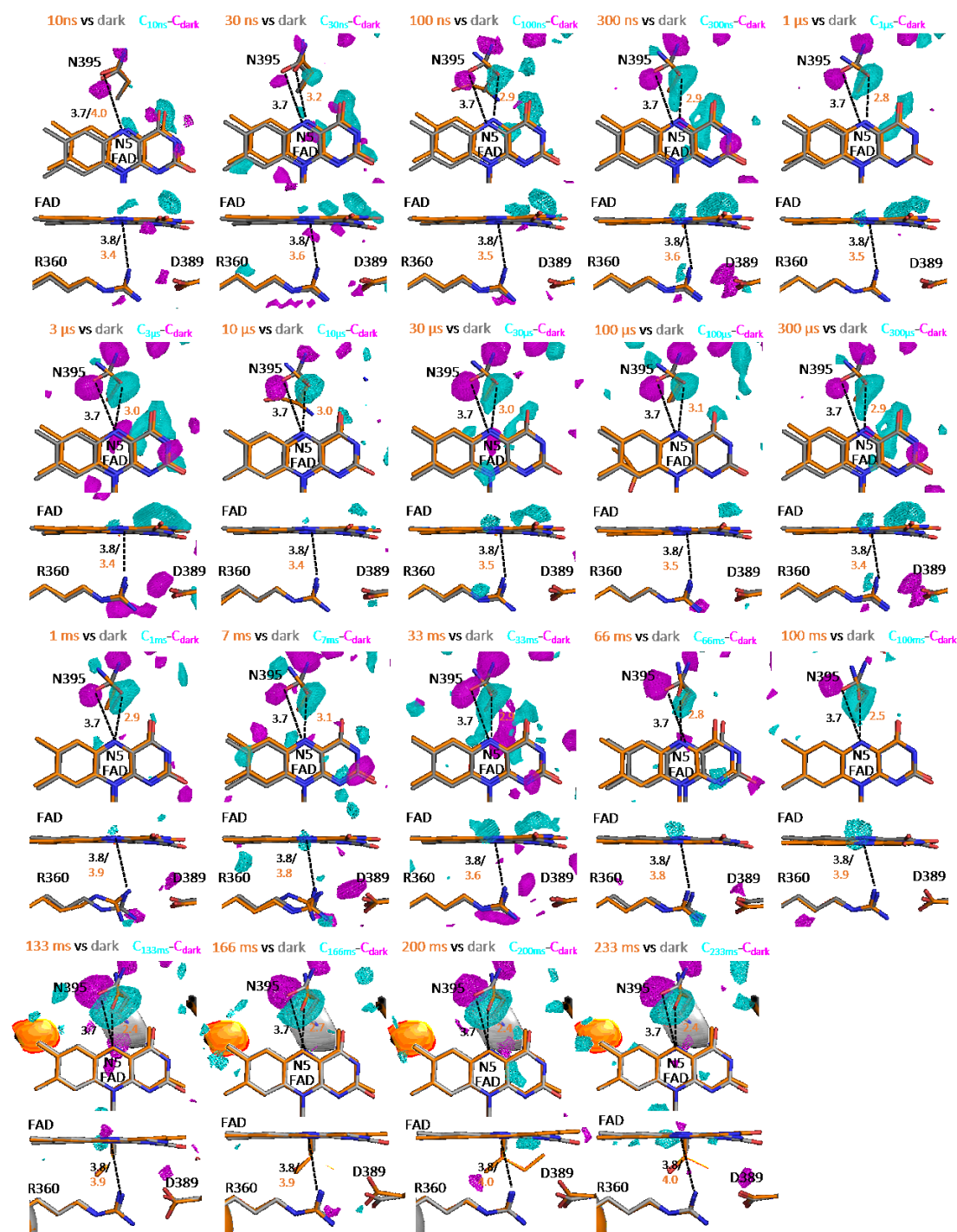
^aR492 was undetermined from C_{1μs} due to light illumination resulting in C-terminal region unfolding.

Appendix 14. Extrapolation plot at all-time points.



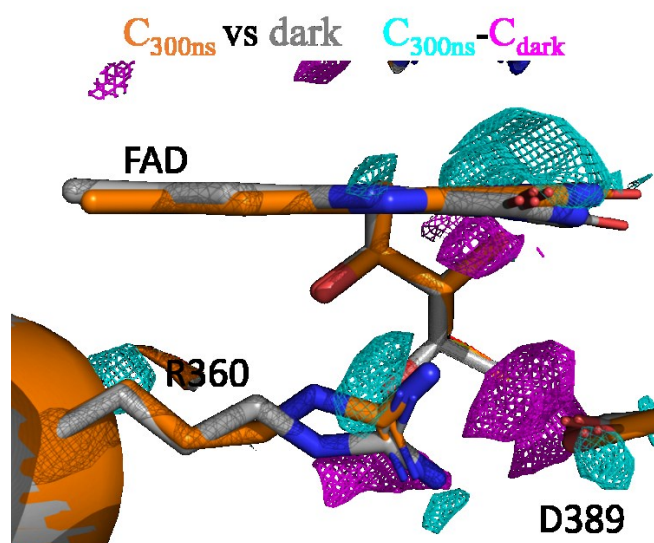
The extrapolation plots were based on N395 for datasets of 10 ns to 100 ms delay times, datasets for 133 ms to 233 ms depended on a short region of the C-terminus (RMAAYRRSK) that gets increasingly disordered. Each blue spot represented the extrapolated N value of cumulative negative density individually. The intersection between red and yellow trend lines was the N value used for the occupancy calculation and structure determination.

Appendix 15. Structures of the FAD binding site at all-time points.



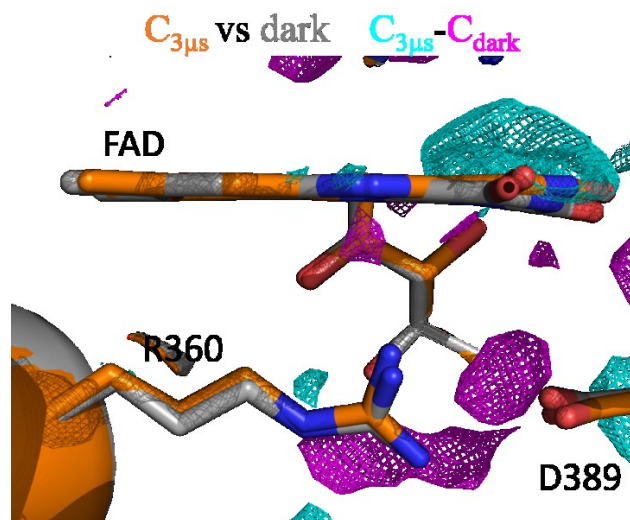
The entire transition of CraCRY C_{dark} to C_{signal} progress at FAD binding site. TR-SFX structural snapshots of CraCRY (C_x , orange) are shown in comparison to C_{dark} (grey). To highlight the experimental significance of the observed differences, 3.5 σ contoured isomorphous difference electron densities (DEDS) are shown in cyan for positive peaks and magenta for negative ones. The C_{dark} and C_x distance are shown in black and orange respectively. In all C_x , N395 was keeping in shorter distance except for $C_{10\text{ns}}$. Meanwhile, C_x (between ns and μ s) are shown shorter distance between R360 and FAD N5, whereas returning to initial position in ms range.

Appendix 16. Close view of 300 ns at R360.



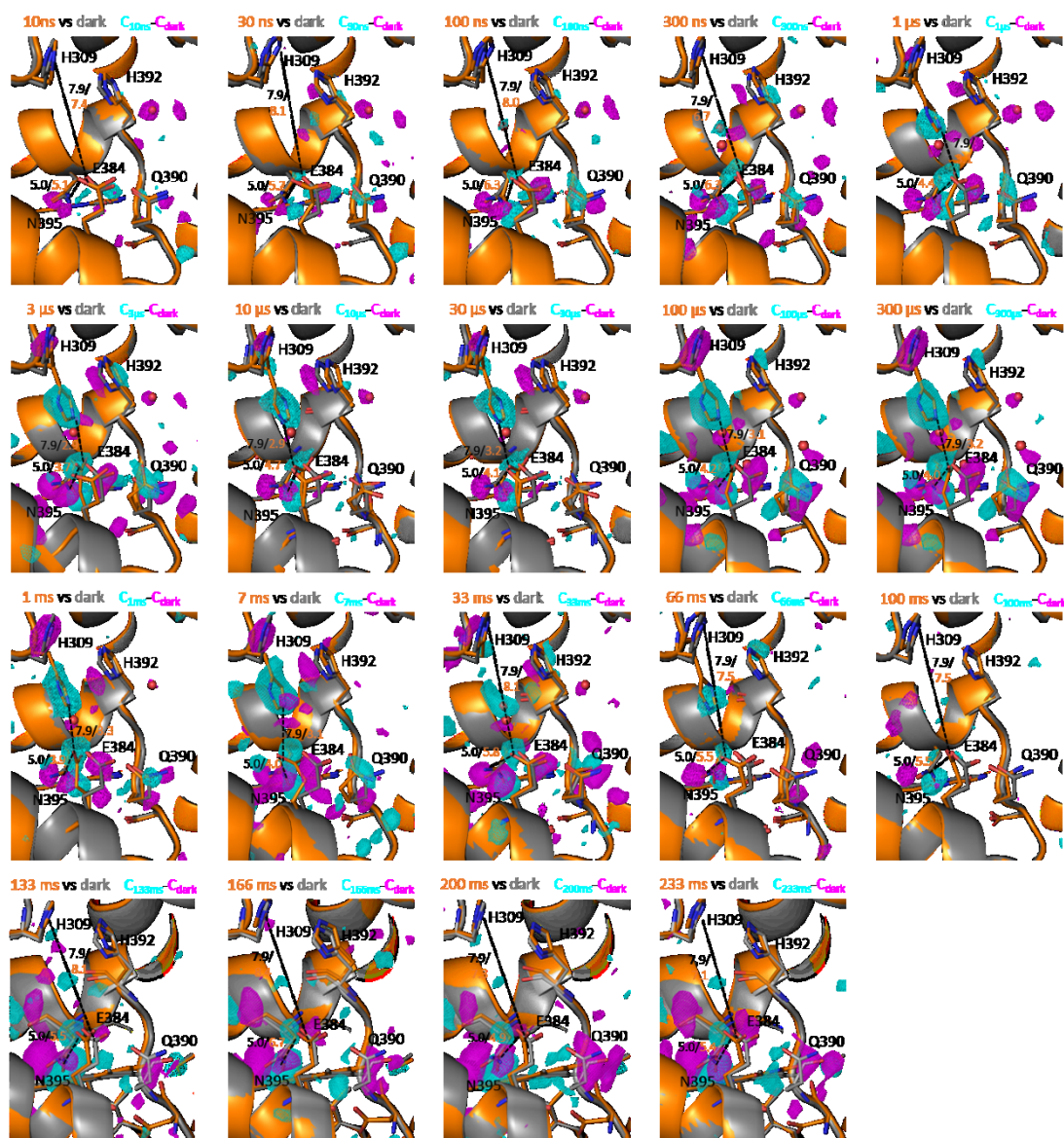
Snapshot of CraCRY C_{300ns} (orange) is shown in comparison to C_{dark} (grey). To highlight the experimental significance of the observed differences, 3.5 σ contoured isomorphous DEDs are shown in cyan for positive peaks and magenta for negative ones. Clearly strong difference maps were shown at R360.

Appendix 17. Close view of 3 μ s at R360.



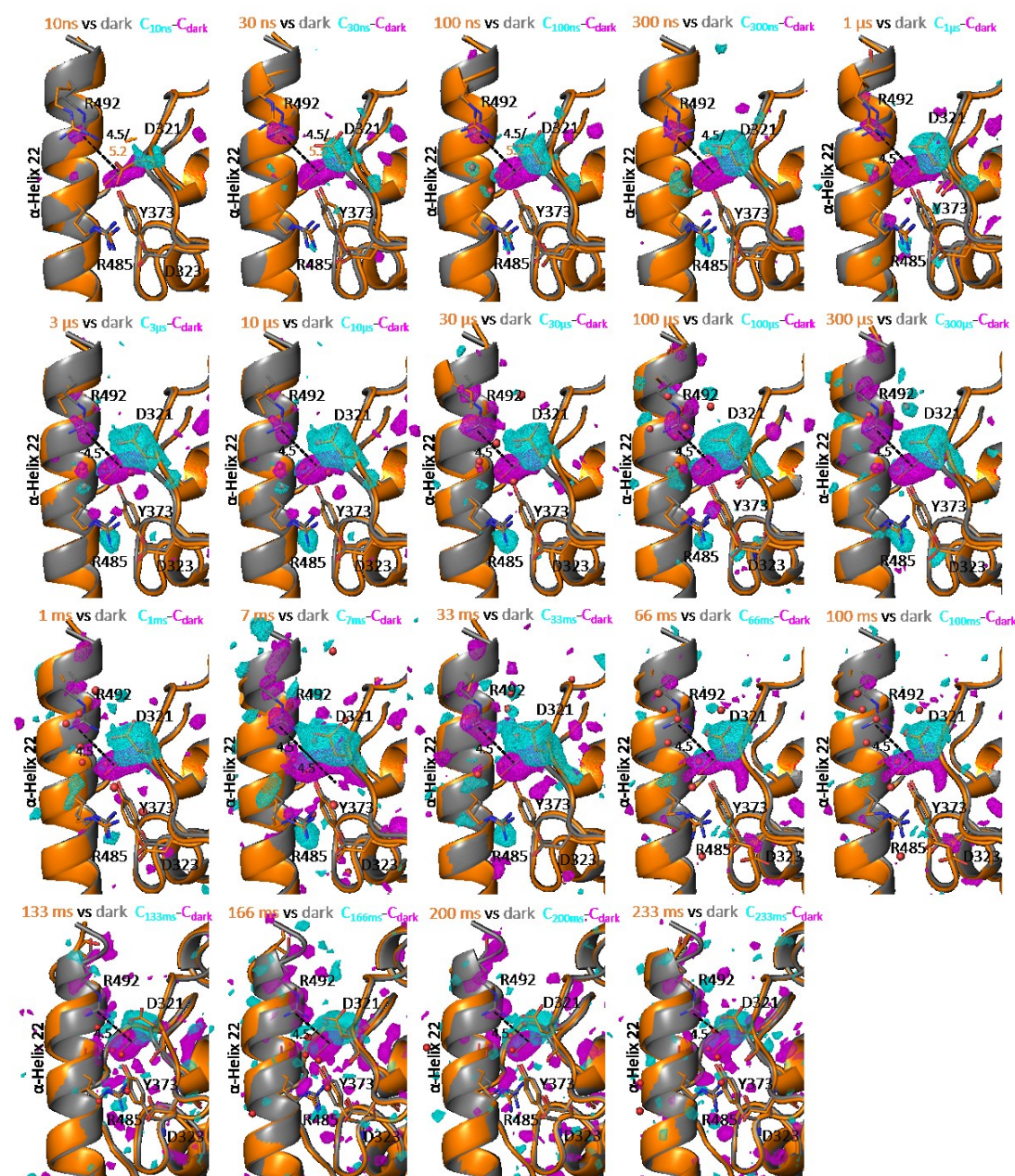
Snapshot of CraCRY $C_{3\mu s}$ (orange) is shown in comparison to C_{dark} (grey). To highlight the experimental significance of the observed differences, 3.5 σ contoured isomorphous DEDs are shown in cyan for positive peaks and magenta for negative ones. Rarely weak difference maps were shown at R360.

Appendix 18. Structures of the solvent expose patch at all-time points.



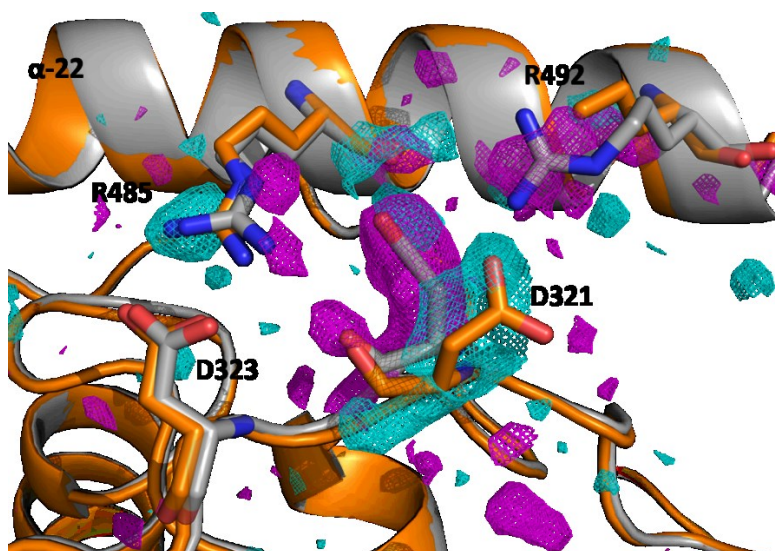
The entire transition of CraCRY C_{dark} to C_{signal} progress at solvent expose patch and which were shown detailed view of proton transfer relevant residues (H309, E384, Q390 and H392). TR-SFX structural snapshots of CraCRY (C_x , orange) are shown in comparison to C_{dark} (grey). To highlight the experimental significance of the observed differences, 3.5 σ contoured isomorphous DEDs are shown in cyan for positive peaks and magenta for negative ones. The C_{dark} and C_x distance are shown in black and orange respectively. The distance changes between H309 and E384 in μ s to few ms, and indicating protonation event took place in a hounded of ms.

Appendix 19. Structures of the C-terminal region at all-time points.



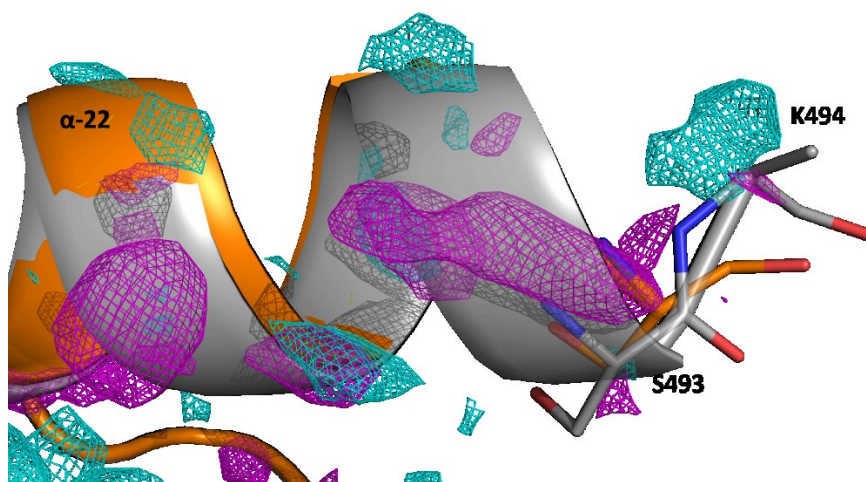
The entire transition of CraCRY C_{dark} to C_{signal} progress at C-terminal region and which were shown detailed view of C terminus unfolding. TR-SFX structural snapshots of CraCRY (C_x , orange) are shown in comparison to C_{dark} (grey). To highlight the experimental significance of the observed differences, 3.5σ contoured isomorphous DEDs are shown in cyan for positive peaks and magenta for negative ones. The C_{dark} and C_x distance are shown in black and orange respectively. In the early ns, D321 moved away from R492, resulting in first salt bridge broken. Thus, negative density was continuous cumulative in C-terminal region and second salt bridge broken (D323 and R485), eventually.

Appendix 20. Close view of $C_{3\mu s}$ revealing side chain of R492 delocalizing.



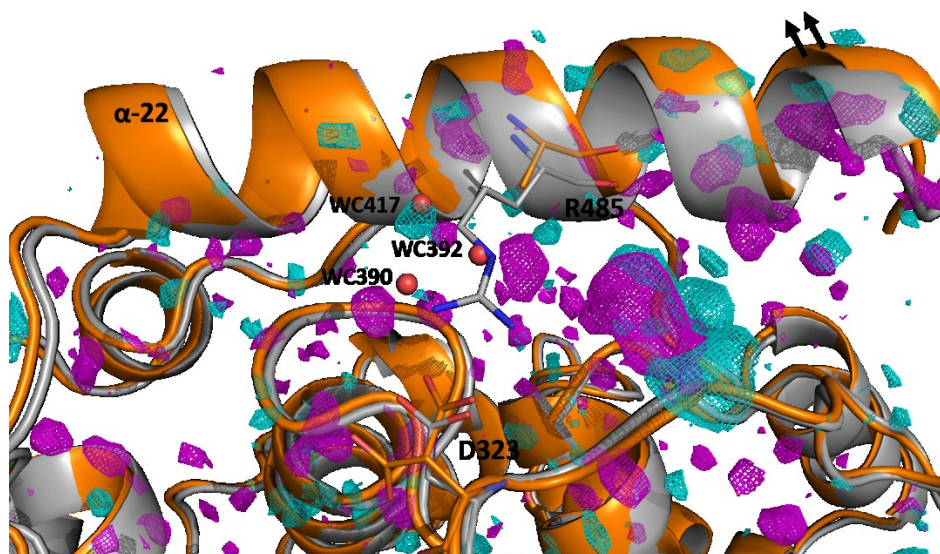
Snapshot of CraCRY $C_{3\mu s}$ (orange) is shown in comparison to C_{dark} (grey). To highlight the experimental significance of the observed differences, 3σ contoured isomorphous DEDs ($C_{3\mu s} - C_{dark}$) are shown in cyan for positive peaks and magenta for negative ones. Strong negative density maps were shown at R492, thus the side chain of R492 was not able to determinate. Meanwhile, the R485 in $C_{3\mu s}$ started to appear the difference map.

Appendix 21. Close view of C_{7ms} revealing K494 residue delocalizing completely.



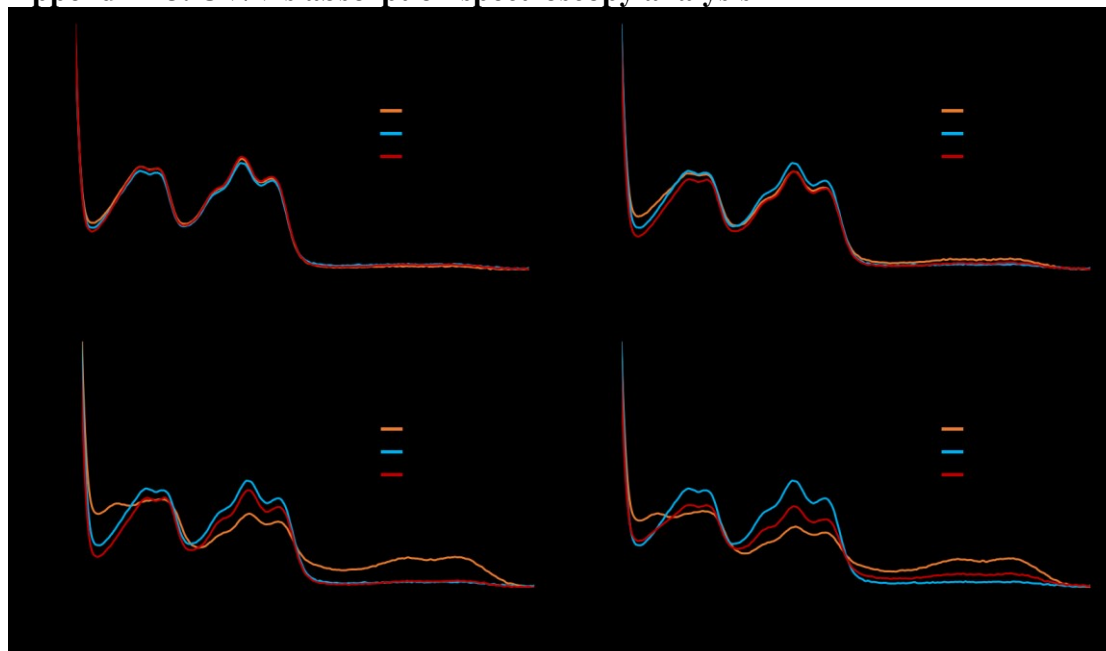
Snapshot of CraCRY $C_{7\mu s}$ (orange) is shown in comparison to C_{dark} (grey). To highlight the experimental significance of the observed differences, 3σ contoured isomorphous DEDs ($C_{7\mu s} - C_{dark}$) are shown in cyan for positive peaks and magenta for negative ones. Via alignment between C_{7ms} and C_{dark} , clearly observing K494 undeterminable in C_{7ms} .

Appendix 22. Close view of C_{233ms} revealing side chain of R485 delocalizing.



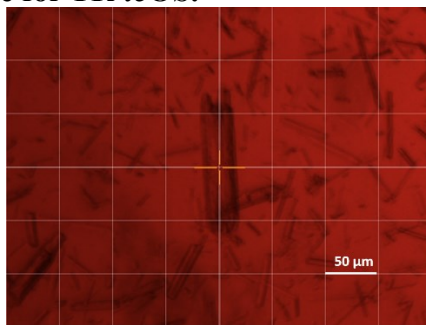
Snapshot of CraCRY C_{233ms} (orange) is shown in comparison to C_{dark} (grey). To highlight the experimental significance of the observed differences, 3σ contoured isomorphous DEDs ($C_{233ms} - C_{dark}$) are shown in cyan for positive peaks and magenta for negative ones. More strong negative density maps were shown entire $\alpha 22$, the side chain of R485 was not able to determinate and occupying by three waters (WC390, WC392, WC417). The arrows were pointed out a direction which leading $\alpha 22$ unfolding.

Appendix 23. UV/Vis absorption spectroscopy analysis



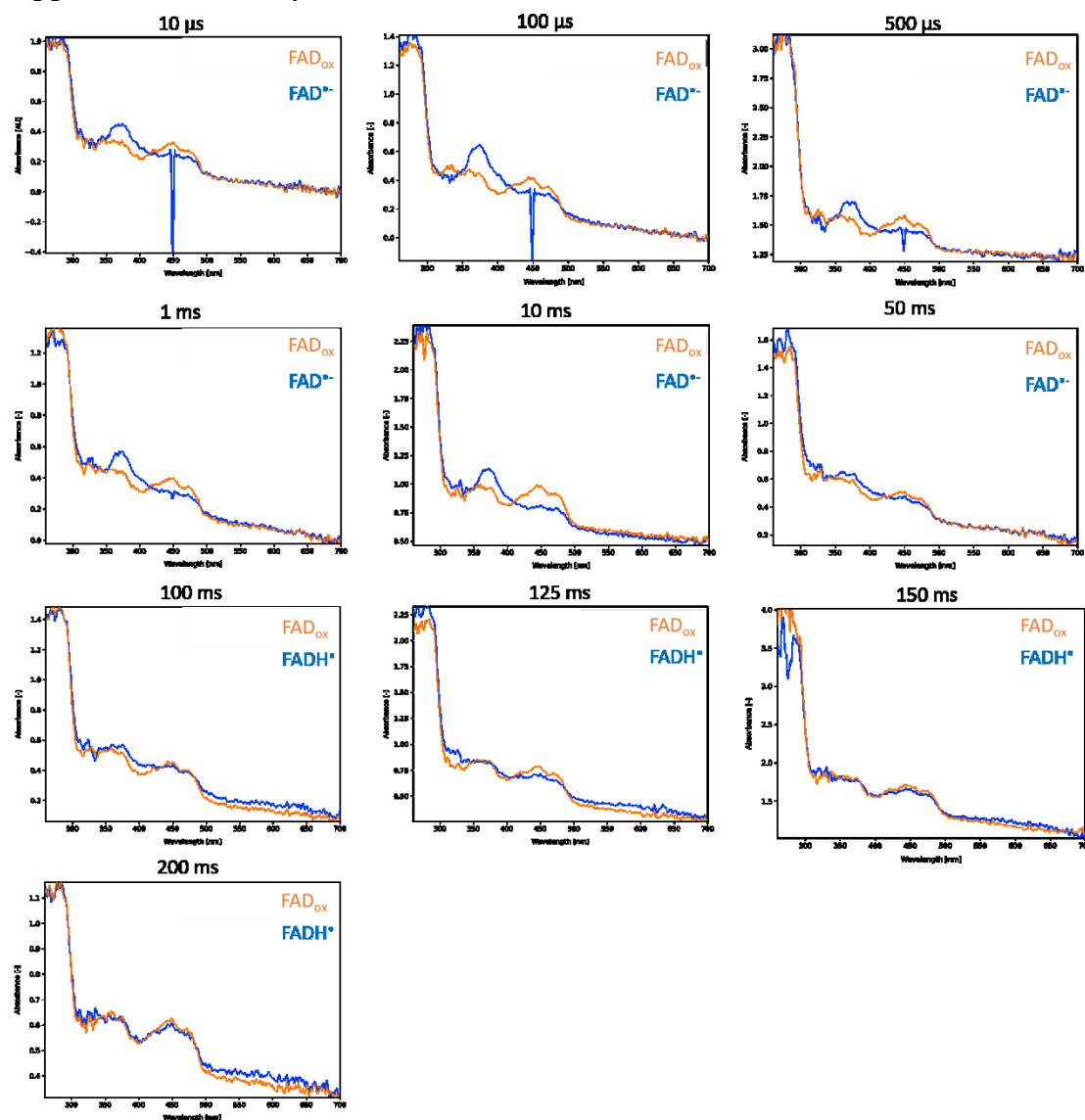
UV-Vis absorption spectroscopy results in showing the difference between the WT and E384Q. The spectrum was taken after light illumination for 5 minutes as described in method section 3.7. The illuminated WT and E384Q were shown in orange and red respectively, meanwhile, WT and E384Q dark control were shown in black and blue respectively.

Appendix 24. Crystal size for TR-icOS.



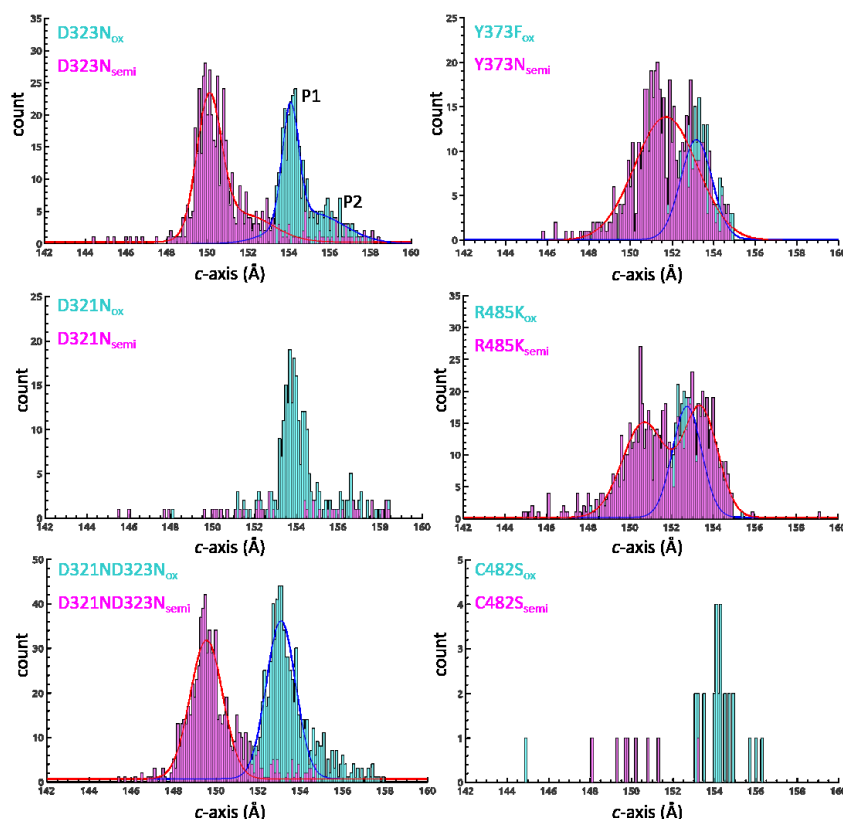
The typical size of the crystals used for the measurements were $100 \times 35 \times 35 \mu\text{m}^3$.

Appendix 25. Entirety TR-icOS measurement in *CraCRY*.



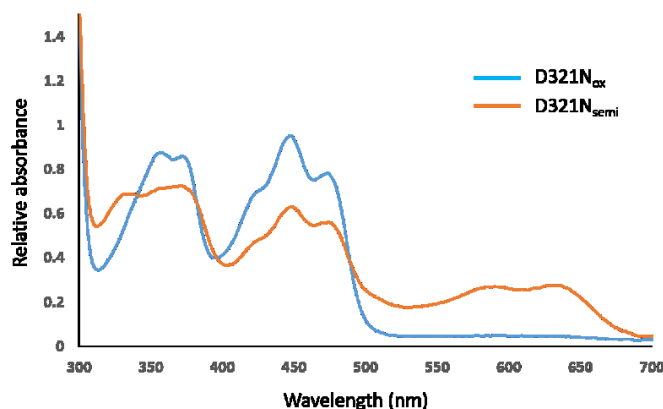
All time points of spectra were shown from $10 \mu\text{s}$ to 200 ms . The FAD_{ox} spectrum was shown in orange and $\text{FAD}^{\bullet-}$ and FADH^{\bullet} were shown in blue respectively. The whole transition of $\text{FAD}^{\bullet-}$ to FADH^{\bullet} in *CraCRY* can be observed. The TR-icOS experiments were performed by Dr. Sylvain Engilberge, ESRF.

Appendix 26. The histogram's distribution of mutants in oxidized and semiquinone states.



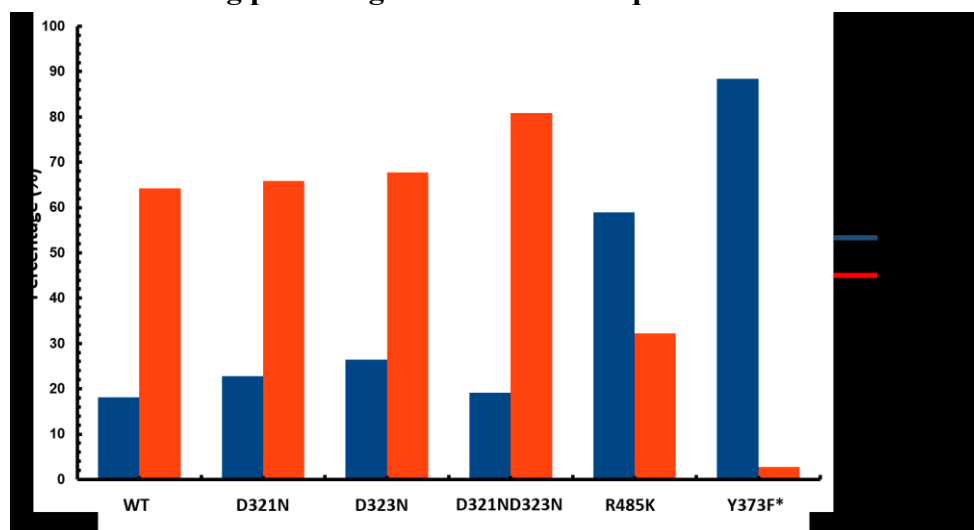
Histogram of *c*-axis in semiquinone dataset of relevant mutants. The histogram of oxidized and semiquinone were shown in cyan and magenta and Gaussian fitting in blue and red, respectively. Here, D323N and R485K can fit with mutli-peak due to different histogram distribution. To be note that, D321N and C482S were too few crystals to use Gaussian fitting method.

Appendix 27. UV/Vis absorption spectroscopy D321N



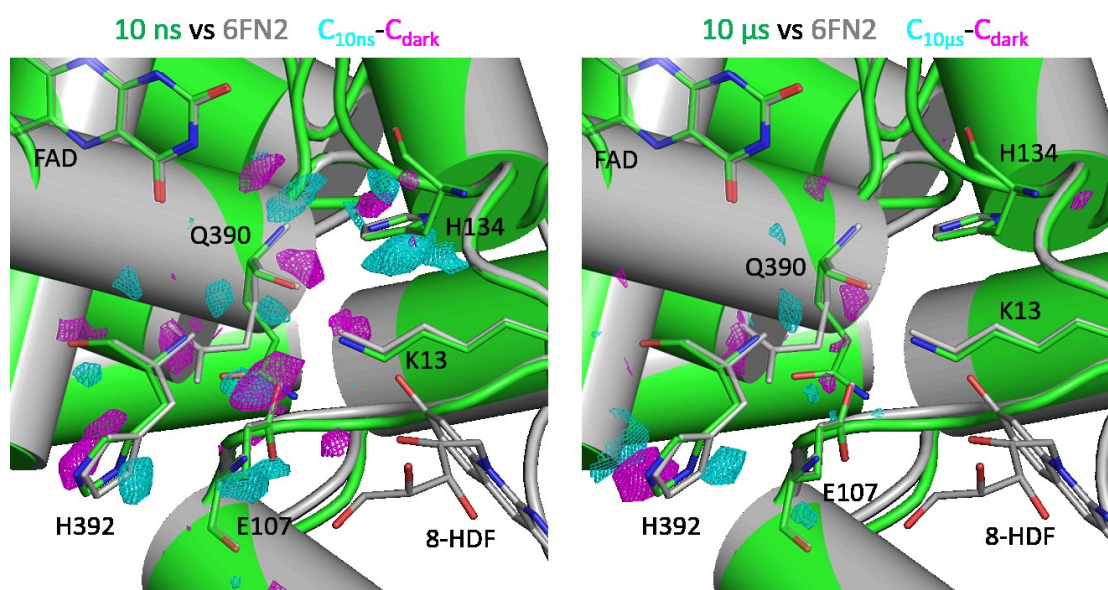
UV-Vis absorption spectroscopy results in showing the difference between the D321N_{ox} and D321N_{semi}. The spectrum was taken after light illumination for 5 minutes as described in method section 3.7. The D321N_{ox} and D321N_{semi} were shown in blue and orange respectively.

Appendix 28. Shifting percentage of *c*-axis in semiquinone datasets.



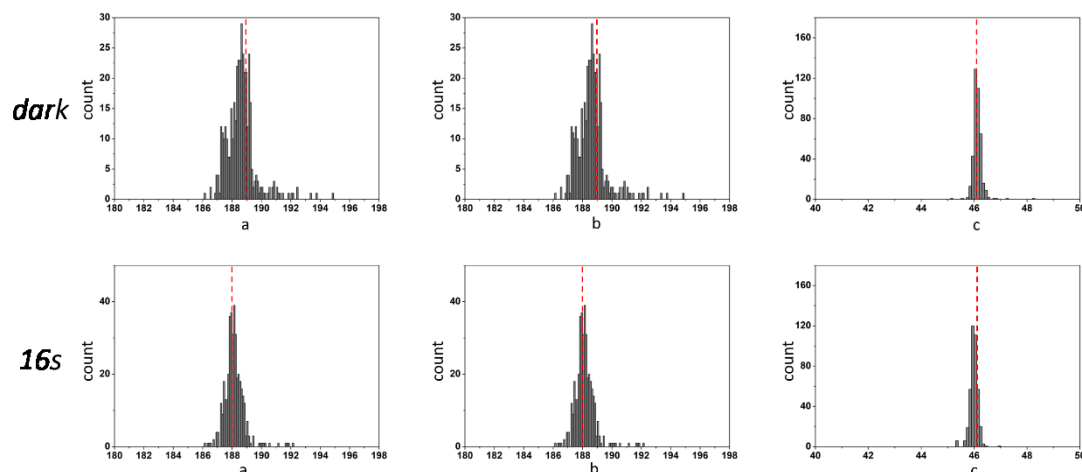
Different shifting percentages of *c*-axis in mutant its semiquinone state. To be note that, after a period of time of light illumination, WT, D321N and D323N were shown similar shifting percentage towards to shorter *c*-axis, in contrast, more R485K prefer to stay in long axis. *Y373F acts as the negative control.

Appendix 29. Possible proton transfer chain.



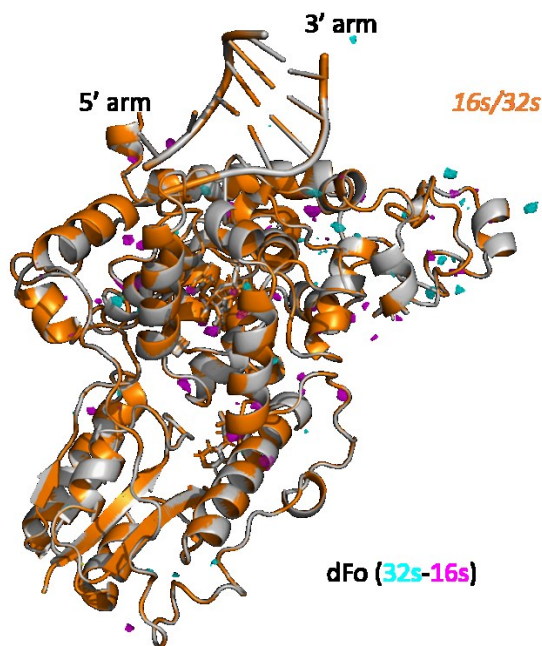
Snapshot of CraCRY C_{10ns} (left) and $C_{10\mu s}$ (right) in orange were shown in comparison to 6FN2 (gray). To highlight the experimental significance of the observed differences, 3σ contoured isomorphous DEDs ($C_x - C_{dark}$) are shown in cyan for positive peaks and magenta for negative ones. Strong DEDs were shown surrounding in 8-HDF binding pocket. Over a period of time to $10\mu s$, the relevant residues returned to original position.

Appendix 30. Unit cell distribution in *dark* and *16s*.



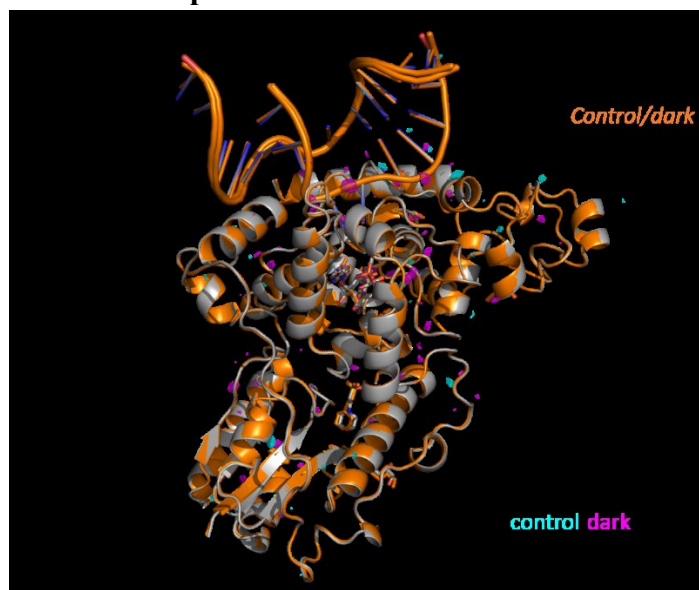
Both superdataset of *dark* and *16s* were shown the distribution of *a*, *b* and *c* axis. By *16s* illumination, clearly observing *a* and *b* were being shortened by 1 Å, and unique *c*-axis remained constant. Red lines were based on the refinement statistics (Table 6).

Appendix 31. Structure comparison between *16s* and *32s*.



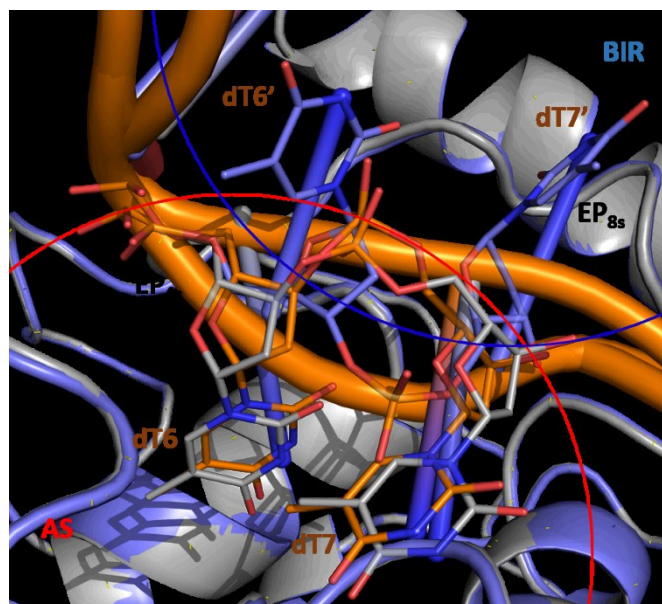
(E) Overall structural comparison between *16s* and *32s*. The *32s* illuminated structure was shown in orange, and superposed over *16s* (gray). Additionally, difference maps are shown at 3.5σ contour level, with positive values in cyan, while negative in magenta. Here, few DEDs can be observed between *16s* and *32s*, indicating high similarity of structures.

Appendix 32. Structure comparison between *dark* and *control*.



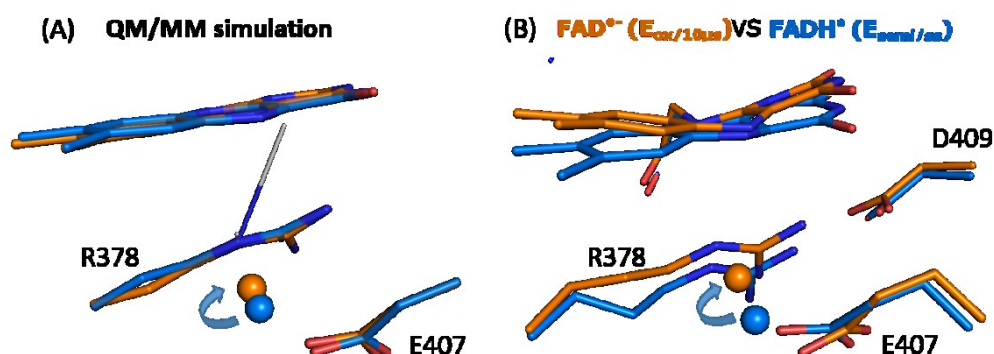
(E) Overall structural comparison between dark and control. The 16s illuminated in absence of reducing agent as control was shown in orange, and superposed over dark (gray). Additionally, difference maps are shown at 3.5σ contour level, with positive values in cyan, while negative in magenta. Here, few DEDs can be observed between 16s and 32s, indicating high similarity of structures.

Appendix 33. Double conformations of 8s structure.



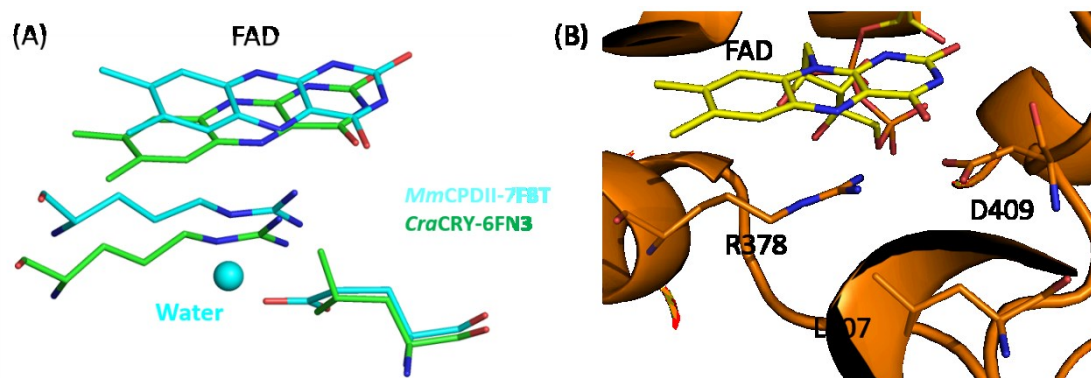
Detail of the 8s intermediate structure. Both dT6 and dT7 have flipped out of the active site (red circle), and are in the process of entering the unpaired bubble by displacing the BIR (blue circle). The EP_{4s} was superposed with 8s model, showing the sticks with gray color. Here, double conformations can be observed in 8s, which in partial overlapping with EP_{4s} (dT6 and dT7). On the other hand, dT6' and dT7' flipped in BIR can be determined in EP_{8s} .

Appendix 34. Observing water movement upon protonation.

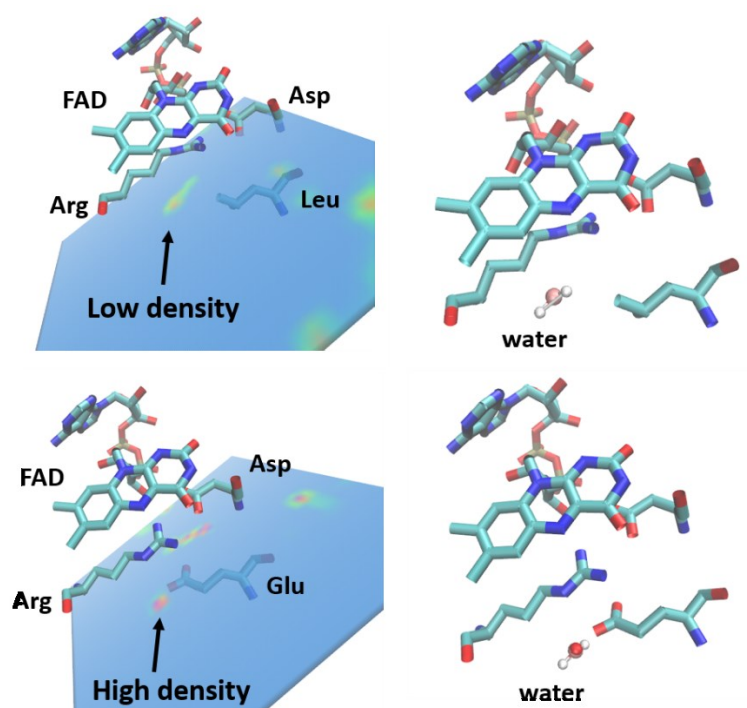


Water movement upon protonation can be observed on simulation and experimental data. Movement of water is highlighted by arrows pointing from original position to final position. The stick models were shown in $FAD^{\bullet-}$ and $FADH^{\bullet}$ with orange and blue color, respectively. (A) Via QM/MM simulation, proton transfer only occurred at R378N ϵ if N ϵ was stabilized by nearby water and E407 (Dr. Igor Schapiro group). Furthermore, from our previous study⁷³ of most twist model $E_{ox/10\mu s}$ comparing to semiquinone steady state ($E_{semi/ss}$), we could observe the similar of water movement which was further stabilized by E407.

Appendix 35. Stick model of protonation relevant residues.



(A) As shown in figure, MmCPDII (PDB number, 7F8T) was superposed with CraCRY (PDB number, 6FN3) and shown by cyan and green color respectively. A crystallographic water had suggested in MmCPDII and being stabilized by E407 instead of leucine. (B) The defined stick model of E407Lox has indicated no water near by L407. FAD and relevant residues were shown in yellow and orange color, respectively.

Appendix 36. Molecular Dynamic simulation for water environment.

Based on MD simulation, if substituting E407 with Leu in MmCPDII suggested that the high density of crystallographic water which had been stabilized R378Nε becoming low density, indicating no crystallographic water in the original position. (Performed by Dr. Han-Yang, Cheng).

8. Acknowledgements

First, I thank Prof. Lars-Oliver Essen who provides the opportunity to finish the PhD thesis in his group. I am very grateful to him for his enthusiasm, trust and his support over the past four years and close collaboration in this work. Next, I would like to thank Distinguished Visiting Chair Prof. Ming-Daw Tsai who offers me the chance to do not only the entire work itself but also a lot of opportunities to learn time-resolved experiments at locations such as SACLA in Japan, SwissFEL in Switzerland and ESRF in France. With his tremendous support, I could promote scientific knowledge to my heart's content. Furthermore, words cannot express my gratitude to Assistant Prof. Manuel Maestre-Reyna, who teaches and leads me into the structure biology and biochemistry fields. His insight into structural biology, scientific erudition and experimental cogitation make me admire again and again. With his enthusiasm and patience of teaching, I am certain that I am a much better and reliable person on the studies and experiments. To me, he is not only a supervisor, but also more like a partner and a friend.

I would also like to thank Prof. Olalla Vazquez and Prof. Alfred Batschauer for taking part in my Examination Committee and giving me many suggestions and ideas of my work.

I thank Associate Prof. Junpei Yamamoto who synthesized the (6-4)PP lesion DNA for me so that I can perform the co-crystallization in this work. I also thank Dr. Antoine Royant, Dr. Sylvain Engilberge and Dr. Nicolas Caramello who performed TR-*ic*OS experiments.

I would also like to thank the lab members who helped me to perform the TR-SFX experiments: Dr. Cheng-Han Yang, Dr. Hsiang-Yi Wu, Dr. Wen-Jin Wu, Dr. Yao-Kai Chang and Dr. Chiung-Wen Chang in Academia Sinica, Taiwan; Dr. Yuhei Hosokawa and Ms. Mia Nakamura in Osaka University, Japan; Dr. Martin Saft and Dr. Hans-Joachim Emmerich in Philipps University Marburg, Germany. Especially for Dr. Cheng-Han Yang, he helped me a lot to perform the simulation and in computation works. He always goes exercise with me to relax the stress and encourage me to look forward. Additionally, Dr. Hsiang-Yi Wu often provides many delicious foods to me so that I have more energy on the experiments of daily works.

Special thanks to my best friend in Taipei, Mr. Chih-Teng Hsu, who offered many meats and beers during holidays and made my life more interesting and colorful.

I am very grateful to my dear family, they are always huge supporting of my life decision, and encouraging me to do what I interested in.

Finally, I would like to thank myself to work hard and serious attitude on my studies and experiments with perseverance and initiative to complete my Ph. D degree.